Technical Physics Letters, Vol. 27, No. 1, 2001, pp. 1–5. Translated from Pis'ma v Zhurnal Tekhnicheskoĭ Fiziki, Vol. 27, No. 1, 2001, pp. 3–11.

An Effective Wavelet Analysis of the Transition to Chaos via Intermittency

A. A. Koronovskiĭ and A. E. Khramov

Saratov State University, Saratov, Russia

e-mail: alkor@cas.ssu.runnet.ru

Received June 19, 2000

Abstract—A new method based on the wavelet transformation is proposed, which provides for the effective determination of the duration of laminar and turbulent stages in a time pattern of the transition to dynamic chaos via intermittency. © *2001 MAIK "Nauka/Interperiodica".*

A possible classical scenario for the passage from periodic to chaotic oscillations is the passage via a transient regime or intermittency (see, e.g., [1, 2]). In this case, a periodic time pattern generated by a dynamic system is interrupted (in the course of increase in the control parameter) by irregular (or, in other words, turbulent) motions. The classical methods used for separating the regular motion stages are based on analysis of either the "current" period or the amplitude of oscillations.

Apparently, the former approach can be applied only when a laminar stage generates a signal close to strictly regular, which is by no means always the case. Actually, a laminar stage usually represents an almost periodic motion that hinders the application of this classical method and decreases accuracy of the description. The second approach can be used only in the case when the oscillation amplitude in the chaotic region differs significantly from that in the regular regime. Otherwise, we are again facing the necessity of dealing with strictly periodic oscillations in the laminar stage of motion.

For rigorously predicting the laminar and turbulent motion stages and correctly determining their durations, we propose a method based on the wavelet transformation [3, 4]

$$W(t, s) = \frac{1}{\sqrt{s}}\int_{-\infty}^{+\infty} x(t')\psi^*\left(\frac{t-t'}{s}\right)dt', \qquad (1)$$

where $x(t)$ is a time pattern, $\psi(\eta)$ is the base wavelet (asterisk denoting complex conjugate), and s is the analyzed time scale. We have used the base wavelet of the Morlet type $\psi(\eta) = \pi^{-1/4}e^{j\omega_0\eta}e^{-\eta^2/2}$, representing a rapidly decaying harmonic wave [5]. The ω_0 value was taken equal to 6, which allows for an analogy with the Fourier transformation [3], which is conveniently achieved by considering a wavelet surface W as a function of the time t and the scale corresponding to the frequency $f_s = 1/s$.

It was found that the wavelet surface $W(t, f_s)$ must possess significantly different structures in the regions corresponding to the laminar and turbulent stages of motion. A weakly irregular character of the signal in the laminar stage has virtually no effect on the wavelet surface structure and, hence, does not lead to errors in determining the duration of each stage. Therefore, based on the wavelet surface structure analysis using an appropriate method, we may rather simply search for different stages or intermittent regimes.

The approach to predicting the laminar and turbulent stages can be illustrated for a conventional example representing the Lorentz model system

$$\dot{x} = \sigma(y-x), \quad \dot{y} = rx - xz - y, \quad \dot{z} = xy - bz. \qquad (2)$$

For the set of control parameters $\sigma = 10$, $b = 8/3$, and $r < r^* \cong 166.07$, the time pattern generated by the Lorentz system (e.g., for the x value considered below) represents a periodic motion. Upon exceeding the threshold level r^*, the regular oscillations $x(t)$ (laminar stage) are interrupted by chaotic "outbursts," the duration of which increases with r until the motion becomes fully chaotic (turbulent stage). An intermittency in the Lorentz system is classified as an intermittency of type I [6].

Figure 1a shows a typical time pattern $x(t)$ and the corresponding projection of the wavelet surface $W(t, f_s)$ for the bifurcation parameter $r = 166.1$. The dark regions correspond to maxima of the surface. The curve in Fig. 1a indicates the region featuring boundary effects [3]. The wavelet surface projection displays clearly manifested regions corresponding to the laminar and turbulent stages in the given time pattern.

The wavelet surface structure corresponding to the regular stage of motion has a profile $W(t, f_s)|_{t = \text{const}}$ with two global maxima (corresponding to two dark bands parallel to the time axis in the projection of the W surface in Fig. 1a). This profile does not change with time

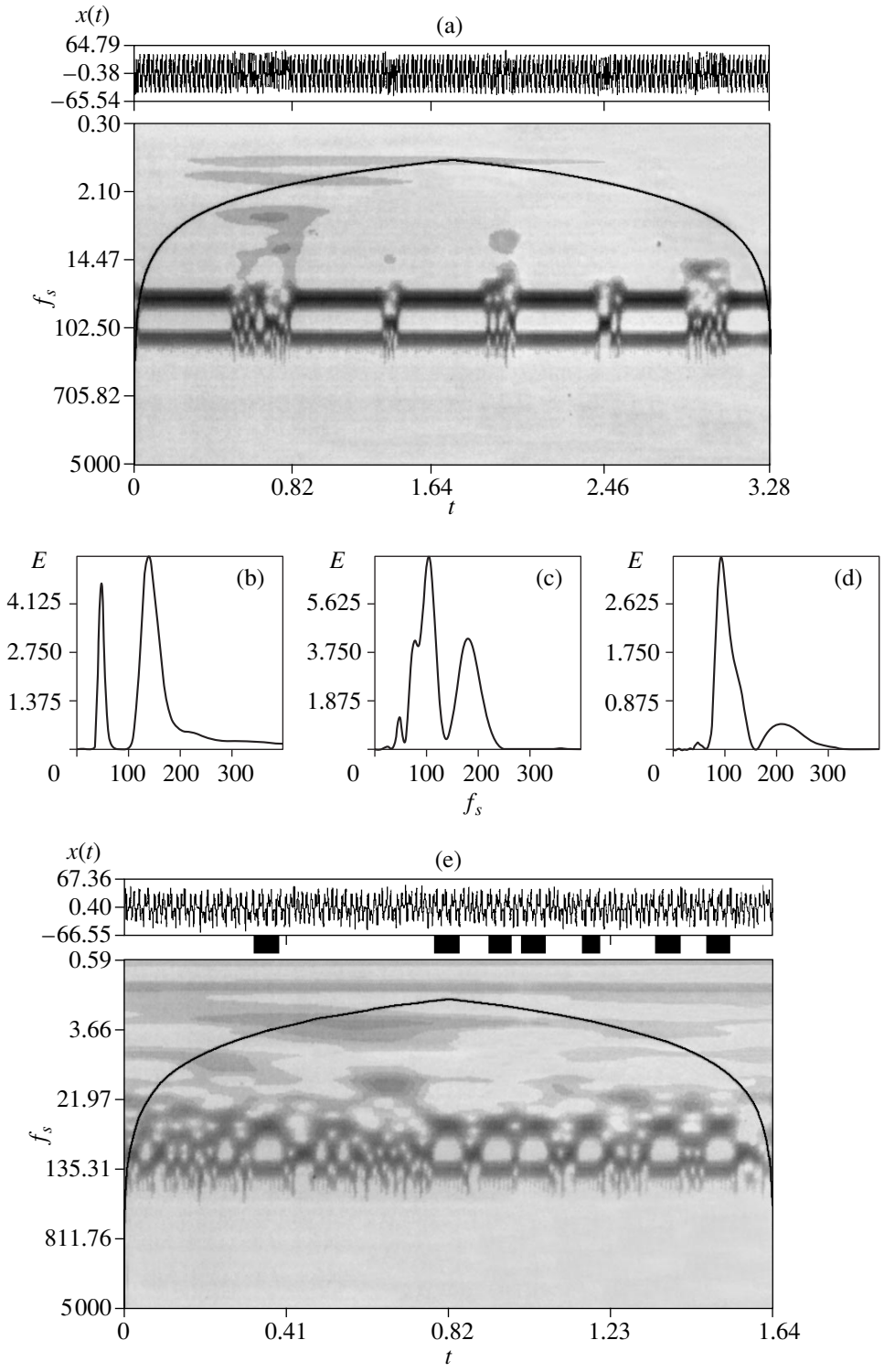

Fig. 1. Wavelet transformation analysis of the time pattern $x(t)$ numerically calculated for the model Lorentz system according to Eqs. (2) using the 4th order Runge–Kutta method (pattern length, $N = 2^{15}$ counts; time step, $\Delta t = 0.0001$): (a) projection of the wavelet surface $W(t, f_s)$ for the bifurcation parameter $r = 166.1$ and the supercritical difference $r - r^* = 0.03$; (b–d) instantaneous energy distributions for the (b) laminar ($t = 0.36$) and (c, d) turbulent stages ($t = 0.56$ and 0.72, respectively); (e) projection of the wavelet surface for $r = 167.0$ and $r - r^* = 0.93$ (black bars at the time pattern indicate the laminar stages).

t within the laminar stage of motion. This shape of the wavelet surface profile, featuring two characteristic global maxima, is related primarily to some features of the Fourier spectrum of a signal corresponding to the laminar stage. This spectrum is characterized by two dominating harmonics with the frequencies $f_1 = 41.3$

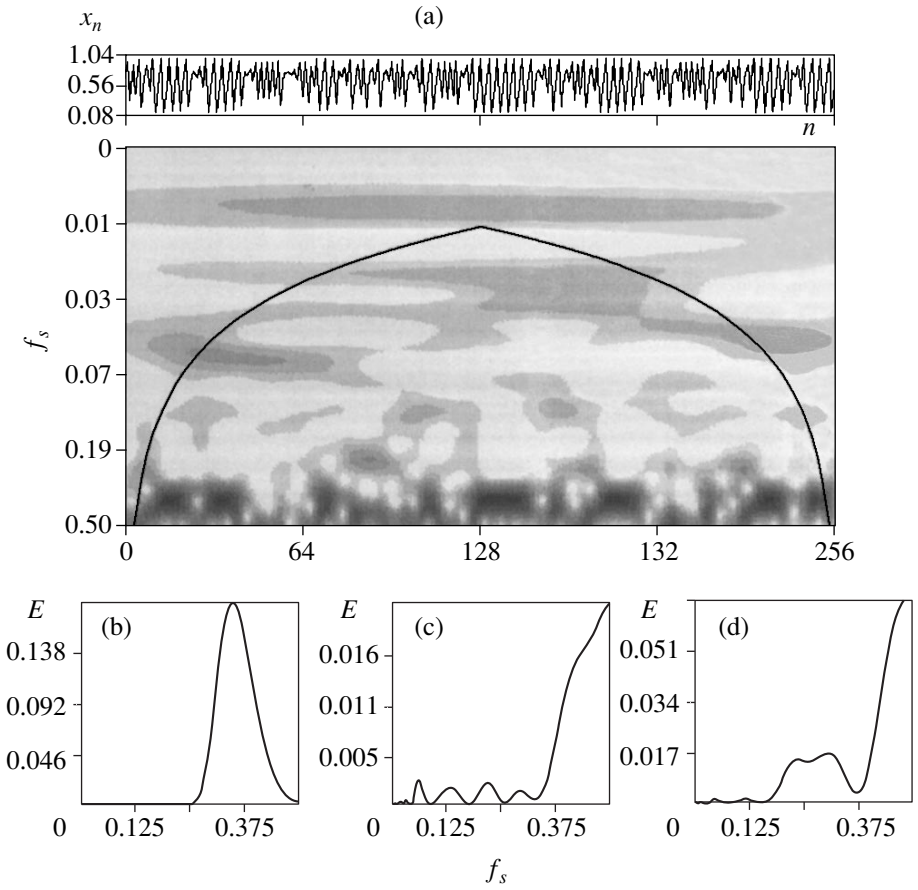

Fig. 2. Wavelet transformation analysis of the time pattern $x_n(t)$ corresponding to a logistic mapping $x_{n+1} = \varepsilon x_n(1 - x_n)$ (pattern length, $N = 256$ counts): (a) projection of the wavelet surface $W(t, f_s)$ for the mapping parameter $\varepsilon = 1 + \sqrt{8} - 0.002$ (b–d) instantaneous energy distributions for the (b) laminar ($n = 136$) and (c, d) turbulent stages ($n = 62$ and 220, respectively).

and $f_2 = 131.3$, which correspond to two maxima observed in the wavelet surface.

When the system enters the turbulent stage, the shape of the W surface exhibits a dramatic variation. The transition to a chaotic dynamic regime is accompanied by the "outburst" of oscillatory phenomena on various scales, the main energy falling within the scale interval corresponding to $f_s \in (f_1, f_2)$. Note that the regions of the wavelet surface corresponding to turbulent stage are strictly defined in time.

As noted above, the wavelet surface structure does not change with time in the laminar stage of motion. The instantaneous energy distribution over the time scales (frequencies) $E(f_s)|_{t = \text{const}}$ in this stage is also time-independent (Fig. 1b). This distribution exhibits a characteristic shape with two maxima, the nature of which was discussed above (the peaks are due to the two frequencies f_1 and f_2 dominating in the Fourier spectrum corresponding to the laminar stage).

The onset of a turbulent stage is manifested by splitting of the $1/f_1$ and $1/f_2$ scales. The resulting energy spectrum exhibits a single dominating scale. Subsequently, the turbulent stage features the excitation and damping of oscillations in the system. These chaotic oscillations occur on various time scales, predominantly below $1/f_1$. The energy distribution during the turbulent stage is essentially nonstationary. The only feature observed over the entire chaotic "outburst" is the presence of a dominating scale $1/f_s \sim 0.011$ (here, the sign "~" indicates that the position of maximum energy varies and the value 0.011 represents an average over several turbulent outbursts). The shape of the energy distribution markedly changes with time. This is illustrated by Figs. 1c and 1d showing the instantaneous energy distributions over the time scales $E(f_s)$ corresponding to the time moments $t = 0.56$ and 0.72. As seen, the two curves differ in both number and position of maxima.

As the bifurcation parameter increases, the duration of laminar stages decreases and eventually (at $r > 167.0$) the laminar motion is virtually indistinguishable in the time pattern. At the same time, the wavelet analysis successfully reveals the laminar stages with a duration of 2–3 periods of oscillation on the main frequency. This is illustrated in Fig. 1e, which shows the

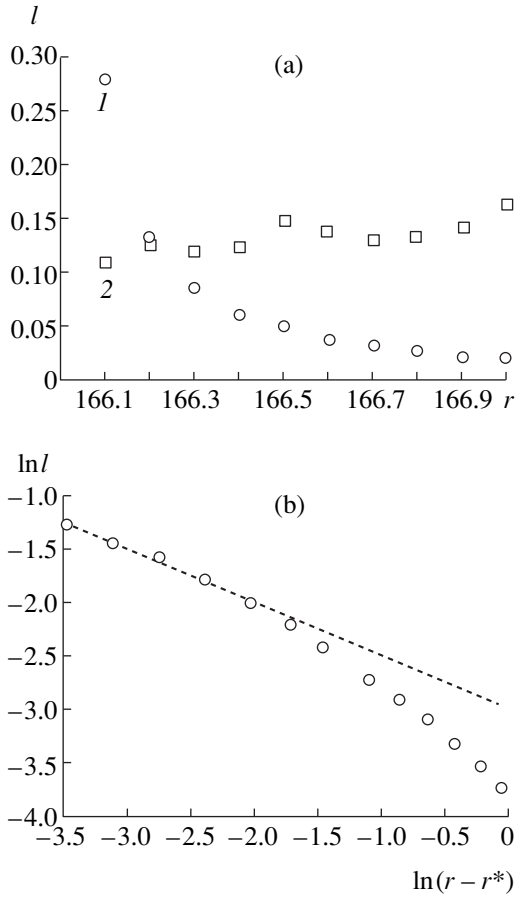

Fig. 3. Average laminar and turbulent stage durations determined using the wavelet transformation analysis of the time pattern $x(t)$ the model Lorentz system presented in Fig. 2: (a) plots of the (*1*) laminar and (*2*) turbulent stage duration versus the bifurcation parameter r; (b) logarithmic plot of the average laminar stage duration versus the supercritical difference $r - r^*$ near the intermittency threshold r^* (open circles, data of this work; dashed curve, power law with the exponent 1/2).

results of the wavelet transformation obtained for the control (bifurcation) parameter $r = 167.0$. As seen, the laminar stages in the time pattern correspond to the characteristic features in the wavelet surface projection $W(t, f_s)$.

This situation does not take place only in analysis of the time patterns generated by the flow systems. For illustration, Fig. 2a shows the results of the wavelet transformation of a time pattern generated by a logistic mapping $x_{n+1} = \varepsilon x_n(1 - x_n)$ with a control parameter $\varepsilon^* - \varepsilon = 0.002$. Here, $\varepsilon^* = 1 + \sqrt{8}$ is the critical value corresponding to the tangential bifurcation of the regular cycle of period 3 (whereby the stable and unstable 3-cycles merge and vanish), while lower values of the parameter correspond to a regime with the laminar stages interrupted by turbulent outbursts.

An analysis of the wavelet surface and its comparison with the time pattern shows that laminar stages in this system also correspond to a special characteristic structure of the W function. Similar to the dynamics observed for the Lorentz system, the escape from the laminar stage of motion is accompanied by the disappearance of the time scale corresponding to regular oscillations. Also significantly different are the characteristic oscillation energy distributions over the time scales (frequencies) for the chaotic and laminar regimes. In the latter case, the $E(f_s)$ distribution remains unchanged and has a shape depicted in Fig. 2b. In the turbulent regime, the energy distribution is time-dependent (see Figs. 2c and 2d showing the $E(f_s)$ functions for two different time instants).

The results of the wavelet analysis presented above for the Lorentz model exhibit a sufficiently universal character from the standpoint of analysis of the transition to chaos via intermittency. Therefore, the wavelet transformation of time patterns generated by dynamic systems featuring a transition to chaos via intermittency can be used for distinguishing and analyzing the laminar and turbulent stages.

The structure of the wavelet surface can be analyzed by a method based on determining the number of maxima F in the instantaneous energy distributions over the time scales $E(f_s)|_{t = \text{const}}$. The number of maxima, which is unchanged during a laminar stage, becomes time-dependent upon transition into a turbulent regime. Using this approach, we may effectively separate the laminar stages of motion. Taking into account that F may acquire only integer values, the determination of the duration of, for example, the laminar stage from the $F(t)$ function is very simple. This method is well applicable upon going to a greater bifurcation parameter.

To illustrate the proposed method, we have determined the average durations l of laminar and turbulent stages as functions of the bifurcation parameter r. The number of laminar (and, accordingly, the turbulent) stages for which the l values were determined amounted to 600–800. The results of this analysis are presented in Fig. 3a. The average duration of the laminar stage of motion noticeably decreases with increasing r; the average duration of the chaotic stage varies at a much lower rate, showing a tendency to increase with the bifurcation parameter. The latter fact is quite explainable, since the chaotic stage of the motion is essentially the stage of "relaminarization," that is, of the system return to the regular motion. Evidently, the duration of the relaminarization process must be independent of the bifurcation parameter r.

Figure 3b shows the plot of $\ln l$ versus $\ln(r - r^*)$. The logarithmic scale clearly demonstrates that the laminar stage duration is proportional to the square root of the distance $r - r^*$ from the intermittency threshold (at least for sufficiently small $r - r^*$ values), which is in agreement with the theory of type I intermittency [6]. For

large values of the supercritical difference, the laminar stage duration deviates from the power law. Thus, the proposed method gives results in good agreement with the published data [2, 6].

Acknowledgments. This study was supported by the Russian Foundation for Basic Research, project nos. 99-02-16016 and 98-02-16541.

REFERENCES

1. P. Manneville and Y. Pomeau, Physica D (Amsterdam) **1**, 219 (1980).
2. Y. Pomeau and P. Manneville, Commun. Math. Phys. **75**, 189 (1980).
3. C. Torrence and G. P. Compo, Bull. Am. Meteorol. Soc. **79**, 61 (1998).
4. *Wavelets*, Ed. by J. M. Combes, A. Grossman, and T. Tchamitchian (Springer-Verlag, Berlin, 1989).
5. A. Grossman and J. Morlet, SIAM J. Math. Anal. **15**, 723 (1984).
6. H. G. Schuster, *Deterministic Chaos* (Physik-Verlag, Weinheim, 1984; Mir, Moscow, 1988).

Translated by P. Pozdeev

Technical Physics Letters, Vol. 27, No. 1, 2001, pp. 11–13. Translated from Pis'ma v Zhurnal Tekhnicheskoĭ Fiziki, Vol. 27, No. 1, 2001, pp. 24–30.

A New High-Brightness Stepped-Crystal Diffractor for X-ray Microanalysis

M. I. Mazuritsky*, A. V. Soldatov*, V. L. Lyashenko*, E. M. Latush*, A. T. Kozakov*, S. I. Shevtsova*, and A. Marcelli**

** Faculty of Physics, Rostov State University, Rostov-on-Don, Russia*

*** LNF, INFN, Frascati, Italy*

e-mail: mazurmik@icomm.ru

Received August 21, 2000

Abstract—An electron-probe X-ray microanalyzers, the characteristic X-ray radiation is generated within a small volume of sample and the emitting surface area is on the order of 1 μm^2. For a distance to analyzer of approximately 0.5 m, this small emitting area can be considered as a point source. Practical implementations of the electron-probe X-ray microanalysis (EPMA) require a high spectral resolution and sufficient intensity. The existing monochromators cannot simultaneously provide for both. A prototype of the new high-brightness stepped-crystal diffractor for EPMA, based on four cylindrically bent (002) mica crystals, has been constructed and tested. © *2001 MAIK "Nauka/Interperiodica".*

As is known, both perfect and mosaic crystals are used for separating monochromatic X-rays with energies ranging from a few hundreds to tens thousand of electronvolts. In the case of virtually point emission sources, it is expedient to employ either the classical focusing X-ray optics based on cylindrically bent crystals proposed by Johann [1], Johansson [2], and Cauchois [3], or the more recent schemes based on spherical and toroidal geometries of the bent crystallographic planes [4, 5].

Some analytical problems solved by method of electron-probe X-ray microanalysis (EPMA) require instruments possessing a high spectral resolution ($\lambda/\Delta\lambda$) together with sufficiently large signal intensity (brightness). The existing monochromators cannot simultaneously provide for both. It is the usual practice to compromise between the necessary resolution level (related to small reflecting area of a crystal analyzer) and acceptable aperture of the diffractor. However, attaining a sufficiently high resolution [$\lambda/\Delta\lambda \sim (1–5) \times 10^3$] in the schemes with bent crystals of any type necessarily imposes certain limitations on the reflecting crystal surface area, thus determining the spectrometer brightness limit.

Previously [6], we proposed a new algorithm and developed a computer program for modeling the diffraction zones and reflecting surfaces of a bent crystal monochromator of any type (cylindrical, spherical, toroidal, etc.) employed in the schemes of focusing on the Rowland circle. For a given resolution parameter, this program determines the shape of a reflecting crystal surface corresponding to the Bragg equation (Bragg's diffraction zone), the optimum curvature parameters, and the diffractor crystal size.

Recently, we proposed for the first time a model [7, 8] and described a mathematical scheme [9] of a high-brightness stepped-crystal X-ray diffractor capable of providing a high spectral resolution at a constant angular width of each step. In an electron-probe X-ray microanalyzer, the primary characteristic X-ray radiation generated within a microscopic sample volume enters the spectrometer chamber. Scanning over the wavelength spectrum is carried out by simultaneously moving the bent crystal (diffractor) and a detector of the crystal-monochromated radiation. In the proposed scheme, the radiation source, the crystal apex, and the input window of the detector are situated on the focusing circle. The optical scheme of a spectrometer channel for the EPMA instrument is described in more detail in the monograph [10].

Figure 1a illustrates the principle of spectral analysis and the scheme of focusing of the crystal-monochromated X-ray radiation. The radiation source S and detector D occur on the focal circle (Rowland's circle), the third point representing the diffractor apex located at the middle of the central step. In this study, we have used a special shape of the reflecting crystal (Fig. 1a) with a stepped pseudocylindrical surface characterized by a constant angular size of steps in the focal circle plane. Each step represents a part of the cylindrical surface with a constant radius, onto which a bent (002) mica crystal is glued. The central step has a bending radius equal to doubled radius of the focal circle. The bending radii of the following steps decrease with increasing distance from the diffractor center. The symmetry axes of all the cylindrical surfaces coincide with the vertical axis passing through point O perpendicularly to the focusing circle. The algorithm for calculat-

1063-7850/01/2701-0011$21.00

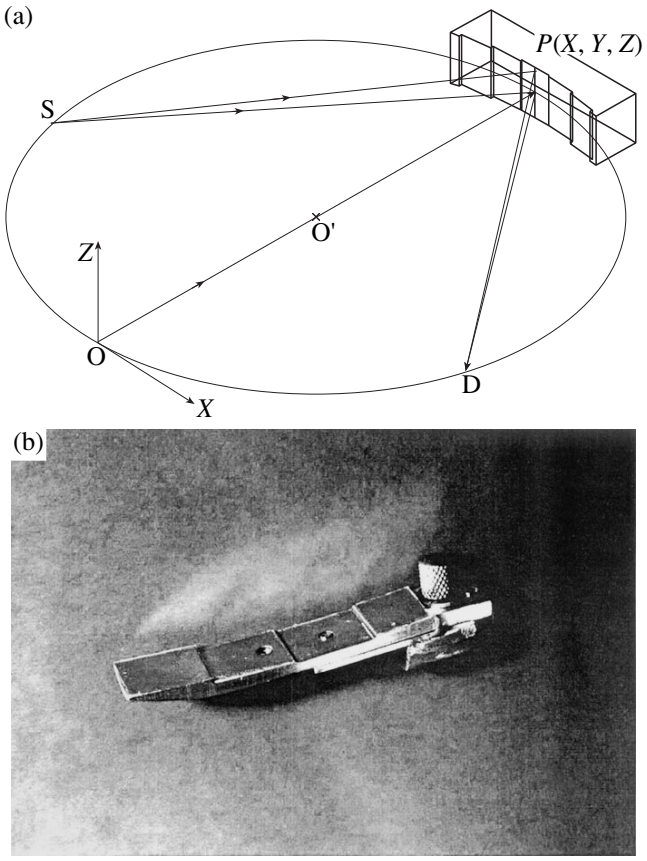

Fig. 1. A pseudocylindrical stepped-crystal X-ray diffractor: (a) schematic diagram showing the principle of spectral analysis and focusing of the X-ray radiation (*XYZ*, coordinate system; O' and O, centers of the focusing circle and step curvature, respectively; S and D radiation source and its image, respectively); (b) a general view of the prototype diffractor for an EPMA instrument.

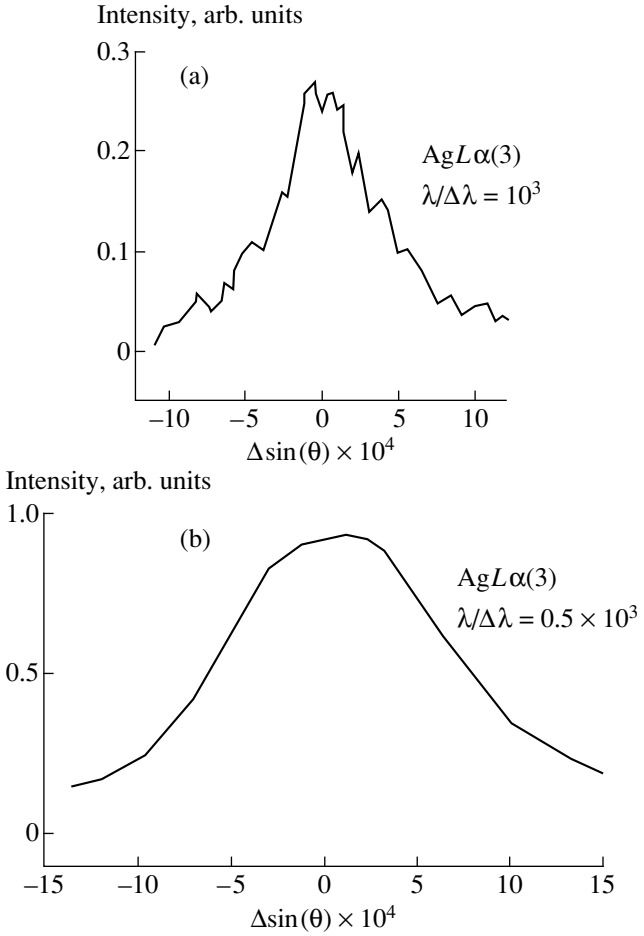

Fig. 2. Ag$L\alpha$(3) X-ray emission spectra obtained using cylindrically bent (002) mica crystals at a Bragg angle of $\theta = 38.92°$ (a) for a single central crystal (resolution, $\lambda/\Delta\lambda = 10^3$) and (b) for the whole four-step diffractor ($\lambda/\Delta\lambda = 0.5 \times 10^3$).

ing the step radii and other parameters of the diffractor was described in [9].

Figure 1b shows the general view of a diffractor prototype manufactured for an EPMA system of the CAMEBAX-micro type, in which the focal circle radius of the spectrometer is 160 mm. The diffractor crystal holder is designed so as to accommodate four steps (with different numbers of steps on the left and right sides of the central step).

The stepped-crystal diffractor prototype was tested in the spectrometer channel of a CAMEBAX-micro analyzer operating with an Ag$L\alpha$(3) radiation at $\theta_B = 38.92°$. Figures 2a and 2b shows typical emission spectra obtained using the central step alone and the whole diffractor. For the X-ray diffraction on the central crystal step, the measured spectral resolution amounted to $\lambda/\Delta\lambda = 10^3$. For the whole diffractor, containing four cylindrically bent crystals, the resolution was somewhat lower (0.7×10^3) but the peak intensity increased by a factor of 3.3, which approximately corresponds to a ratio of the entire diffractor surface to that of the central step. Therefore, the spectrum intensity in the analyzer prototype studied increases in proportion to the working area of the diffractor surface.

Thus, replacing a bent single crystal in the Johann scheme [1] by the stepped-crystal diffractor composed of four bent mica crystals provided for an increase in intensity. The spectral resolution must, in principle, remain unchanged. However, the experimental spectra (Figs. 2a and 2b) show that the resolution slightly decreased. This can be explained by errors in manufacturing the crystal holder or uncertainties in gluing the crystals.

In order to analyze the possible factors and sources of uncertainty, we have used a high-precision profilometer (Rank Taylor Hobson) to study profiles of the diffractor steps. It was found that the bent mica crystal remains sufficiently smooth on the side of reflecting face, the surface roughness size not exceeding a few microns. At the same time, the surface profiles revealed ridges with a height of 20–30 μm, showing evidence of

a partial cleavage and separation of the outer crystal surface layers. However, the most significant factor detrimentally affecting resolution of the stepped-crystal diffractor was a noncoaxial alignment of the cylindrically bent mica crystals. Expressions relating the possible uncertainty due to displacement $\Delta x(\Delta y)$ of the axes of cylinders to the spectral resolution are as follows:

$$\Delta x = \frac{R}{\lambda/\Delta\lambda}\tan\theta; \quad \Delta y = \frac{R}{\lambda/\Delta\lambda}\tan^2\theta,$$

where R is the crystal bending radius.

In our case, the relative displacements of the axes of cylinders were on the order of 0.2 mm, which accounts for a resolution of 0.7×10^3. It was established that the error was caused by a technological error in manufacturing the crystal holder and gluing bent mica crystals on the holder surface.

REFERENCES

1. H. H. Johann, Z. Phys. **69**, 185 (1931).
2. T. Johansson, Z. Phys. **82**, 507 (1933).
3. Y. Cauchois, J. Phys. Radium **2**, 320 (1932).
4. C. Bonnelle and C. Mande, *Advances in X-ray Spectroscopy* (Pergamon, Oxford, 1982).
5. E. O. Baronova, M. M. Stepanenko, V. V. Lider, and N. R. Pereira, *Second Workshop, Weimar, Germany, 1999*, p. 213.
6. M. I. Mazuritskiĭ, A. V. Soldatov, E. M. Latush, *et al.*, Pis'ma Zh. Tekh. Fiz. **25** (19), 11 (1999) [Tech. Phys. Lett. **25**, 763 (1999)].
7. A. Marcelli, A. V. Soldatov, and M. I. Mazuritsky, Eur. Patent No. 97830282. 6-2208 deposited by INFN on 06/11/97 published on 12/16/98.
8. M. I. Mazuritsky, A. V. Soldatov, and A. Marcelli, Proc. SPIE **3449**, 75 (1998).
9. M. I. Mazuritskiĭ, A. V. Soldatov, E. M. Latush, *et al.*, Pis'ma Zh. Tekh. Fiz. **26** (12), 15 (2000) [Tech. Phys. Lett. **26**, 502 (2000)].
10. S. J. B. Reed, *Microanalysis* (Cambridge Univ. Press, Cambridge, 1997).

Translated by P. Pozdeev

Technical Physics Letters, Vol. 27, No. 1, 2001, pp. 14–16. Translated from Pis'ma v Zhurnal Tekhnicheskoĭ Fiziki, Vol. 27, No. 1, 2001, pp. 31–38.

Optical Properties of Submonolayer Germanium Clusters Formed by Molecular-Beam Epitaxy in a Silicon Matrix

G. É. Cirlin, P. Werner, G. Gösele, B. V. Volovik, V. M. Ustinov, and N. N. Ledentsov

Max Planck Institute of Microstructure Physics, Halle, Germany
Ioffe Physicotechnical Institute, Russian Academy of Sciences, St. Petersburg, Russia
Technical University, Berlin, Germany
Institute of Analytical Instrument Building, Russian Academy of Sciences, St. Petersburg, Russia

Received September 4, 2000

Abstract—Study of the optical properties of submonolayer germanium clusters formed by molecular beam epitaxy in a silicon matrix showed that the spectra of samples obtained at elevated deposition temperatures (~750°C) contain a series of new bands related to the formation of germanium nanoislands. © *2001 MAIK "Nauka/Interperiodica".*

Introduction. As is known, silicon occupies the leading position in the market of materials for microelectronic devices. However, use of this semiconductor in optoelectronics is limited by its indirect band structure, leading to a considerable decrease in the luminescence efficiency. Nevertheless, integrating silicon microelectronic technologies with facilities of the optical data transmission in the same microchip is an urgent task, primarily in the field of silicon-based light-emitting devices (SLEDs).

A considerable effort of researchers devoted to the SLED development is shared between several principal approaches based on the use of porous silicon [1], Ge/Si and GeSiC/Si quantum dots obtained by molecular-beam epitaxy (MBE) [2], silicon doped with rare-earth elements [3], InAs nanostructures incorporated into silicon matrix [4], and some others. Despite obvious progress in research, the results still did not find commercial implementations, which stimulates the search for new approaches to solving the problem of obtaining SLEDs.

Below, we will consider one of the possible approaches, based on the formation of submonolayer (SML) germanium clusters in a silicon matrix, and report on the optical properties of these heterostructures. It is suggested that SML Ge clusters may form an ensemble of sufficiently small islands with lateral dimensions below the Bohr radius of holes. This would partly change selection rules for the radiative recombination and provide for the possibility of exciton formation upon the interaction of electrons with localized holes, the excitons being stable at temperatures up to room temperature.

This situation will be possible provided that the Coulomb attraction of electrons to holes exceed the repulsion due to a potential barrier created by SML Ge clusters in the conduction bands, which may lead to the appearance of spatially separated electrons and holes in quantum dots and holes of sufficiently large size (width) [5]. The narrow photoluminescence (PL) bands characteristic of SML clusters in other heteroepitaxial systems [6–8] would favor an increase in the absorption coefficient (gain) in these structures. A further increase in the PL intensity can be achieved in multiple (stacked) layers with SML Ge clusters, separated by Si barriers (spacers). Note that the probability of the formation of dislocations and stacking faults in these systems is small because of a rather low level of stresses in such heterostructures.

Experiment. The heterostructures were grown in a Riber SIVA 45 setup by MBE on phosphorus-doped *n*-type Si(100) substrates (5-inch OKMETIC wafers) with a resistivity of 3 Ω cm. The substrates were chemically pretreated using the following procedure: (i) boiling in an H_2O_2–H_2SO_4 (1 : 1) solution for 10 min to remove organic compounds of heavy metals; (ii) treatment in an HF–H_2O (1 : 10) solution at room temperature for 1 min to remove the surface oxide layer; (iii) treatment in an HCl–H_2O_2–H_2O (1 : 1 : 6) solution at 80°C for 10 min to remove alkali metals, Al, Fe, and Mg; (iv) treatment in an NH_4OH–H_2O_2–H_2O (0.5 : 1 : 5) solution at 80°C for 10 min to restore the oxide layer. After each treatment step, the wafers were rinsed in deionized water; the first treatment was repeated. After the chemical pretreatment, the substrates were dried in a flow of argon (6.0 purity grade) and charged into a sample-changing stage of the MBE setup. The surface oxide layer could be removed from Si wafers in the growth chamber by radiation heating to 840°C. The sample heater was rotated during the MBE growth, which ensured inhomogeneity of the temperature field over the substrate surface not exceeding 5%.

1063-7850/01/2701-0014$21.00 © 2001 MAIK "Nauka/Interperiodica"

The SML Ge clusters were obtained by a method developed previously for the preparation of analogous inclusions of A_3B_5 and A_2B_6 compounds [9–11]. The structures comprised a 1000-Å-thick buffer Si layer, a Ge(0.7 Å)/Si(35 Å) superlattice (99 pairs), and a 200-Å-thick Si overlayer. The MBE growth rates of Si and Ge layers were 0.5 and 0.05 Å/s, respectively. The constant deposition rates were controlled by two mass-spectrometers with feedback circuits tuned to m/z = 28 (Si) and 74 (Ge). The samples of two types were prepared on the substrates heated to 500°C (sample 1) and 750°C (sample 2). The residual pressure during MBE did not exceed 5×10^{-9} torr. The state of the sample surface was monitored *in situ* by reflection high-energy electron diffraction (RHEED). The photoluminescence spectra were excited by Ar^+ laser (λ = 514.5 nm) operated at a maximum radiant power density of ~500 W/cm^2. The sample emission was detected with a cooled Ge photodiode.

During the MBE growth, the RHEED patterns exhibited (irrespective of the sample temperature) no significant changes compared to the initial (2×2) surface reconstruction. Therefore, even the uppermost superlattice layers remained atomically smooth and a three-dimensional structure was not formed as a result of the stress relaxation.

Results and discussion. The results of our optical measurements showed that the PL spectrum of sample 1 was virtually identical with that of the substrate, while the spectrum of sample 2 displayed a set of new bands observed neither in the substrate nor in sample 1. Figure 1 shows the room-temperature PL spectrum of sample 2 in comparison to that of the substrate measured for the same excitation intensity. The PL spectrum of sample 2 possesses an integral intensity comparable to that of the substrate spectrum and exhibits a series of additional PL bands denoted by SL–(NP, TA, TO, TO + O) not found in the substrate spectrum. The SL–NP band corresponds to the nonphonon photoluminescence, while the other additional bands are due to emission with participation of the corresponding phonons. It should be noted that the SL bands could not be observed in the PL spectra of Si substrates measured at either very high or very low excitation levels. The PL bands assigned to emission from the silicon substrate are denoted by Si–(NP, TA, TO + O). Thus, we attribute the SL bands to the emission from excitons localized at the Ge clusters occurring in the SML superlattice.

The ratio of intensities of the PL peaks due to the SML Ge/Si superlattice and the Si substrate significantly depends on the excitation level. Figure 2 shows the PL spectra of sample 2 measured at various relative intensities of the optical excitation. As the excitation level grows, the Si–TO/SL–TO band intensity ratio increases. However, the integral intensities of these bands are comparable even at high excitation levels, while at low levels the SL–TO contribution dominates. The full width at half maximum (WFHM) for the PL

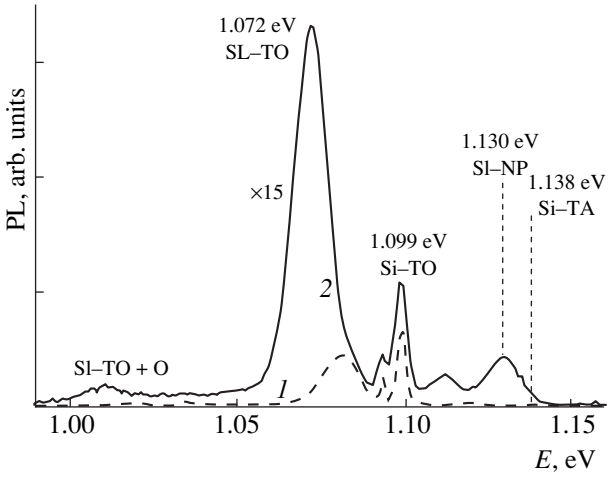

Fig. 1. Typical PL spectra of (*1*) Si substrate and (*2*) sample 2 measured at 10 K with an excitation power density of 5 W/cm^2.

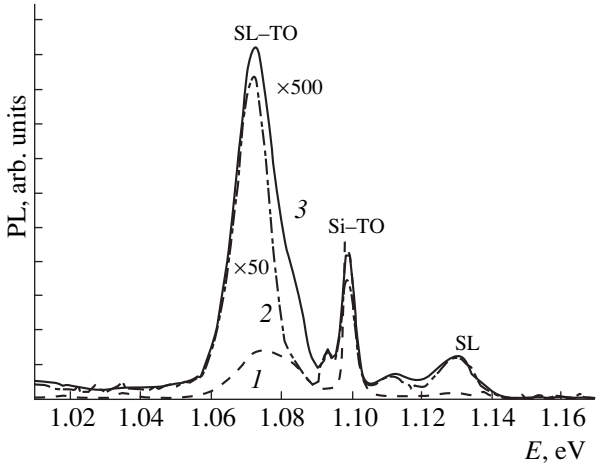

Fig. 2. The PL spectra of sample 2 measured at 10 K with various excitation power densities: (*1*) $0.5I_0$; (*2*) $0.05I_0$; (*3*) $0.005I_0$ (I_0 = 500 W/cm^2).

bands is approximately 15 meV. The change in the excitation power density is not accompanied by shift of the SL–TO band.

Previously [12], we reported on the formation of quantum filaments on a vicinal Si(100) surface upon deposition of a small (below 0.5 ML) amount of Ge followed by vapor-phase MBE of silicon. Variation of the SL–TO photoluminescence peak position observed in [12] was explained by the formation of a density of states typical of a laterally confined configuration. The TO band position observed in [12] for an 0.12 ML Ge deposit, as well as the character of the PL intensity variation, agree with the behavior of the SL–TO peak observed in this study.

Figure 3 shows the temperature variation of the PL spectra of sample 2 measured at an excitation power density of 500 W/cm^2. Despite a significant decrease in

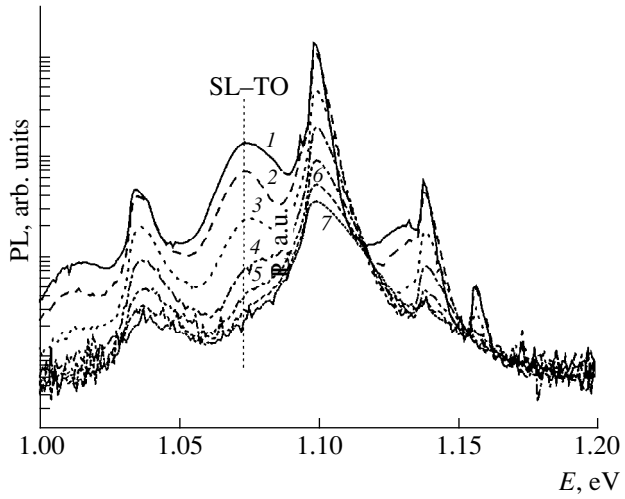

Fig. 3. The PL spectra of sample 2 measured at various temperatures $T = 10$ (*1*), 20 (*2*), 30 (*3*), 40 (*4*), 50 (*5*), 60 (*6*), and 70 K (*7*) with an excitation power density of 500 W/cm^2.

the integral intensity with increasing temperature, the SL–TO band position exhibits no change. A shortwave shift in the PL band position with increasing temperature was observed, for example, in a heteroepitaxial InAs/Si structure [13], where this behavior was explained by the heterojunction belonging to type II. Thus, our data indicate that behavior of the SL bands observed in the system studied is different from that typical of the type II heterojunctions.

The fact that characteristic features observed in the PL spectra of sample 2 are absent in the spectra of sample 1 can be related to the formation of greater two-dimensional Ge islands in the latter case, with lateral dimensions above the Bohr radius of holes (leading to delocalization of the holes in the given geometry). This hypothesis can be verified by studying the sample structure in detail by the method of high-resolution transmission electron microscopy. It should be noted that an increase in the lateral size of islands with decreasing deposition temperature was observed, for example, in an InAs/GaAs SML system.

Thus, we have observed a series of additional emission bands in the PL spectra of a system comprising SML Ge clusters in a Si matrix not contained in a typical PL spectrum of silicon. An analysis of the spectroscopic data allowed us to conclude that the new features are related to the formation of Ge clusters with a characteristic size below the Bohr radius of holes. No such PL bands are observed in a system with the Ge clusters of greater size. The system of submonolayer Ge clusters in a Si matrix can be considered as a possible variant of silicon-based light-emitting devices.

Acknowledgments. The authors are grateful to the Russian Foundation for Basic Research and the Federal Program “Physics of Solid State Structures” for partial support of this study.

REFERENCES

1. A. G. Cullis, L. T. Canham, and P. D. Calcott, J. Appl. Phys. **82**, 909 (1997).
2. K. Eberl, K. Brunner, and W. Winter, Thin Solid Films **294**, 98 (1997).
3. S. Coffa, G. Franzo, and F. Priolo, MRS Bull. **23** (4), 25 (1998).
4. G. E. Cirlin, V. G. Dubrovskii, V. N. Petrov, *et al.*, Semicond. Sci. Technol. **13**, 1262 (1998).
5. N. N. Ledentsov, I. L. Krestnikov, M. V. Maximov, *et al.*, Appl. Phys. Lett. **69**, 1343 (1996).
6. N. N. Ledentsov, A. F. Tsatsul’nikov, A. Yu. Egorov, *et al.*, Appl. Phys. Lett. **74**, 161 (1999).
7. M. V. Belousov, N. N. Ledentsov, M. V. Maximov, *et al.*, Phys. Rev. B **51**, 14346 (1995).
8. P. D. Wang, N. N. Ledentsov, C. M. Sotomayor Torres, *et al.*, Appl. Phys. Lett. **64**, 1526 (1994).
9. G. É. Tsyrlin, A. O. Golubok, S. Ya. Tipisev, *et al.*, Fiz. Tekh. Poluprovodn. (St. Petersburg) **29**, 1697 (1995) [Semiconductors **29**, 884 (1995)].
10. G. E. Cirlin, V. N. Petrov, A. O. Golubok, *et al.*, Surf. Sci. **377–379**, 895 (1997).
11. H. Sunamura, N. Usami, Y. Shiraki, and S. Fukatsu, Appl. Phys. Lett. **68**, 1847 (1996).
12. R. Heitz, N. N. Ledentsov, D. Bimberg, *et al.*, Appl. Phys. Lett. **74**, 1701 (1999).

Translated by P. Pozdeev

Technical Physics Letters, Vol. 27, No. 1, 2001, pp. 17–19. Translated from Pis'ma v Zhurnal Tekhnicheskoĭ Fiziki, Vol. 27, No. 1, 2001, pp. 39–46.

Strongly Modulated Conductivity in a Perovskite Ferroelectric Field-Effect Transistor

I. A. Veselovskiĭ, I. V. Grekhov, L. A. Delimova, and I. A. Liniĭchuk

Ioffe Physicotechnical Institute, Russian Academy of Sciences, St. Petersburg, 194021 Russia

Received September 4, 2000

Abstract—An all-perovskite field-effect transistor with a $(Pb_{0.95}La_{0.05})(Zr_{0.2}Ti_{0.8})O_3$ gate insulator exhibits a strongly modulated room-temperature conductivity in a $La_{1.94}Sr_{0.06}CuO_4$ channel. The channel conductivity is controlled by the hopping mechanism with variable jump length and determined by the Coulomb gap at the Fermi level. © *2001 MAIK "Nauka/Interperiodica".*

Introduction. A possible approach to creating an energy-dependent solid-state memory consists in using a ferroelectric base memory cell possessing a residual polarization in the absence of applied voltage. A most promising solution, providing for a high cell packing density, is offered by a field-effect transistor (FET) cell with ferroelectric gate insulator. This design allows the same cell to be used both for the recording and energy-dependent storage of data and for their nondestructive readout. However, creation of a ferroelectric-gate FET based on traditional semiconductors encounters serious difficulties because deposition of a ferroelectric film, for example, of a (Pb, La)(Zr, Ti)O_3 type, immediately onto a Si substrate leads to undesired diffusion of Pb and Ti into silicon and the formation of an intermediate silicon oxide layer with small dielectric permittivity. Introducing protective buffer layers between ferroelectric film and silicon substrate gives rise to additional problems.

As an alternative approach, Watanabe [1] suggested using an all-perovskite FET, in which the epitaxial heterostructures are formed by layers of perovskite semiconductors chemically and crystallographically compatible with a ferroelectric layer. Very promising results were obtained for a $SrRuO_3/Pb(Zr_{0.52}Ti_{0.48})O_3$ structure, in which a ±10 V bias voltage produced a 9% modulation of the channel conductivity [2], and for a $La_{1.99}Sr_{0.01}CuO_4/(Pb_{0.95}La_{0.05})(Zr_{0.2}Ti_{0.8})O_3$ structure capable of a 10% channel conductivity modulation for a ±5 V gate voltage variation [1].

Below, we report on a much stronger (~70%) conductivity modulation in a

$$La_{1.94}Sr_{0.06}CuO_4/(Pb_{0.95}La_{0.05})(Zr_{0.2}Ti_{0.8})O_3/Ag$$

(LSCO/PLZT/Ag) FET structure, which means a real possibility of creating an energy-dependent memory cell based on this device.

Sample fabrication. The LSCO/PLZT/Ag transistor structures were prepared by successively depositing the component films in the course of synchronous co-sputtering of two ceramic targets with crossed beams of two AYG lasers operating in the Q-switched mode (wavelength λ = 1064 nm; pulse energy, 20 mJ; pulse duration, 15 ns; pulse repetition frequency, 25 Hz; focused laser beam spot on the target surface, 1 mm). The oxygen pressure in the sample preparation chamber was 0.2 torr during layer deposition and 760 torr during cooling [3]. The sample structure geometry was formed using special silicon templates in the course of layer deposition.

The process of a FET structure formation was as follows. First, a $(La_{1.94}Sr_{0.06})CuO_4$ layer was deposited onto a $(110)NdGaO_3$ substrate at T = 650°C to form the transistor channel with a thickness of 10 nm, a width of 230 μm, and a subgate length of 320 μm. This was followed by depositing an overlayer of $(Pb_{0.95}La_{0.05})(Zr_{0.2}Ti_{0.8})O_3$ at a temperature of T = 500°C to form a 100-nm-thick ferroelectric insulator. Then the structure was cooled to room temperature at a rate of ~30 K/min, and ~0.1-μm-thick contacts to the channel and gate were formed by thermal deposition of Ag. The gate area was 7.36×10^{-4} cm^2. Figure 1 shows a schematic diagram of the FET structure studied.

Sample FET structure characteristics. A rather large resistance (~2 MΩ) of the transistor channel hindered the direct investigation of the PLZT layer properties in the transistor structure. For this reason, we prepared special sample structures with a 100-nm-thick ferroelectric film deposited onto a a thick LSCO layer with a lower resistance (~0.1 MΩ). Using these samples, we studied variation of the ferroelectric polarization with the applied field strength by the Tower–Soyer method at a frequency of 100 Hz. The resulting dielectric hysteresis loop had a shape typical of ferroelectrics, with a saturation polarization of $P_s \approx$ 40–45 μC/cm^2, a residual polarization of $P_r \approx$ 20–30 μC/cm^2, and a coercive field strength of $E_c \approx 3 \times 10^5$ V/cm.

Figure 2 shows a typical current–voltage characteristic of the ferroelectric gate insulator in the transistor

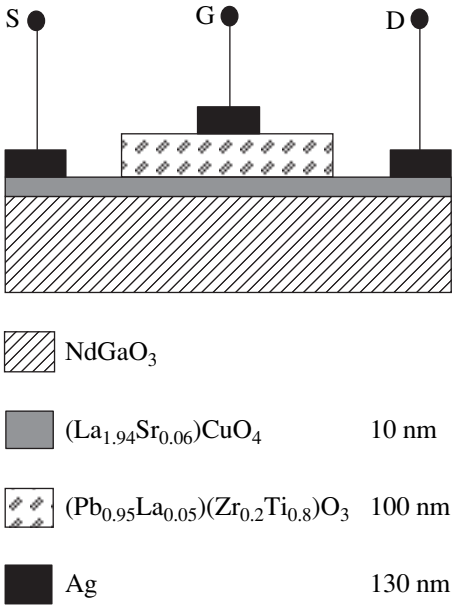

Fig. 1. A schematic diagram of the FET structure (S, G, D denoting the source, gate and drain electrodes, respectively). Bottom insets indicate the transistor layer compositions and thicknesses.

structure studied. An analysis of conductivity of the PLZT films is a nontrivial task because this system features both the intrinsic leaks (controlled by the charge carrier injection through interface, the bulk space charge, and the injected carrier trapping by charge traps) and the time-dependent current component due to the dielectric relaxation determined by the method of measurements, sample prehistory, and some other factors [4].

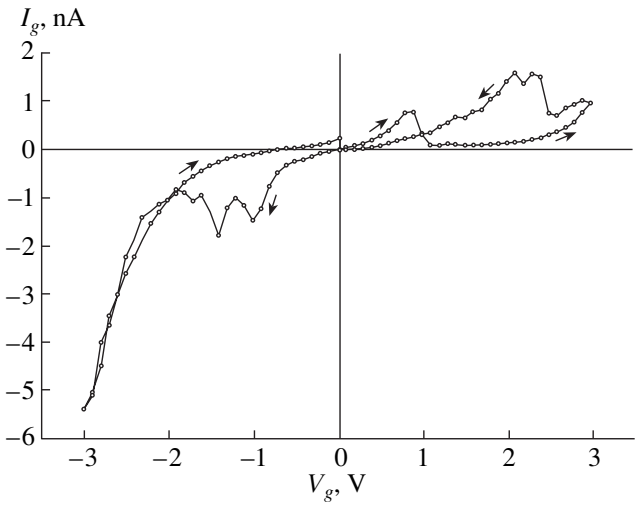

Fig. 2. The plot of gate leak current versus voltage for a single cycle measured at a zero voltage across the channel. Arrows indicate directions of the gate voltage variation.

Discussion of results. In this short communication, we are not intending to present a detailed analysis of leak currents in the PLZT structure and only briefly comment some general features of the current–voltage characteristic. The I_g versus V_g curve (Fig. 2) is asymmetric: for the positive bias voltage (plus on metal), the curve shape is determined primarily by the reverse-bias PLZT/Ag Schottky barrier and for the negative voltage, by two direct-bias barriers (PLZT/Ag and LSCO/PLZT) and the intrinsic resistance of the PLZT layer [5]. The current hysteresis observed in the cycle of increasing and decreasing voltage amplitude probably reflects the polarization properties of the ferroelectric layer [6]; the current maxima can be related to the relaxation processes involving charge carrier trapping and release from traps [4].

The X-ray diffraction patterns (CuK_α radiation) measured on the control LSCO/PLZT samples with 100- and 10-nm-thick ferroelectric layers showed evidence of a predominant *c*-orientation in both PLZT and LSCO layers. The lattice parameter determined using the (004) refection for LSCO (~1.5% mismatch with substrate) is c = 13.157 Å (in good agreement with published data [7]), while the crystallite size along the *c*-axis (evaluated from the peak width) is about 10 nm. These data show evidence of a rather high film crystallinity in the channel. For PLZT, the lattice constant determined using the (001) reflection is c = 4.094 Å (in god agreement with [8]), while the crystallite size in the direction perpendicular to the substrate is about 6 nm.

An analysis of the temperature variation of the transistor channel conductivity in the range from 30 to 330 K shows that the charge transfer is controlled by the hopping mechanism with variable jump length and determined by the Coulomb gap at the Fermi level:

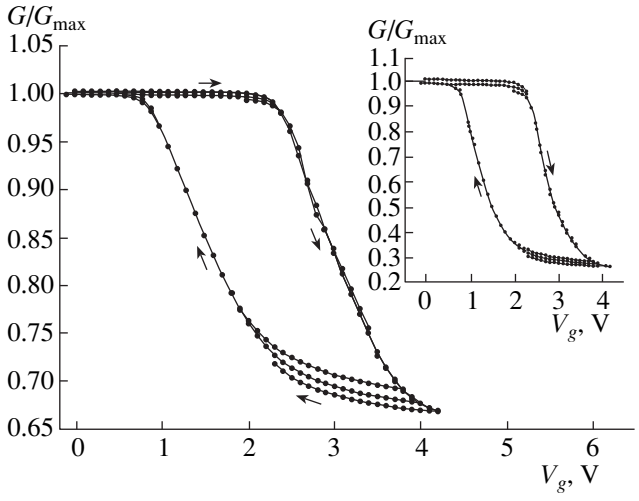

Fig. 3. The plots of channel conductivity (normalized to maximum) versus gate voltage for three cycles of measurement. Arrows indicate directions of the gate voltage variation. The inset shows the conductivity variation calculated for a channel part under the gate by subtracting the resistance of non-modulated regions from the total channel resistance.

$\sigma \sim \exp\{-(T_0/T)^{1/2}\}$ [9]. Using the parameter T_0 = 7600 K determined from the conductivity versus temperature plots, we may estimate the charge carrier localization radius a = 12 Å. Note that an analogous behavior of the conductivity ($\sigma \sim \exp\{-T^{1/2}\}$) was observed in La_2CuO_4 single crystals in the direction parallel to the Cu–O planes [10]. As is known, LSCO exhibits conductivity of the hole type. The room-temperature charge carrier concentration in the channel, evaluated from the conductivity value assuming that the carrier mobility, is $\mu = 1$ cm^2/(V s), is $p \sim 3 \times 10^{18}$ cm^{-3}.

In the FET structure studied, the length of the channel part in which the conductivity modulation took place (i.e., that covered by the gate) was ~20% of the total channel length. Figure 3 shows a plot of the room-temperature conductivity in the whole channel versus the gate voltage V_g (measured relative to the drain electrode). The conductivity is normalized to the maximum value (~6×10^{-7} Ω^{-1}). As seen, the plot resembles the classical hysteresis loop characteristic of the ferroelectric polarization as function of the applied voltage. This is quite natural since the channel conductivity variation is directly related to a change in the hole concentration affected by the transverse electric field at the gate. Here, the observed modulation amplitude is ~32%. The inset in Fig. 3 shows the same plot upon subtraction of the resistance of nonmodulated regions from the total channel resistance; the effective modulation amplitude is ~73%.

For a voltage of 5.1 V across the channel, the central potential of the channel region under the gate (relative to the drain electrode) is approximately 2.4 V. Thus, the abscissa of the hysteresis loop center in Fig. 3 is $V_g \approx$ 2.4 V, which corresponds to a zero average voltage on the ferroelectric layer. The voltage drop across a part of the channel under the gate is rather large (~1.5 V). This means that the voltage on the ferroelectric layer and, hence, the modulation amplitude significantly vary over the modulated part of the channel. In the region of maximum bias, the modulation may exceed the maximum value (~73%) calculated above. Note that a gate leak current in all experiments did not exceed 1% of the amplitude of the current variation in the transistor channel.

Conclusion. We have demonstrated for the first time that an all-perovskite LSCO/PLZT/Ag field-effect transistor allows for a strong (>70%) modulation of conductivity under the action of the PLZT ferroelectric gate insulator polarization. Being appropriately developed, a transistor of this type may serve as a unit cell in an energy-dependent memory with nondestructive readout. Of course, this development would encounter the problems typical of ferroelectrics, concerning degradation in the course of repeated write/read cycles, storage time, operation speed, etc. We are planning works on these problems.

Acknowledgments. The authors are grateful to K.D. Tsendin for fruitful discussions. This work was partly supported by the Ministry of Science, project no. 30696.

REFERENCES

1. Y. Watanabe, Appl. Phys. Lett. **66** (14), 1770 (1995).
2. C. H. Ahn, R. H. Hammond, T. H. Geballe, *et al.*, Appl. Phys. Lett. **70** (2), 206 (1997).
3. I. V. Grekhov, L. A. Delimova, I. A. Liniĭchuk, *et al.*, Sverkhprovodimost': Fiz., Khim., Tekh. **3** (1), 1708 (1990).
4. I. Stolichnov and A. Tagantsev, J. Appl. Phys. **84**, 3216 (1998).
5. Y. Watanabe, Phys. Rev. B **59**, 11257 (1999).
6. A. Taganstsev, A. Kholkin, E. Colla, *et al.*, Integr. Ferroelectr. **10**, 189 (1995).
7. F. Chou, J. Cho, and D. Johnston, Physica C (Amsterdam) **197**, 303 (1992).
8. Yu. Boikov, S. Esayan, Z. Ivanov, *et al.*, Appl. Phys. Lett. **61** (5), 528 (1992).
9. B. I. Shklovskiĭ and A. L. Efros, *Electronic Properties of Doped Semiconductors* (Nauka, Moscow, 1979; Springer-Verlag, New York, 1984).
10. S.-W. Cheong, Z. Fisk, R. Kwok, *et al.*, Phys. Rev. B **37**, 5916 (1988).

Translated by P. Pozdeev

Technical Physics Letters, Vol. 27, No. 1, 2001, pp. 20–24. Translated from Pis'ma v Zhurnal Tekhnicheskoĭ Fiziki, Vol. 27, No. 1, 2001, pp. 47–57.

The Nonlinear Dynamics of the Interface between Media Possessing Different Densities and Symmetries

N. B. Volkov*, A. E. Maĭer, and A. P. Yalovets****

** Institute of Electrophysics, Ural Division, Russian Academy of Sciences, Yekaterinburg, Russia*

*** Chelyabinsk State University, Chelyabinsk, Russia*

e-mail: nbv@ami.uran.ru

Received July 18, 2000

Abstract—A time-saving method is proposed for the study of a nonlinear vortexless stage of a Rayleigh–Taylor (RT) instability development at the free surface of a heavy liquid or a Richtmyer–Meshkov (RM) instability at the interface between continuous media possessing different densities and symmetries. The efficacy of the proposed method is demonstrated by the results of a special numerical experiment. It is shown that instability development at the solid–plasma interface gives rise to stresses in the solid. *© 2001 MAIK "Nauka/Interperiodica".*

An interesting problem for investigation is offered by the nonlinear dynamics of the free surface of a liquid or a contact boundary (interface) between two media possessing different densities and symmetries, either occurring in a gravitational (gravitational Rayleigh–Taylor instability) or magnetic field (magnetohydrodynamic Rayleigh–Taylor instability [1]) or driven by an external pressure pulse of arbitrary shape (Richtmyer–Meshkov instability [2, 3]). Studying these problems is of considerable fundamental and practical importance [4], in particular, for solving the task of creating plasma sources of high-power X-ray radiation [5]. It should be noted that a strong turbulence developed in the late nonlinear stages of the above instabilities [6, 7] is beyond the scope of our analysis.

Both linear and nonlinear (vortexless) stages of the Rayleigh–Taylor (RT) and Richtmyer–Meshkov (RM) instability development are studied in sufficient detail (see [1, 2, 4, 8–10]). However, generalization of the methods used in the cited works to the case of arbitrary time variation of the external potential field meets serious problems. Application of these theories to describing the interface dynamics in a curvilinear coordinates also encounters considerable difficulties. It is also difficult to apply all these theories to an interface between media with different symmetries, in particular, for description of the dynamics of a boundary between solids and plasmas generated by charged particle beams or laser radiation.

Below, we propose a time-saving method for the study of a nonlinear vortexless dynamics of an interface between incompressible liquids in the case of arbitrary time variation of the external field potential and various symmetries of the media on different sides of the interface. In a vortexless incompressible liquid, the velocity potential is a harmonic function and, hence, is uniquely determined by the boundary conditions. This circumstance allows a closed system of differential equations describing the interface to be formulated, excluding from consideration the bulk flows in both media. A solution to the problem of instability development at the interface can be used as a boundary condition in solving the equations of continuum mechanics. By jointly solving the equations describing the interface dynamics and the equations of continuum mechanics for a solid, we may take into account the influence of the elastic-plastic properties of the medium on the instability development and the effect of surface perturbations on the distribution of physical fields in the system.

For simplicity, the principal ideas of the proposed method are initially formulated in application to a free boundary and then generalized to the case of an interface between continuous media with different properties and symmetries.

It is assumed that a (generally three-dimensional) flow in a liquid is independent of one coordinate, for example, z (the proposed method is readily generalized to the 3D case). Excluding from consideration the late turbulent stage of the instability development, we set the shape of a free surface representing the upper boundary of the incompressible liquid by a single-valued function of the type $y = Y(x, t)$. Variation of the velocity field potential φ along the boundary is described by the Bernoulli equation [11]

$$\frac{\partial \varphi(x, Y, t)}{\partial t} + \frac{1}{2} v^2(x, Y, t) + G(x, Y, t) = 0, \qquad (1)$$

where G is the external field potential. The phase velocity of the liquid boundary is determined by a kinematic condition physically meaning the absence of a sub-

stance flux across the free surface:

$$\frac{\partial Y}{\partial t} = v_y(x, Y, t) - v_x(x, Y, t)\frac{\partial Y}{\partial x}. \quad (2)$$

Equations (1) and (2) are the boundary conditions for the velocity potential that is harmonic in the bulk. Assuming that the motion of medium in the bulk is determined only by evolution of the boundary, we arrive at a closed system of equations.

Since the parameters of the liquid are homogeneous along the z-axis, the derivative of the potential with respect to x is equal to the x-component of the tangential velocity (v_τ) and we may write

$$\frac{\partial \varphi(x, Y, t)}{\partial x} = v_x(x, Y, t) + v_y(x, Y, t)\frac{\partial Y}{\partial x}. \quad (3)$$

To close the set of Eqs. (1)–(3), we may use the condition of incompressibility and the boundary condition $v(x, y = -\infty, t) = 0$. Using an expression for the stream current on the free surface $\psi(x, Y, t) = \int_{-\infty}^{Y(x,t)} v_x(x, y, t)dy$, the condition of incompressibility, and Eq. (2), we obtain

$$\frac{\partial Y}{\partial t} + \frac{\partial \psi(x, Y, t)}{\partial x} = 0. \quad (4)$$

Taking into account a decay of the velocity potential in depth and the condition of incompressibility, the above expressions can be written as

$$\psi(x, Y, t) = \int_{-\infty}^{Y(x,t)} \frac{\partial \varphi(x, y, t)}{\partial x}dy = H(x, t)\frac{\partial \varphi(x, Y, t)}{\partial x}, \quad (5)$$

$$v_y(x, Y, t) = -\int_{-\infty}^{Y(x,t)} \frac{\partial^2 \varphi(x, y, t)}{\partial x^2}dy = -h(x, t)\frac{\partial^2 \varphi(x, Y, t)}{\partial x^2}, \quad (6)$$

where $H(x, t)$ and $h(x, t)$ are unknown functions satisfying the conditions of compatibility for Eqs. (5) and (6):

$$h = H\left(1 + \left(\frac{\partial Y}{\partial x}\right)^2\right)^{-1}, \quad \frac{\partial H}{\partial x} = \frac{\partial Y}{\partial x}. \quad (7)$$

Integrating the second relationship in (7), we obtain

$$H(x, t) = Y(x, t) - \gamma(t). \quad (8)$$

The quantity H can be interpreted as the effective perturbation depth and $y = \gamma(t)$, as a surface separating the perturbed and unperturbed regions of the medium. Integrating Eq. (8) with respect to x and differentiating the resulting expression with respect to time, we arrive (taking into account the incompressibility condition) at a relationship of the type

$$\dot{\gamma} = -\frac{1}{\lambda_m}\int_0^{\lambda_m} v_y(x, Y, t)dx, \quad (9)$$

where λ_m is the size of the perturbed region along the x-axis.

Equations (1), (4), (5), (8), and (9) present a closed set describing evolution of the boundary $Y(x, t)$. We accept the following boundary and initial conditions:

$$v_x(x = 0) = v_x(x = \lambda_m) = 0,$$

$$Y(x, t = 0) = Y_0 + a_0\cos(kx), \quad H(x, t = 0) = 1/k,$$

where $k = 2\pi/\lambda_m$ and Y_0 is the unperturbed surface coordinate.

The above set of equations is solved by numerical methods. Direct application of the lattice-point (finite difference) method leads to an unstable solution, which is explained by the absence of dissipative mechanisms (limiting the build-up of short-wavelength perturbations) in the model studied. Since a maximum growth rate in the ideal liquid is inherent in the short-wavelength perturbations, the stage of turbulent mixing comes earlier for these perturbations than for the long-wavelength ones. The appearance of small-scale turbulence leads to an effective truncation (caused by turbulent viscosity) of perturbations with large wavenumbers. This fact was taken into account by accomplishing forward and inverse Fourier transformations of the velocity potential increments. The inverse Fourier transform was determined taking into account only the long-wavelength perturbations. This approach provides for the stability of solution even when Eqs. (1) and (5) are integrated using the Euler scheme.

Now let us proceed to description of a system comprising a liquid with the density ρ_+ above another liquid with the density ρ_-, where $\rho_- < \rho_+$ (in what follows, the indexes "plus" and "minus" refer to the quantities describing the heavy and light medium, respectively).

According to the approach outlined above, a set of equations describing evolution of the boundary (interface) between the two liquids can be written in the following form:

$$\frac{\partial \varphi^\pm(x, Y, t)}{\partial t} + \frac{1}{2}(v^\pm(x, Y, t))^2 + G(x, Y, t) + \frac{P(x, Y, t)}{\rho_\pm} = 0, \quad (10)$$

$$\left(\frac{\partial Y}{\partial t}\right)^\pm + \frac{\partial \psi^\pm(x, Y, t)}{\partial x} = 0, \quad (11)$$

$$\psi^\pm(x, Y, t) = \pm H^\pm(x, t)\frac{\partial \varphi^\pm(x, Y, t)}{\partial x}, \quad (12)$$

$$H^{\pm}(x, t) = \pm Y(x, t) \mp \gamma^{\pm}(t), \quad (13)$$

$$\dot{\gamma}^{\pm} = -\frac{1}{\lambda}\int_0^{\lambda} v_y^{\pm}(x, Y, t)dx, \quad (14)$$

where P is the pressure. The condition of equality of the velocity components perpendicular to the interface yields

$$H^{+}\frac{\partial\varphi^{+}}{\partial x} = -H^{-}\frac{\partial\varphi^{-}}{\partial x}. \quad (15)$$

Substituting $\varphi^{-}(x, Y, t) = -\varphi^{+}(x, Y, t) + \eta(x, t)$ into Eq. (15), we obtain

$$\eta(x, t) = \int_0^{x}\left(1 - \frac{H^{+}(x', t)}{H^{-}(x', t)}\right)\frac{\partial\varphi^{+}}{\partial x'}dx' + \eta_0(t), \quad (16)$$

where $\eta_0(t)$ is an unknown function that has virtually no effect on the dynamics of interface and, therefore, can be taken equal to zero.

Excluding the pressure from Eqs. (10) and using Eq. (16), we obtain an equation for φ^{+}:

$$\frac{\partial\varphi^{+}}{\partial t} + \frac{1}{2}\left(1 + \left(\frac{\partial Y}{\partial x}\right)^2\right)^{-1}\left\{A\left(\frac{\partial Y}{\partial t}\right)^2 + \alpha\left(\frac{\partial\varphi^{+}}{\partial x}\right)^2\right\} + AG - \frac{1-A}{2}\frac{\partial\eta}{\partial t} = 0, \quad (17)$$

where $A = \dfrac{\rho_+ - \rho_-}{\rho_+ + \rho_-}$ is the Atwood number and $a(x, t) = \dfrac{1}{2}\left[(1 + A) + (1 - A)\left(\dfrac{H^{+}}{H^{-}}\right)^2\right]$. In Eq. (17), the only characteristic of the light liquid is the perturbation depth $H^{-}(x, t)$ that can be determined from Eqs. (13)–(15).

If the heavy liquid is replaced by a solid, the new properties of the bottom medium have to be taken into account by adding a term describing internal stresses to the right-hand part of Eq. (10) for φ^{+}. As a result, a new term appears in Eq. (17) as well, which has the form

$$S(x, Y, t) = \frac{1}{\rho_+}\left\{\int_0^{x}\left(\frac{\partial\sigma_{xx}}{\partial x} + \frac{\partial\sigma_{xy}}{\partial y}\right)_Y dx' + \int_0^{x}\left(\frac{\partial\sigma_{yx}}{\partial x} + \frac{\partial\sigma_{yy}}{\partial y}\right)_Y\frac{\partial Y}{\partial x'}dx'\right\}, \quad (18)$$

where $(\ldots)_Y$ indicates that the corresponding derivatives of the stress tensor components are calculated on the interface and the integration is performed over the boundary. Expression (18) is calculated in solving the equations of continuum mechanics.

Let us consider a solution to the problem of the RM instability development for $A = 1$ in the initially resting liquid subjected at $t = 0$ to the action of an instantaneous pulsed potential $G(x, y, t) = -U\delta(t)y$. Integrating the Bernoulli equation (1) with respect to time from

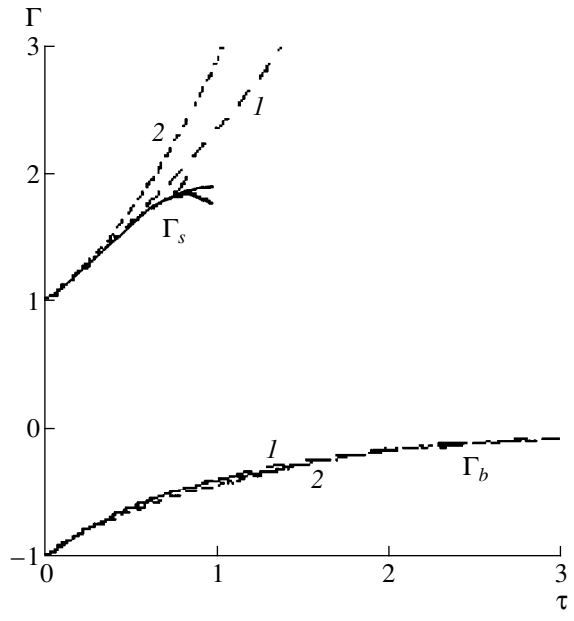

Fig. 1. Plots of the growth rate (normalized to the linear values) for a bubble $\Gamma_b = \dot{Y}_b / \dot{Y}_{RM}$ and a stream $\Gamma_s = \dot{Y}_s / \dot{Y}_{RM}$ calculated for two different values of the Atwood number $A = 1.0$ (*1*) and 0.1 (*2*) in comparison with the data (solid curve) taken from [9].

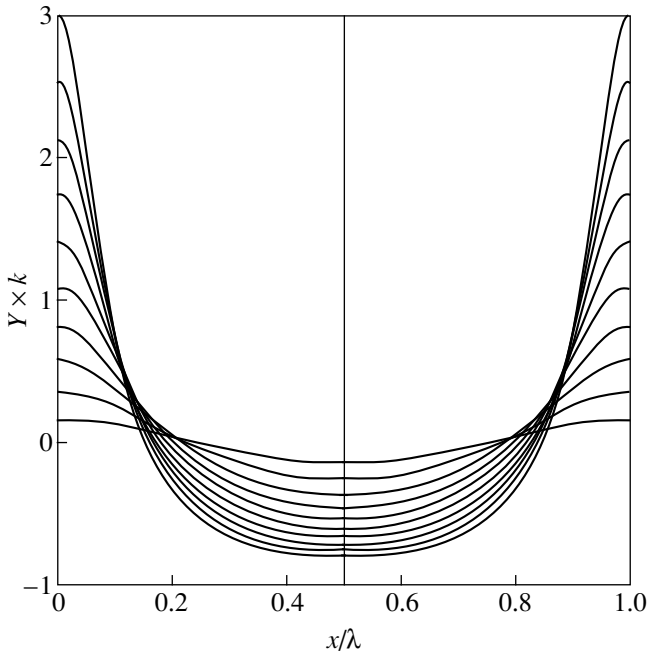

Fig. 2. The profiles of a free interface $Y(x, t)$ calculated for the sequential time instants $\tau = 0.15, 0.30, 0.45, \ldots, 1.50$ ($A = 1$).

$t = -0$ to $t = +0$, we obtain an initial condition for the potential

$$\varphi(x, t = +0) = AUY(x, 0). \quad (19)$$

The initial perturbation was described by a harmonic law with the amplitude $a = 0.001\lambda$. A linear theory [2] yields a constant growth rate of the perturbation amplitude: $\dot{Y}_{RM} = AUk$.

Figure 1 shows the plots of the growth rate (normalized to the linear values) for a bubble $\Gamma_b = \dot{Y}_b / \dot{Y}_{RM}$ and a stream $\Gamma_s = \dot{Y}_s / \dot{Y}_{RM}$ calculated for two different values of the Atwood number. The curves are constructed against the dimensionless time $\tau = (k^2AUa)t$. For comparison, we have also plotted the data taken from [9], where the solution was obtained in the form of a power series. Beyond the domain of convergence, the solutions in [9] were obtained in an approximate form (the approximations of different orders for s exhibited divergence).

Figure 2 presents the profiles of interface $Y(x, t)$ calculated for the sequential time instants $\tau = 0.15$, 0.30, 0.45, …, 1.50 ($A = 1$). The initial harmonic profile transforms into a bubble with flat bottom and long narrow streams. As seen from Figs. 1 and 2, the results of our calculations agree with the data taken from [9] (within the domain of applicability of that model). However, our method provides the description for a later stage of instability development as compared to the model used in [9].

Exposure of a solid target to intensive beams of charged particles of laser radiation with a radiant power density above 10^8 W/cm^2 leads to the formation of plasma that acts upon the solid boundary to impart it acceleration on the order of 10^8–10^{11} m/s^2. This leads to the RT type instability development, which produces deformation of the solid and gives rise to stress fields. The stress field amplitude is comparable with the amplitude of stress waves generated by the conventional thermoelastic mechanism.

Figure 3 shows evolution of the stress field (t = 100 ns) developed in a copper target under the action of a medium accelerated to 10^{10} m/s^2, the acceleration pulse lasting for 100 ns. Such acceleration pulses are observed in metal targets irradiated by pulsed electron beams with a current density on the order of several tens kA/cm^2. The elastic-plastic flows in the solid were calculated by a method described in [12].

Thus, the proposed method of calculation of the RT and RM instability development gives results that are in good agreement with the other published data and allow, in combination with a solution to the equations of continuum mechanics, the elastic properties of a particular medium to be taken into account. It should be noted that description of the stress fields arising in irradiated solids as a result of instability development at the plasma–solid interface is the task of principal importance for the study of material modification by intense radiation beams.

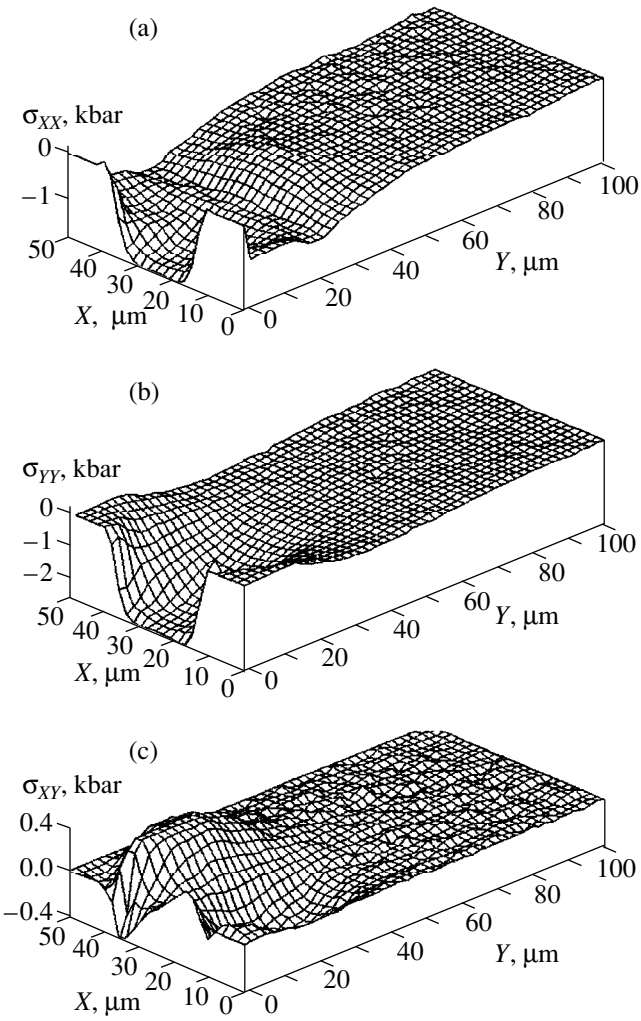

Fig. 3. Evolution of the stress field (t = 100 ns) developed in a copper target under the action of an electron beam with a current density of several tens kA/cm^2.

Acknowledgments. This study was partly supported by the Ministry of Education of the Russian Federation (project no. 97–24–7.1–38).

REFERENCES

1. S. Chandrasekhar, *Hydrodynamic and Hydromagnetic Stability* (Clarendon, Oxford, 1961).
2. R. D. Richtmyer, Commun. Pure Appl. Math. **12**, 297 (1960).
3. E. E. Meshkov, Izv. Akad. Nauk SSSR, Mekh. Zhidk. Gaza **5**, 151 (1969).
4. D. H. Sharp, Physica D (Amsterdam) **12**, 3 (1984).

5. D. D. Ryutov, M. S. Derzon, and M. K. Matzen, Rev. Mod. Phys. **72**, 167 (2000).
6. N. A. Inogamov, Pis'ma Zh. Tekh. Fiz. **4**, 743 (1978) [Sov. Tech. Phys. Lett. **4**, 299 (1978)].
7. O. M. Belotserkovskiĭ, *Numerical Experiment in Turbulence: from Order to Chaos* (Nauka, Moscow, 1997).
8. E. Fermi, in *Scientific Works* (Nauka, Moscow, 1972), Vol. 2, p. 493; E. Fermi and J. Neiman, *ibid*, p. 498.
9. A. L. Velikovich and G. Dimonte, Phys. Rev. Lett. **76**, 3112 (1996).
10. V. E. Neuvazhayev and I. E. Parshukov, in *Mathematical Modeling and Applied Mathematics*, Ed. by A. A. Samarsky and M. P. Sapagovas (IMACS, North-Holland, 1992), p. 323.
11. L. D. Landau and E. M. Lifshitz, *Course of Theoretical Physics*, Vol. 6: *Fluid Mechanics* (Nauka, Moscow, 1988; Pergamon, New York, 1987).
12. A. P. Yalovets, Prikl. Mekh. Tekh. Fiz. **38** (1), 151 (1997).

Translated by P. Pozdeev

Technical Physics Letters, Vol. 27, No. 1, 2001, pp. 25–28. Translated from Pis'ma v Zhurnal Tekhnicheskoĭ Fiziki, Vol. 27, No. 1, 2001, pp. 58–64.

A Lanthanum–Strontium Manganite: HF Absorption Features in the 2–30 MHz Frequency Range

V. A. Berezin*, K. V. Baginskiĭ*, V. A. Tulin*, D. A. Shulyatev, and Ya. M. Mukovskiĭ****

** Institute for Problems of Microelectronic Technologies, Russian Academy of Sciences, Chernogolovka, Moscow oblast, Russia*

*** Institute of Steel and Alloys, Moscow, Russia*

e-mail: berezin@ipmt-hpm.ac.ru; tulin@ipmt-hpm.ac.ru

Received August 11, 2000

Abstract—The RF magnetic response of a $La_{0.8}Sr_{0.2}MnO_3$ single crystal was studied in a frequency range from 2 to 30 MHz. The main contribution to the RF absorption in this range is related to the hysteresis losses. A new frequency-dependent anomaly in the HF absorption spectrum was observed and interpreted as being due to relaxation with a characteristic time above 10^{-7} s. The HF absorption measured as function of the field strength exhibits a sharp drop on approaching the saturation field, which makes the manganite studied a convenient material for the field and temperature sensors. © *2001 MAIK "Nauka/Interperiodica".*

Observed in recent years, a considerable growth in the number of publications devoted to the properties of manganites is explained primarily by the good prospects for using these materials in various transducers. In most of these investigations, the phenomenon of giant magnetoresistance was studied by dc techniques. To our knowledge, the RF properties of manganites were mostly studied in a different context, being related predominantly to the ferro- and paramagnetic resonance in the SHF range. However, the practical applications of magnetic transducers frequently require that the behavior of sensor material at lower frequencies (e.g., a few tens of MHz for the magnetoresistive sensors) be known as well. In addition, the attractive possibility of monitoring the transducer state by a contactless method is also rather simply implemented in the HF range.

In order to elucidate the behavior of manganites in this less studied frequency interval, we measured the HF magnetic response of a $La_{0.8}Sr_{0.2}MnO_3$ single crystal irradiated in a frequency range from 2 to 30 MHz.

The samples were prepared in the form of disks with a diameter of 2.8 mm and a thickness of 0.1 mm. The single crystal was oriented so that the crystallographic axis (110) was perpendicular (to within 5°) to the sample surface. For the HF absorption measurements, a sample was placed inside a helical coil with a diameter of 6 mm and a length of 12 mm representing a few dozen turns of a copper wire. The sample plane was vertical and parallel to the coil axis. The *LC*-circuit, comprising the coil with sample connected by a coaxial cable to a parallel capacitor, had a *Q*-value about 60. By varying the capacitance, the resonance frequency of the *LC*-circuit could be adjusted within desired limits.

The coil size (coefficient of filling) was selected in preliminary experiments so as to provide that the change in the *Q*-value related to the HF absorption in the sample would not exceed 30% (eventually, the coefficient of filling was set at about 2×10^{-3}). Once this condition is satisfied, we may assume that the change in height of the resonance absorption curve is proportional to the HF energy losses due to absorption in the sample [1]. Using small coupling capacitors, the *LC*-circuit was excited with a signal from a sweep generator and connected to a lock-in detector. Thus, the detector output signal was proportional to the HF losses in the sample. The HF magnetic field amplitude in the measuring coil was on the order of 0.1 Oe. The vector of the magnetic field created by the electric magnet was oriented in the horizontal plane. The magnet could be rotated in this plane.

We studied the HF absorption as a function of the applied magnetic field strength and temperature. Figure 1 shows the curves of the room-temperature HF absorption at 24 MHz measured for various directions of the magnetic field vector relative to the sample plane. The field orientation angle was measured from the normal to the sample surface. As is seen, even a rather large deviation of the magnetic field direction from the sample plane does not significantly affect the dependence of the HF losses in the sample on the field strength. This

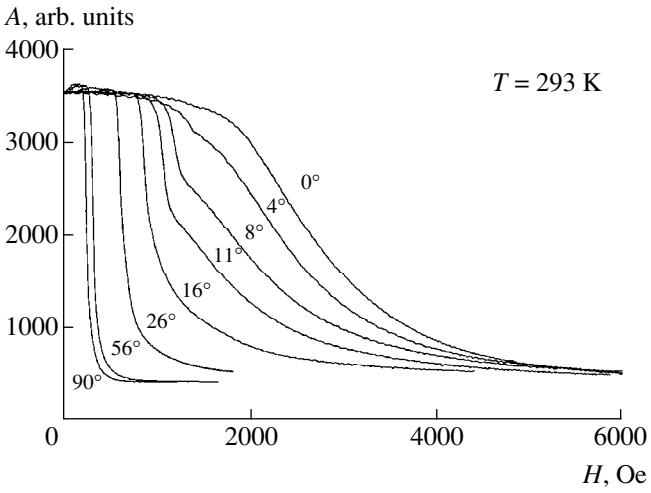

Fig. 1. The plots of room-temperature (T = 293 K) HF absorption (24 MHz) versus magnetic field strength measured for a lanthanum-strontium manganite single crystal with the magnetic field vector oriented at various angles relative to the sample surface normal.

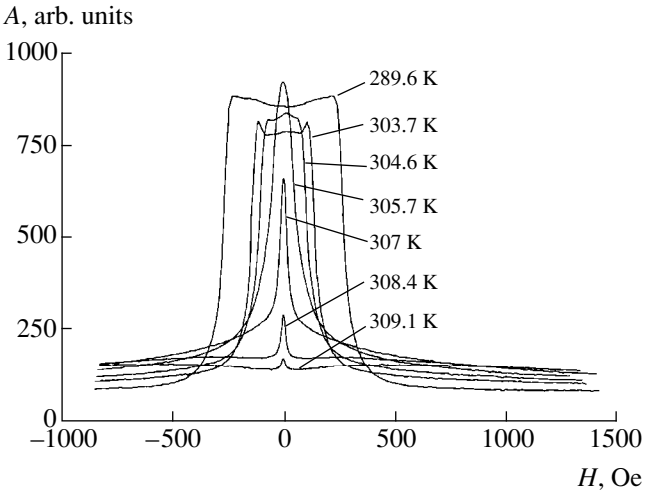

Fig. 2. The plots of HF absorption (24 MHz) versus magnetic field strength measured for a lanthanum-strontium manganite single crystal at various temperatures with the magnetic field oriented parallel to the sample surface.

fact indicates that no high-precision adjustment of the parallel orientation is required.

Besides the conventional shift of the absorption curve related to the effect of demagnetizing fields, the curves in Fig. 1 reveal two special features. These are the growth of absorption with the field strength in the initial stage, which becomes less pronounced when the field direction approaches the sample normal, and a noticeable break observed in the curves measured for the field orientations close to the normal. The latter break is apparently related to the preferred magnetization direction switching from parallel to perpendicular to the sample surface.

Figure 2 shows the curves of the HF absorption at 24 MHz measured at various temperatures for a magnetic field oriented parallel to the sample surface. Since the measuring system characteristics remain virtually constant in the whole temperature interval studied, all the significant variations are due to a change in the sample properties within a rather narrow temperature interval in the vicinity of the Curie point (for a given material, T_c = 305 K). It should be noted that the shape of the HF absorption curves is significantly different from that of the curves of magnetoresistance versus field strength measured by dc techniques.

Figure 3 presents a series of the curves of absorption at 288 K versus field strength measured at various frequencies. For better illustration, the curves are normalized in height so as to level the absorption at zero and very large field strengths. Note that the absorption maximum observed in Fig. 1 and manifested at higher temperatures in Fig. 2 (see the curve measured at 303.7 K) exhibits a pronounced frequency-dependent behavior.

Let us discuss the obtained results. As is known, there are two possible mechanisms of absorption losses in ferromagnetic materials exposed to HF magnetic fields. The first mechanism is related to the HF-field-induced currents passing through the sample, whereby the magnitude of losses is determined by the conductivity (magnetoresistance) of the material studied. The second type of losses is due to the HF magnetic field affecting the sample magnetization, inducing its periodic variation and leading to the energy dissipation (via hysteresis losses in the magnetization field range). Now, we will separately consider these mechanisms in application to the system under investigation.

As is known, applied magnetic fields strongly affect the conductivity of manganites and these effects were studied in sufficient detail (see, e.g., [2, 3]). Not dwelling much on the factors determining this behavior, we only note that manganite single crystals exhibit a monotonic decrease in their magnetoresistance with an increasing field strength (up to a few dozen kOe). However, the observed pattern is significantly different from that characteristic of the "giant" magnetoresistance effect revealed by dc measurements [4]. Our data (Fig. 2, curve for 289.6 K) show a rather sharp drop in the HF absorption at a field strength of ~250 Oe, which is followed by relatively small changes with the field strength increasing further. This behavior indicates that the main contribution to the HF absorption in the manganite samples studied is due to a factor other than magnetoresistance.

Now let us consider in more detail the mechanism related to the sample magnetization reversal in the applied HF magnetic field. At low frequencies, the sample magnetization "follows" the variable magnetic field in an "equilibrium" manner, as described by the corresponding partial hysteresis loop. Here, the magnitude of losses depends on the amplitude and frequency of an alternating field and on the strength of a constant magnetic field (the losses are proportional to the area of a partial hysteresis loop). As the magnetic field strength increases above the saturation level H_s, the area of the partial hysteresis loop drops to zero (paramagnetic process) and the HF losses decrease accordingly. Here, dependence of the HF losses on the field strength is determined by the shape of the complete hysteresis loop. Our manganite samples are characterized by a narrow hysteresis loop with virtually linear increase in magnetization with the field strength and rapid saturation [5].

This pattern qualitatively agrees with the system behavior at the magnetic field frequencies above 10 MHz. However, the absorption maximum observed in the HF absorption versus field strength plots can be explained by considering two mechanisms involved in the magnetization of ferromagnetic materials—the motion of domain boundaries (walls) and the rotation of magnetization in the domains—and taking into account that the magnetization response to the external action is not instantaneous. The motion of the domain walls is a quite rapid process, with a sufficiently short room-temperature characteristic time τ satisfying the condition $\omega\tau \ll 1$ (ω is the frequency of the external action). It should be noted that the absorption response with a shape similar to that above 10 MHz (Fig. 3) is observed even at frequencies as high as 10 GHz.

The magnetization curve of a ferromagnetic sample usually terminates in the regions featuring the magnetization reversal by means of a process other (and, apparently, slower) than the domain wall motion. The rate of the magnetization variation can be characterized by a relaxation time during which a given magnetic system comes to equilibrium with the external factors [6]. As the frequency of the external field increases, the instantaneous value of the sample magnetization gradually shifts in phase relative to the equilibrium value. This shift leads to the appearance of additional losses reaching maximum for $\omega\tau \sim 1$ (τ is the relaxation time and ω is the external field frequency). The further increase in the field frequency leads to a decrease in the additional losses, since the above magnetization reversal mechanism fails to follow the external factor at a necessary rate and the amplitude of magnetization variation drops.

Based on the above considerations, we may readily explain the appearance of a maximum in the HF absorption versus field strength curves measured at frequencies below 10 MHz. Indeed, this maximum must be manifested when the magnetization relaxation time

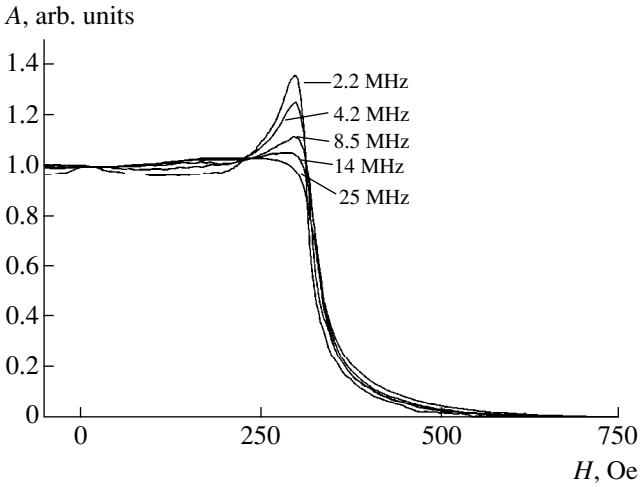

Fig. 3. The plots of HF absorption versus magnetic field strength measured at 288 K for a lanthanum-strontium manganite single crystal at various frequencies of the applied field. The curves are normalized in height so as to level the absorption at zero and very large field strengths.

depends on the magnetic field (in this case, because different magnetization mechanisms are operative in the system studied). The presence of this maximum indicates that the HF absorption level is higher and the relaxation frequency is markedly lower for the mechanism of magnetization reversal than for the domain wall motion. Our measurements did not reach the absorption maximum even at a lower frequency studied (~2 MHz), from which we infer that the room-temperature τ_{rot} value is greater than 10^{-7} s. The appearance of analogous maximum at a higher temperature for the measurements at 24 MHz reflects the temperature dependence of the of the relaxation time.

Thus, the RF absorption response of $La_{0.8}Sr_{0.2}MnO_3$ single crystals studied as function of the magnetic field strength in the 2–30 MHz frequency range is determined by magnetoresistance and hysteresis losses of the material. The magnetoresistance contribution to the HF absorption is markedly pronounced at temperatures in the vicinity of the Curie point, that is, in the region where the magnetoresistance is maximum (Fig. 2, curves for 304.6 and 303.7 K). The corresponding contribution to the total HF losses can be estimated using the slope of the curve of HF absorption versus magnetic field strength in the region of large fields ($H > H_s$). This contribution amounts to approximately 1/20 of the total HF absorption in the range of magnetization fields ($H < H_s$).

In the magnetic fields with $H < H_s$, the main contribution to the HF absorption response is due to the hysteresis losses. Here, about half of the total HF absorption variation falls within a 20-Oe interval in the vicinity of H_s. The observed nonmonotonic variation is related to the existence of different mechanisms of the

magnetization reversal in various magnetic fields, determining both the intensity of absorption and the relaxation frequency. The magnetic field strength at which the HF absorption exhibits sharp variation strongly depends on the temperature (at room temperatures, the variation rate is ~20 Oe/K). This behavior allows lanthanum–strontium manganites to be used in magnetic field and temperature sensors.

REFERENCES

1. V. A. Berezin, E. V. Il'ichev, and V. A. Tulin, Zh. Éksp. Teor. Fiz. **105** (1), 207 (1994) [JETP **78**, 110 (1994)].
2. É. L. Nagaev, Usp. Fiz. Nauk **166** (8), 833 (1996) [Phys. Usp. **39**, 781 (1996)].
3. L. P. Gor'kov, Usp. Fiz. Nauk **168** (6), 665 (1998) [Phys. Usp. **41**, 589 (1998)].
4. A. Urusibara, Y. Moritomo, T. Arima, *et al.*, Phys. Rev. B **51** (20), 14103 (1995).
5. O. Yu. Gorbenko, R. V. Demin, A. R. Kaul', *et al.*, Fiz. Tverd. Tela (St. Petersburg) **40** (2), 290 (1998) [Phys. Solid State **40**, 263 (1998)].
6. A. G. Gurevich, *Magnetic Resonance in Ferrites and Antiferromagnets* (Nauka, Moscow, 1973).

Translated by P. Pozdeev

Technical Physics Letters, Vol. 27, No. 1, 2001, pp. 29–31. Translated from Pis'ma v Zhurnal Tekhnicheskoĭ Fiziki, Vol. 27, No. 1, 2001, pp. 65–71.

Study of the Ozone Production and Loss during Oxygen Photolysis in a VUV Ozonator Chamber

V. V. Ivanov, N. A. Popov, O. V. Proshina, T. V. Rakhimova, G. B. Rulev†, and V. B. Saenko

Research Institute of Nuclear Physics, Moscow State University, Moscow, Russia

Received February 2, 2000

Abstract—The process of ozone production and loss during the oxygen photodissociation upon the absorption of radiation from an excimer lamp with a wavelength of 172 nm was studied by experimental and theoretical methods. Analysis of the experimental data within the framework of a one-dimensional numerical model showed evidence for the presence of a previously unknown mechanism of the heterogeneous ozone loss in a flow of atomic oxygen. *© 2001 MAIK "Nauka/Interperiodica".*

At present, the commercial production of ozone is based on using nonequilibrium processes in a barrier discharge plasma. However, efficiency of the ozone production by this method may significantly decrease as a result of the inhomogeneous structure of these discharges and the presence of a low-energy resonance in the dissociative sticking cross section of the ozone molecule discovered recently [1, 2]. An alternative way of effective ozone production is based on the process of oxygen photodissociation and related to the development of vacuum ultraviolet (VUV) radiation sources of a new type [3, 4].

Eliasson and Kogelshatz [4] revealed a significant discrepancy between the experimentally and theoretically predicted time variation of the ozone concentration. The rate constants for the ozone production and loss in the volume processes being well known, it was suggested [4] that the discrepancy can be related to a zero- dimensional numerical model used in the calculation. It should be noted that a certain difference between calculated and measured data on the ozone concentration was also observed in other investigations of the ozone production in discharge systems.

Another possible factor responsible for the discrepancy between experiment and theory can be the heterogeneous loss of ozone molecules on the reactor walls. The experiment with a VUV ozonator performed in this work was specially intended to assess the role of the surface processes on the ozone production and loss kinetics. For this purpose, we have also developed a self-consistent one-dimensional spatial reactor model. This model describes the spatial and temporal variations of all gas phase components, as well as those of the VUV radiation absorption.

Figure 1 shows a schematic diagram of the experimental setup. A VUV radiation beam with a initial intensity F_0 is absorbed in a flow of oxygen continuously supplied at a rate V_0 between a MgF_2 window *1* and a metal wall *2* spaced by the distance $L = 0.2$ mm. The ozonator chamber diameter is $D = 28$ mm. The oxygen flow rate in the ozonator chamber was measured with a digital gas flow meter of the ESS-60 type. The atomic oxygen formed as a result of the photodissociation is converted into ozone carried away from the reactor with the oxygen flow. The ozone concentration in the output gas flow was measured with a digital ozone meter of the Ozon-M3 type situated immediately at the exit hole of the ozonator chamber.

The VUV radiation was produced by an excimer lamp using a barrier discharge in pure Xe. The emission spectrum of the source (Fig. 2) represents a band centered at 1712 Å with a full width at half height about 120 Å. The output MgF_2 window of the VUV source is mounted on the input hole of the ozonator chamber. The absolute intensity of the VUV radiation was measured with an EG&G Model 550 photometer convert-

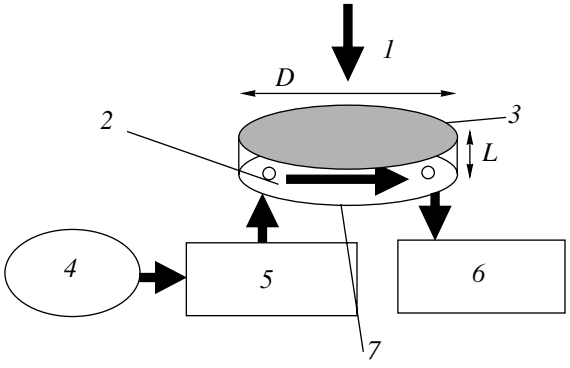

Fig. 1. Schematic diagram of the experimental setup: (*1*) VUV radiation beam; (*2*) steel wall; (*3*) MgF_2 window; (*4*) oxygen container; (*5*) gas flow rate meter; (*6*) ozone meter; (*7*) O_2 flow.

† Deceased.

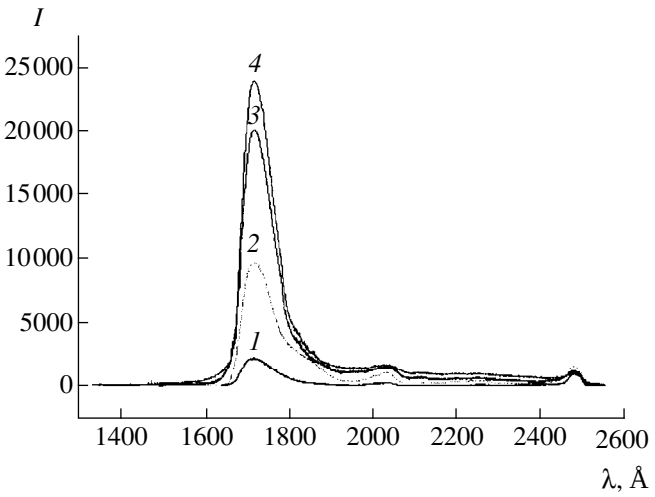

Fig. 2. Emission spectra of a VUV radiation source (excimer lamp) used in the experiment (intensity I in relative units) measured at a xenon pressure of (*1*) 0.25, (*2*) 0.5, (*3*) 1.0, and (*4*) 1.5 bar.

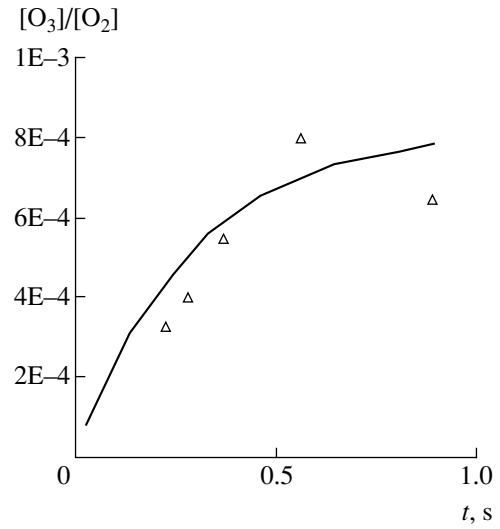

Fig. 3. The plot of relative ozone content in the oxygen flow versus the irradiation time (triangles, experimental data; solid curve, model calculation).

ing VUV into visible radiation with the aid of a sodium salicylate luminophor. Sodium salicylate is characterized by a constant quantum yield in a broad range of VUV frequencies. The VUV photometer was calibrated using an ArF laser and a laser power meter of the Labmaster type. The absolute intensity of the VUV radiation source measured by this setup was 3.6 mW/cm^2 at a working frequency of 20 kHz. Figure 3 shows an experimental plot of the time variation of the relative ozone content in oxygen flowing through the reactor.

The spatial distribution of various gas phase components in the reactor was studied within the framework of a specially developed one-dimensional spatial model. The chemical kinetics was described using a set of equations analogous to that used in [4]. Each of the five gas phase components [O_2, $O_2(a^1\Delta)$, $O_2(b^1\Sigma)$, $O(^3P)$, $O(^1D)$ and O_3] was described by a continuity equation

$$\frac{\partial N_i}{\partial t} = \frac{\partial}{\partial x}\left(D_i\frac{\partial N_i}{\partial x}\right) + R_i, \qquad (1)$$

where N_i is the concentration of particles of the ith type, D_i are the corresponding diffusion coefficients, and R_i is the total rate of the production and loss of particles of the ith type. The continuity equations were solved jointly with an equation describing the gas phase temperature T:

$$\frac{\partial\sum C_{p,i}N_iT}{\partial t} = \frac{\partial}{\partial x}\left(\chi\frac{\partial T}{\partial x}\right) + \sum Q_k, \qquad (2)$$

where $C_{p,i}$ is the heat capacity of the ith component, χ is the thermal conductivity coefficient, $\sum Q_k = \sum R_k\delta_k$ is the total energy change due to all chemical reactions, and R_k and δ_k are the rate and energy defect of the kth reaction. The set of equations (1) and (2) was supplemented by the initial conditions

$N_{O_2}(x)|_{t=0} = N_0$ (for oxygen molecules in the ground state),

$N_i(x)|_{t=0} = 0$ (for all other gas phase components),

$$T(x)|_{t=0} = T_0,$$

and by the boundary conditions for the particle fluxes

$$J_i(t)_{x=0;\,L} = \gamma_i\frac{N_iV_i}{4}\bigg|_{x=0;\,L}$$

(J_i is the flux to the reactor wall, V_i is the thermal velocity, and γ_i is the probability of heterogeneous loss on the wall for particles of the ith type) and for the wall temperature

$$T(t)|_{x=0;\,L} = T_{wall}.$$

The photodissociation process upon absorption of the VUV radiation by oxygen and ozone molecules is described by the following reaction scheme:

$$O_2 + h\nu \longrightarrow O(^3P) + O(^1D), \quad 155\text{ nm} < \lambda < 175\text{ nm}, \qquad (I)$$

$$O_2 + h\nu \longrightarrow O(^3P) + O(^3P), \quad 175\text{ nm} < \lambda < 190\text{ nm}, \qquad (II)$$

$$O_3 + h\nu \longrightarrow O(^1D) + O_2(b^1\Sigma, v), \qquad (III)$$

$$O_3 + h\nu \longrightarrow O(^3P) + O_2(A^3\Sigma, v) \longrightarrow 3O(^3P). \qquad (IV)$$

It was assumed that the absorption of VUV photons by ozone molecules via channels (III) and (IV) is

equiprobable, so that the corresponding quantum yields are $\eta(O^1D) = \eta(O_2b^1\Sigma) \cong 0.5$, $\eta(O^3P) \cong 1.5$. The photodissociation rate for each channel was determined by the formula

$$D_k(x) = \int_0^\infty J(\lambda)\sigma_k(\lambda)\exp(-\tau(\lambda, x))d\lambda, \qquad (3)$$

where $J(\lambda)$ is the spectral density of the radiation flux in the plane $x = 0$ normalized as $\int_0^\infty J(\lambda)d\lambda = F_0$ (where F_0 is the total radiation flux thorough the reactor window) and $\tau(\lambda, x)$ is the effective "optical thickness" of a gas layer with the geometric thickness x for absorption of the VUV radiation with a wavelength λ. The latter quantity is determined by the expression

$$\tau(\lambda, x) = \sum \sigma_k(\lambda)\int_0^x N_k(l)dl,$$

where $\sigma_k(\lambda)$ is the absorption cross section of the corresponding channel and N_k is the concentration of absorbing centers. Equation (3) takes into account that (because of the radiation absorption and internal refection in the MgF_2 window) the main part of the radiation entering into the ozonator is confined within a narrow cone around the normal to the window plane.

In our calculations, the radiation flux was taken equal to the experimentally measured VUV source intensity ($F_0 = 3 \times 10^{15}$ cm^{-2} s^{-1}) and the gas layer thickness was $L = 0.2$ mm. The results of the calculation showed that the gas temperature is constant throughout the volume and equal to T_{wall}. This fact is explained by a relatively small value of E_0 (and, hence, slow gas heating in the course of photodissociation) and by the small layer thickness L (which implies rapid gas cooling due to thermal conductivity).

The spatial distribution of excited oxygen atoms $O(^3P)$ is determined by distribution of the photodissociation intensity of O_2 and O_3 molecules. In view of a rapid conversion of the $O(^3P)$ particles into ozone via a three-body volume reaction, the spatial diffusion of atomic oxygen was insignificant everywhere except for the near-wall regions. The distributions of O_3 and $O_2(a^1\Delta)$ molecules are spatially homogeneous because the system features no rapid room-temperature volume processes involving their formation and loss. Thus, the stationary concentrations of these components are determined by their diffusion and loss at the reactor walls.

As is well known, the probability of ozone loss on metal and glass surfaces exposed to pure ozone is rather low ($\gamma_{03} \sim 2 \times 10^{-11}$–$10^{-9}$). These estimates of γ_{03} were obtained for the wall surface interacting with an oxygen–ozone of pure ozone flows in the absence of a constant source of atomic oxygen in the system. However, these conditions by no means take pace in ozonators of the photodissociation or electric-discharge types. Therefore, the results of calculations using these γ_{03} values markedly differ from the measured data. A satisfactory agreement with the results of measurements (Fig. 3) can be obtained assuming a markedly greater probability of the ozone loss on the wall surface: $\gamma_{03} \sim 7 \times 10^{-6}$ (for a glass reactor).

In order to check for validity of this assumption concerning the γ_{03} value, we have numerically modeled the experiment described in [4] within the framework of our one-dimensional model. The VUV photon flux F_0 (3×10^{16} cm^{-2} s^{-1}) was estimated from the initial slope of the $\frac{dO_3}{dt}$ kinetic curve using a method described in [4]. The results of calculations with the surface ozone loss coefficient $\gamma_{03} \sim 7 \times 10^{-6}$ completely agree with the experimental data reported in [4]. This γ_{03} estimate for the glass surface implies that there must exist a mechanism of the surface ozone loss in the presence of atomic oxygen, which differs from the heterogeneous loss mechanism operative in pure ozone. We are planning detailed experimental and theoretical investigations of the heterogeneous ozone loss process aimed at elucidating this mechanism.

Acknowledgments. The work was supported by the Russian Foundation for Basic Research, project no. 98-02-16381.

REFERENCES

1. G. Shenn, J. D. Skalny, *et al.*, *Proceedings of the 12th Symposium on Application of Plasma Processes, Liptovsky Jan, Slovakia, 1999*, p. 103.
2. K. S. Klopovskiĭ, N. A. Popov, O. V. Proshina, *et al.*, Fiz. Plazmy **23**, 183 (1997) [Plasma Phys. Rep. **23**, 165 (1997)].
3. V. V. Ivanov, K. S. Klopovskii, Yu. A. Mankelevich, *et al.*, Laser Phys. **6**, 654 (1996).
4. B. Eliasson and U. Kogelshatz, Ozone: Sci. Eng. **13**, 365 (1991).

Translated by P. Pozdeev

Technical Physics Letters, Vol. 27, No. 1, 2001, pp. 32–36. Translated from Pis'ma v Zhurnal Tekhnicheskoĭ Fiziki, Vol. 27, No. 1, 2001, pp. 72–80.

Triplet Molecules of the D_5 Symmetry Group Based on C_{60} Fullerene

S. S. Moliver* and Yu. F. Biryulin**

** Ul'yanovsk State University, Ul'yanovsk, Russia*

*** Ioffe Physicotechnical Institute, Russian Academy of Sciences, St. Petersburg, Russia*

e-mail: biryulin@nano.ioffe.rssi.ru

Received July 4, 2000

Abstract—The possibility of observing a non-zero-spin triplet state in highly symmetric derivatives of fullerene molecules with five double bonds, representing isomers of the type D_5–C_{60} $(R - r_6 - R)_5$ (where R = H or CH_3), is assessed based on the results of quantum-chemical calculations. The energies of isomer formation (endo- and exothermal process for the hydrogenated and methylated isomers, respectively) and the energies of terms are determined. The ground state corresponding to a non-zero-spin triplet e_1^2 ($^3A_2$) occurs approximately 0.3 eV below the zero-spin states. The results can be interpreted within the framework of the tight binding approximation for the $p\pi$ basis set orbitals of fullerene molecules (representing radially directed C2*p* hybrid atomic orbitals). The character of the open electron shell of isomers, delocalized over a large fullerene surface, suggests that, with high probability, the above non-zero-spin triplet state (rather than the e_1^2 ($^1E_2$) state stabilized by the Jahn–Teller effect) is the ground state of the system. © *2001 MAIK "Nauka/Interperiodica".*

Introduction. Let us consider a chemical modification of C_{60} fullerene accompanied by partial saturation of the covalent bond r_6 separating two hexagonal faces of the fullerene molecule. The corresponding derivatives with *n* saturated bonds will be denoted by $C_{60}(R_1 - r_6 - R_2)_n$. Such a modification takes place, for example, in the case of methylation or hydrogenation (with both radicals representing methyl groups CH_3 and hydrogen atoms H, respectively). The chemical synthesis of fullerene-containing starlike polystyrenes [1] offers an example of the mixed saturation process leading to $C_{60}(CH_3 - r_6 - H)_n$, where methyl group denotes a polymer chain attached to the fullerene.

The tight binding model [2] and the quantum-chemical calculation [3] show that a change in the electron structure of the π electron shell upon this chemical modification is determined by influence of the nearest neighbor monomer unit (e.g., a methyl group). These theoretical conclusions were confirmed by optical spectra of the films and solutions of fullerene-containing starlike polymers with variable number *n* of covalently attached polymeric arms [2]. Of special interest are the fullerene isomers of high symmetry [3], first, because these compounds are characterized by a greater enthalpy of formation and, hence, are synthesized at a higher concentration; second, because the π electron shells of highly symmetric fullerene modifications may exhibit both orbital and spin degeneracy, after which the ground state may either exhibit the Jahn–Teller effect or possess a non-zero-spin triplet character.

Below, we apply quantum-chemical methods for theoretical analysis of the possibility of observing a non-zero-spin triplet state in highly symmetric isomers of the D_5–C_{60} $(R - r_6 - R)_5$ type. The first indication of this possibility was reported previously [3]. The approach to quantum-chemical calculations based on the open shell model (ROHF method) and the parametrization of atomic orbitals of carbon [4] showed good results in describing the vacancy structure of diamond [5] and the electron structure of three-dimensional graphite [6].

Quantum-chemical calculation. The D_5–C_{60} $(R - r_6 - R)_5$ isomers exhibit a saturated bond configuration of the "tropic" type [3] (see Fig. 1 and the table). The initial approximation (Hückel') for both isomers (hydrogenated and methylated) is characterized by uppermost molecular orbitals (MOs) with close energy values (singlet and orbital doublet). Therefore, the self-consistent calculation can be started with a state possessing either closed (a_2^2 configuration, $^1A_1$ term) or open (e_1^2 configuration, $^1E_2$, $^1A_1$, and $^3A_2$ terms) shell.

The ROHF coefficients for terms of the e_1^2 configuration [5] coincide in groups D_5 and C_{3v}. The calculation indicates that, despite the odd total number of elec-

trons and the covalent character of bonds, the ground states of both isomers are of the non-zero-spin triplet type. The energies of isomer formation (endo- and exothermal process for the hydrogenated and methylated isomers, respectively) and the energies of terms are as follows:

$$C_{60} + 5H_2 \longrightarrow C_{60}(H - r_6 - H)_5 - 6.9 \text{ eV},$$

$$\begin{cases} a_2^2(^1A_1) \\ e_1^2(^1E_2) \end{cases} = e_1^2(^3A_2) + \begin{cases} 0.23 \text{ eV} \\ 0.31 \text{ eV}, \end{cases} \quad (1)$$

$$C_{60} + 5C_2H_6 \longrightarrow C_{60}\,(CH_3 - r_6 - CH_3)_5 + 25.5 \text{ eV},$$

$$\begin{cases} e_1^2(^1E_2) \\ a_2^2(^1A_1) \end{cases} = e_1^2(^3A_2) + \begin{cases} 0.26 \text{ eV} \\ 0.32 \text{ eV}. \end{cases}$$

The electron structures of both isomers are clearly illustrated in Fig. 2 showing the highest occupied (HOMO) and lowest unoccupied (LUMO) molecular orbitals of fullerene molecule (center) [3] and isomers (left and right). The MO levels of open shells (open square symbols) are depicted in arbitrary positions because their orbital energies (determined by the ROHF method), in contrast to those of the closed and virtual shells, are not equal to the eigenvalues of the Fock matrix. For this reason, Koopman's theorem [7] of ionization and electron affinity is inapplicable to the orbital energies of open shells; their positions in Fig. 2 only indicate the electron configuration: all orbitals below these are fully occupied (closed shell) and the orbitals above are empty (virtual shell).

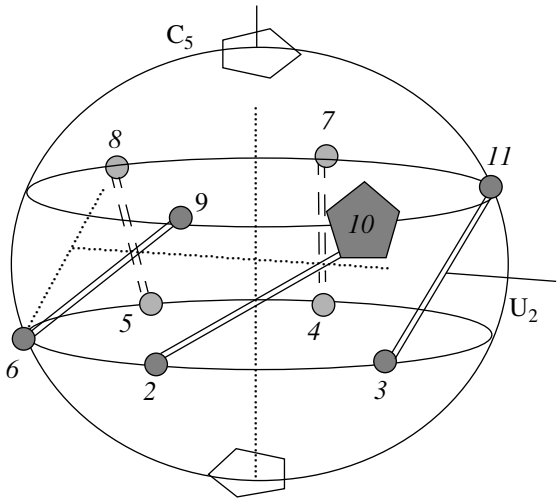

Fig. 1. A schematic diagram illustrating the "tropic" configuration of isomers. Carbon atoms of the fullerene are grouped in 12 regular pentagons with r_5 bond sides, representing truncated vertices of an icosahedron (for clarity, only some of the pentagons are depicted and their relative dimensions are decreased below the true proportion). The indicated r_6 bonds encircle one of the fifth-order axes; dihedral axes of the U_2 type are retained.

The MOs of isomers can be classified with respect to irreducible representations either using the signs of the MO LCAO coefficients for atoms passing into one another upon rotations about U_2 axes (in the case of nondegenerate MOs a_1 and a_2) or taking into account the partial electron densities, depending on whether the

MO character and representation expansions

D_5	E	$2C_5$	$2C_5^2$	$5U_2$	x_i	x_ix_k	
A_1	1	1	1	1		$(x^2 + y^2, z^2)$	$\alpha = \cos(\pi/5) = (1 + \sqrt{5})/4$
A_2	1	1	1	–1	z		$(2\alpha - 1)^2 = (3 - \sqrt{5})/2$
E_1	2	$2\alpha - 1$	-2α	0	(x, y)	(xz, yz)	$(2\alpha)^2 = (3 + \sqrt{5})/2$
E_2	2	-2α	$2\alpha - 1$	0		$(x^2 - y^2, xy)$	$2\alpha(2\alpha - 1) = 1$
I							D_5
G	4	–1	–1	0			$E_1 + E_2$
H	5	0	0	1			$A_1 + E_1 + E_2$
T_1	3	2α	$1 - 2\alpha$	–1			$A_2 + E_1$
T_2	3	$1 - 2\alpha$	2α	–1			$A_2 + E_2$

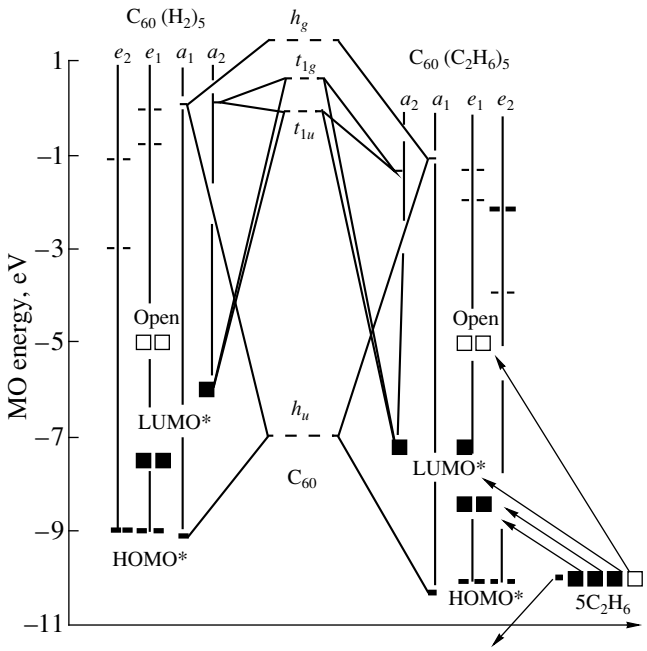

Fig. 2. A schematic diagram illustrating the formation of isomer molecular orbitals from the MOs of fullerene. Orbital energies (levels) of isomers are grouped in columns in accordance with their irreducible representations (see table) indicated at the vertical lines. Unoccupied MOs situated above the conventional open-shell level are indicated by thin bars. For nondegenerate MOs formed in the D_5 field, thin solid lines indicate the original MOs participating in their formation. Bottom right inset shows a conventional source of electrons doping the upper MOs of the isomers, representing ten electrons from the upper occupied orbitals of five ethane or hydrogen molecules according to scheme (1).

U_2 axes are nodal or not (MOs e_1 and e_2, respectively; see map (*g*) in Fig. 2).

Discussion of results. We will now demonstrate that the above results can be interpreted within the framework of the tight binding approximation for the $p\pi$ basis set orbitals of fullerene molecules (representing radially directed C2*p* hybrid atomic orbitals) [8]. These basis set orbitals form the electron shells with the I_h symmetry in a C_{60} fullerene molecule LUMOt_{1u}, (LUMO + 1)t_{1g}, (LUMO + 2)h_g, and HOMOh_u, the orbitals of which are illustrated in Fig. 2; on decreasing the symmetry, the orbitals split as indicated in the table (last column).

As seen from the MO scheme in Fig. 2, these shells of the fullerene molecule are sufficient to form a MO for any representation (from the standpoint of symmetry, even the shells above LUMO are not necessary for expanding the isomer MOs in terms of the fullerene orbitals). The question concerning a minimum number of basis set orbitals necessary for successful quantitative application of the tight binding approximation is answered by comparing the partial electron densities of the fullerene shells and the groups of isomer orbitals indicated by HOMO* and LUMO* in Fig. 2.

Figure 3 shows the electron densities mapped as isolines in the plane passing through the dihedral axis U_2. The total electron densities (a) and (b) illustrate the molecules of fullerene and its methylated isomer. The other maps in Fig. 3 show that orbitals of the methyl groups (or hydrogen atoms for the hydrogenated isomer) do not contribute to the partial electron densities and, hence, to the molecular orbitals in the indicated energy interval. Thus, the chemistry of saturation of double bonds in the fullerene molecule turns out to be similar to the case of semiconductor doping with donors, whereby the donor level is described by wavefunctions of the conduction band (analogous to the LUMO+*n* shells of the fullerene molecule).

Orbitals in the group denoted by HOMO* possess close energies and their irreducible representations can be used to expand the h_u orbital of fullerene. A small difference between the corresponding partial electron densities observed in maps (c) and (d) of Fig. 3 is evidence that the tight binding approximation is sufficient to describe the corresponding distinction by hybridization of the HOMO and LUMO of fullerene (this hybridization involves only the MO e_1 of the HOMO* group).

The irreducible representations of orbitals in the group denoted by LUMO* can be used to expand the t_1 orbital of fullerene. A difference between the partial electron density of this group from that of the LUMO group in maps (e) and (f) of Fig. 3 is rather large. From the standpoint of the tight binding approximation, this means that the hybridization of LUMOt_{1u} with a single shell of HOMO h_u is insufficient and it is necessary to take into account some other fullerene orbitals as well. The presence of two MOs a_2 in the separate part of the isomer spectrum indicates that description of the LUMO* group must first of all take into account the hybridization with (LUMO + 1)t_{1g}.

According to data in the table, only MO e_1 can be obtained by hybridization of the HOMO, LUMO, and LUMO+1 shells, while the other isomer MOs have a unique origin (as indicated in Fig. 2). Taking into account that the isomer spectrum contains a high-lying MO a_1 in addition to those forming the HOMO* group, we may conclude that the (LUMO+2) h_g shell [3] must be added to the basis set used in the tight binding approximation.

Since the multielectron effects in scheme (1) are decisive in determining the properties of the fullerene isomers studied, an important factor for the analytical methods based, for example, on the tight binding approximation, is the occupation of molecular orbitals. Figure 2 shows that an analysis based on the $p\pi$ basis set orbitals requires these to be filled with 18

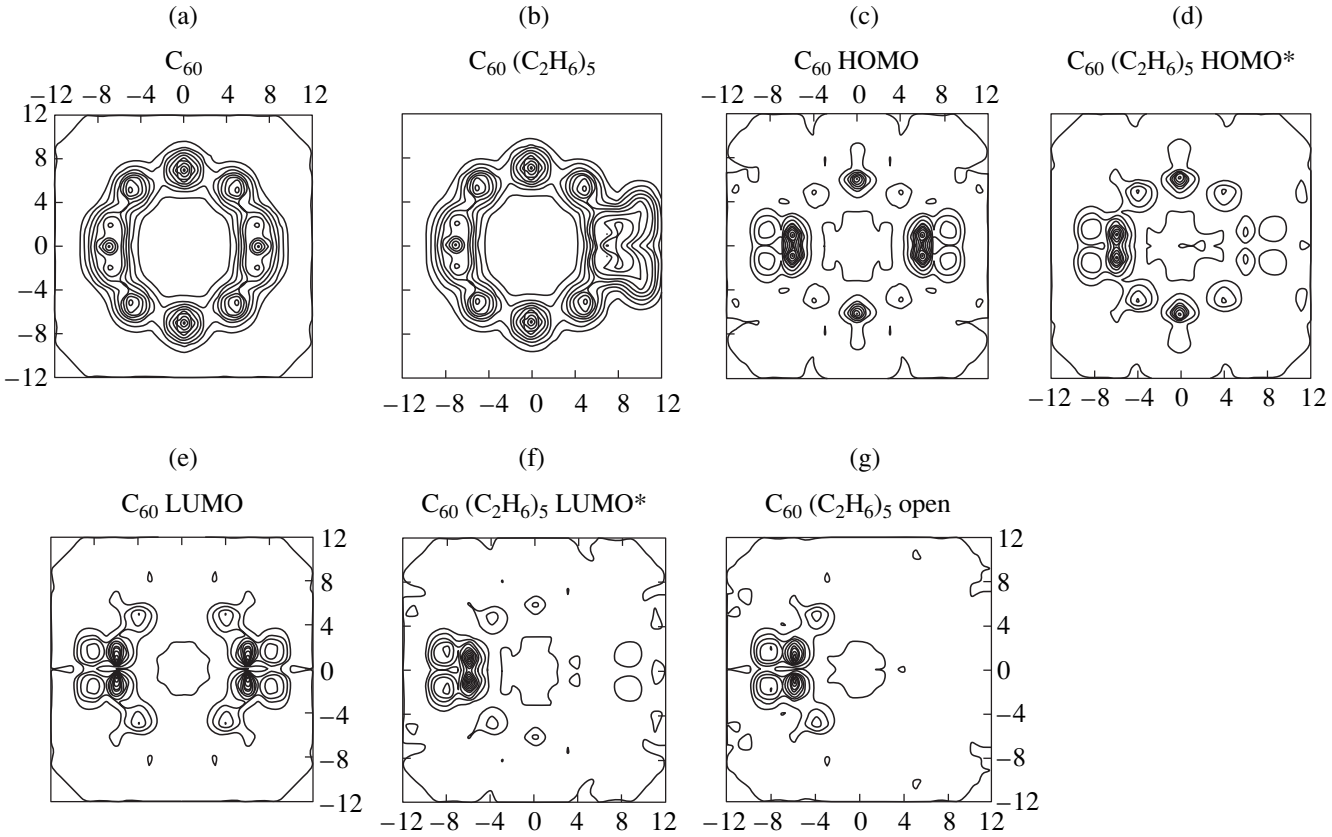

Fig. 3. Maps of total and partial electron densities: (a) fullerene; (b) methylated isomer (with two methyl groups saturating the r_6 bond); (c–g) partial densities for MO groups (HOMO, HOMO*, LUMO, LUMO*) indicated in Fig. 2. The coordinates of maps are expressed in atomic units (Bohr radius); the horizontal axis is oriented along U_2 (Fig. 1) and the vertical axis, along the corresponding saturated bond r_6.

electrons, including 10 electrons from the HOMO shell of fullerene plus 8 electrons from five ethane or hydrogen molecules in scheme (1). In terms of the tight binding approximation, 8 of 10 electrons from the outer shells of five molecules saturating fullerene are doping the LUMO and LUMO+1 shells, while the remaining electron pair occupies the MO situated deep in a filled shell of the isomers (as indicated by arrows in Fig. 2).

Map (g) in Fig. 3 illustrates the electron density distribution in the open isomer shell. According to the calculated scheme (1), this shell in the ground state $e_1^2(^3A_2)$ is populated with two electrons having the total spin 1. The electron density is weakly localized, being distributed between five double bonds r_6 [note that these are the inverse bonds (one of which is depicted by dashed line connecting pentagons 6 and 8 in Fig. 1) situated at the fullerene "tropic" between saturated bonds, rather than the saturated bonds themselves]. Since the MO method tends to understate the energies of non-zero-spin triplet states [7], it is necessary to point out that the delocalized character of the open electron shell in isomers (in contrast, for example, to the localized open shell of a vacancy in diamond [5]) suggests that, with high probability, the above-mentioned non-zero-spin triplet state (rather than the $e_1^2(^1E_2)$ state stabilized by the Jahn–Teller effect) is the ground state of the system. Moreover, the fullerene isomers possess a low-lying non-zero-spin triplet state even in the case of a strong Jahn–Teller effect (according to scheme (1), the stabilization energy must be about 0.3 eV), which makes these molecules an interesting object for molecular spectroscopy.

Acknowledgments. This study was supported by the Interinstitution Scientific-Technological Program "Fullerenes and Atomic Clusters" (project no. 98076 "Polymer-2") and by the Russian Foundation for Basic Research (project no. 98-02-03327).

REFERENCES

1. A. N. Aleshin, Yu. F. Biryulin, N. B. Mironkov, *et al.*, Fullerene Sci. Technol. **6** (3), 545 (1998).

2. Yu. F. Biryulin, V. S. Vikhnin, and V. N. Zgonnik, Fiz. Tverd. Tela (St. Petersburg) **42** (1), 188 (2000) [Phys. Solid State **42**, 197 (2000)].
3. S. S. Moliver and Yu. F. Biryulin, Fiz. Tverd. Tela (St. Petersburg) **42** (10), 1899 (2000) [Phys. Solid State **42**, 1952 (2000)].
4. S. S. Moliver, Fiz. Tverd. Tela (St. Petersburg) **38** (7), 2029 (1996) [Phys. Solid State **38**, 1119 (1996)].
5. S. S. Moliver, Fiz. Tverd. Tela (St. Petersburg) **42** (4), 655 (2000) [Phys. Solid State **42**, 673 (2000)].
6. S. S. Moliver, Fiz. Tverd. Tela (St. Petersburg) **42** (8), 1518 (2000) [Phys. Solid State **42**, 1561 (2000)].
7. R. McWeeny, *Methods of Molecular Quantum Mechanics* (Academic, London, 1982).
8. N. Laouini, O. K. Andersen, and O. Gunnarsson, Phys. Rev. B **51** (24), 17446 (1995).
9. R. Flurry, *Symmetry Groups. Theory and Chemical Applications* (Prentice-Hall, Englewood Cliffs, 1980; Mir, Moscow, 1983).

Translated by P. Pozdeev

Technical Physics Letters, Vol. 27, No. 1, 2001, pp. 37–40. Translated from Pis'ma v Zhurnal Tekhnicheskoĭ Fiziki, Vol. 27, No. 1, 2001, pp. 81–88.

Generation of Subnanosecond High-Voltage Pulses with a Peak Power of up to 300 MW and a Repetition Rate of 2 kHz

M. I. Yalandin, S. K. Lyubutin, S. N. Rukin, B. G. Slovikovskiĭ, M. R. Ul'maskulov, V. G. Shpak, and S. A. Shunaĭlov

Institute of Electrophysics, Ural Division, Russian Academy of Sciences, Yekaterinburg, Russia

Received August 9, 2000

Abstract—We report on the results of testing a hybrid subnanosecond modulator with an input resistance of 50 Ω based on an all-solid-state high-voltage nanosecond-pulse charging source with an inductive energy accumulator, a semiconductor current switch, and a pulse shaper with gas-discharge gaps. Use of the sharpening and cutting discharge gaps filled with hydrogen at a pressure of 100 atm ensured the stable formation of pulses with a peak amplitude of up to 140 kV and a pulse width of ~500 ps at a repetition rate of up to 2 kHz. © *2001 MAIK "Nauka/Interperiodica".*

Introduction. Solving the task of further development of the high-energy super-wideband electromagnetic pulse [1–3] and subnanosecond microwave pulse [4] generators requires modulators capable of switching pulsed signals at high peak and average power levels. Increase in the peak power is reached by increasing the output voltage, while the growth of average power is provided by increasing the pulse repetition rate.

There are special requirements with respect to stability of the output pulses, which has to be not worse than that provided by the subnanosecond-pulse modulators with semiconductor commutators [5]. However, the latter devices available at present exhibit restrictions with respect to both pulse amplitude and peak power. For example, the output commutator based on a fast-recovery drift diode capable of forming 1- to 2-ns-wide pulses was reported to provide for a maximum output peak power of 64 MW and a maximum pulse amplitude of 80 kV [6]. Using the retarded-ionization-wave diode pulse shapers, it is possible to obtain the output subnanosecond pulses with a leading front duration of about 200 ps, but at the expense of much lower values of the peak power (500 kW) and amplitude (5 kV) [5].

Generation of the high-power subnanosecond pulses is still possible only with the aid of devices based on the energy accumulators of a capacitive type (short pulse-forming lines) with spark-discharge commutators [7–9]. The discharge-gap commutators operating at a repetition rate above 100 Hz should be filled with hydrogen, whichprovides for the electric strength restoration at a sufficiently high rate [10]. In this case, the acceptable stability of operation can be achieved without using complicated gas purge [11] and/or controlled commutator systems [12, 13].

The contradictory requirement of combining a high electric strength of insulators employed in miniature subnanosecond-pulse capacitive energy accumulators and a high level of the breakdown overvoltage used in the discharge gap implies that a pulse-forming line must be charged within a very short time (a few nanoseconds). As is known, the scatter in the breakdown voltage of the discharge gap strongly depends upon stable operation of a source of the short charging current pulse (driver). Thus, the task of developing high-power modulators for the generation of subnanosecond high-voltage pulses requires creating nanosecond drivers providing for stable charging of the pulse-forming lines at sufficiently high pulse repetition rates.

Below, we report on the first results of testing an original hybrid high-rate modulator comprising a combination of a solid-state nanosecond driver with an inductive energy accumulator and a semiconductor current switch (SM-3NS) [14] and a subnanosecond pulse shaper based on ultrahigh-pressure gas-discharge gaps [8]. Creation of an experimental prototype of this device has became possible only upon thoroughly studying operation of the semiconductor commutator and finding regimes ensuring a driver output pulse duration of less than 10 ns [14]. The modulator prototype was tested at an output pulse repetition rate ranging from 100 to 2000 Hz. The discharge gaps were filled with a working gas (hydrogen) at a pressure of 100 atm. For the comparison, some experiments were performed with nitrogen-filled discharge gaps. The discharge gaps were operated without induced gas circulation.

System description. A nanosecond driver of the SM-3NS type represents a multistage energy accumulation system comprising several intermediate capacitor banks, a pulse transformer, and solid-state commutators (thyristors and magnetic saturation switches). The output circuit implements a serial scheme (Fig. 1) containing a capacitive energy accumulator, a magnetic

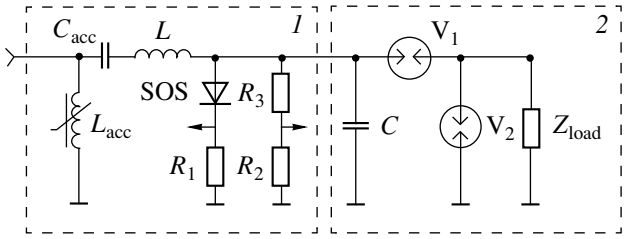

Fig. 1. A schematic diagram of the output stages of a subnanosecond pulse modulator capable of operating at a pulse repetition rate of up to 2000 Hz: (*1*) nanosecond pulse driver; (*2*) subnanosecond pulse shaper.

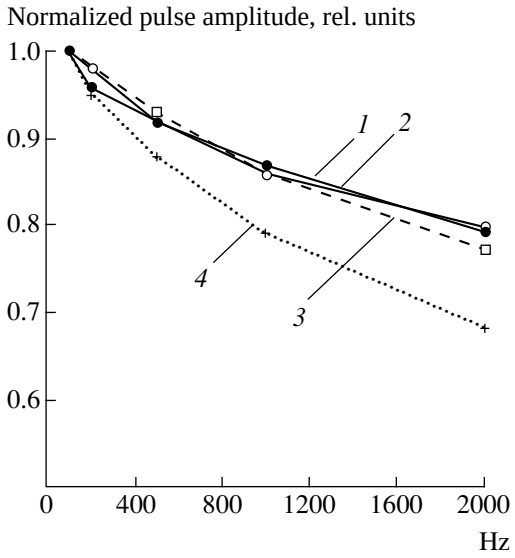

Fig. 2. Plots of the output pulse amplitude versus repetition rate: (*1*, *2*) nanosecond pulses of the driver loaded with 150 and 500 Ω, respectively; (*3*, *4*) subnanosecond pulses of the shaper with hydrogen- and nitrogen-filled discharge gaps, respectively.

switch, an inductive energy accumulator, and a high-current semiconductor commutator (comprising an SOS diode array [15]). The commutator was capable of switching an open-circuit voltage of up to 400 kV with a pulse width at half-height of ~6 ns. The driver provided for a pulse-train system operation at a repetition frequency of up to 2 kHz. The system parameters were monitored using a Tektronix TDS684 digital oscillograph operated in the signal accumulation (ENVELOPE) and averaging (over up to 1000 pulses) modes. The results of this monitoring showed that stability of the output current pulses fell within the rated registration accuracy for oscillographs of the type employed.

The SM-3NS driver was used as a current source to charge the pulse-forming line with a wave resistance of 50 Ω and capacitance of ~12 pF. The line is designed as a joint assembly with ultrahigh-pressure gas-discharge gaps operated at a gas pressure of up to 100 atm. Pulses of ~1 ns width were formed using a principle of the charging pulse sharpening and cutting, whereby switching on the sharpening discharge gap is followed at a certain controlled delay by operation of the cutting discharge gap. The discharge gaps operated in a common working gas medium. Both gaps could be smoothly adjusted immediately in the course of the system operation.

In the regime of maximum charging current and a pulse repetition rate of up to 100 Hz, the pulse-forming line charged up to a voltage of ~300 kV. The breakdown voltage of the sharpening discharge gap was selected an adjusted close to this level. We did not observe malfunctions (missing pulses) during the discharge gap operation. The modulator was loaded with a 50-Ω coaxial oil-filled line. The output signals of the pulse-forming line were monitored using a calibrated capacitive divider with a transient time of 120 ps.

Results and discussion. In these experiments, the driver was operated in a limited power regime determined by resistance of the mains line wires (3 × 380 V, 50 Hz). For this reason, an increase in the pulse repetition frequency to 2 kHz was accompanied by a gradual decrease in voltage on the input mains filter and on the subsequent driver stages. This led to a decrease in both forward and reverse pumping currents through the SOS diodes, as well as in the voltage on the inductive energy accumulator reached by the instant of the SOS diode current pulse termination.

Figure 2 shows the experimental curves of the driver output voltage measured as a function of the pulse repetition rate using two different load resistors; the data were normalized to the corresponding maximum values of the voltage amplitude observed in the 0–100 Hz frequency interval. The results of these measurements indicate that dynamics of the driver output pulse amplitude is independent of the load resistance. This fact was taken into account in determining a real decrease in amplitude of the subnanosecond output pulse at high pulse repetition rates in the modulator.

Figure 3 shows a series of the output pulse oscillograms measured at various pulse repetition rates in the subnanosecond modulator. Each time pattern was obtained by accumulating 500 pulses with a digital storage (stroboscopic) oscillograph of the Tektronix TDS820 type with a working frequency band of 6 GHz. The discharge gaps were filled either with hydrogen at 100 atm (Fig. 3a) or with nitrogen at 60 atm (Fig. 3b).

The gaps of dischargers filled with hydrogen (Fig. 3a) were adjusted at a modulator pulse repetition rate of 100 Hz so as to obtain stable pulses of maximum possible amplitude and minimum (~400 ps) duration (curve *1*) and remained unchanged in the course of subsequent experiments. Because of the aforementioned feature in operation of the nanosecond driver, the charging voltage amplitude in the pulse-forming line exhibited a 20–21% decrease when the pulse repetition frequency increased from 100 to 2000 Hz (Fig. 2, curves *1* and *2*). A decay in amplitude of the subnano-

second output pulse was ~23%. Constructed using the data normalized to the maximum amplitude (measured at a pulse repetition rate of 100 Hz) this plot (Fig. 2, curve *3*) virtually coincides with curves *1* and *2*.

A maximum pulse amplitude observed in the 100-Hz regime was ~145 kV, which is close to half of the charging voltage amplitude in the energy accumulator, where the energy stored prior to discharge was about 0.5 J. The peak power level of the output pulses was ~300 MW. As the pulse repetition frequency increased to 2000 Hz, the accumulated energy decreased to 0.3 J, and then average output power on a 50-Ω output was 0.3 kW. Thus, the data presented in Fig. 2 (curve *3*) show that, in the range of switched energies below 1 J, the rate of the electric strength recovery in the hydrogen-filled discharge gap is quite sufficient from the standpoint of generating pulses at a repetition rate of 2000 Hz with virtually no loss in the pulse amplitude.

As the pulse repetition frequency was increased, and the charging voltage in the pulse-forming line decreased by 20–21% at a constant charge time of ~5 ns, the leading front edge of the pulse formed with the hydrogen-filled discharge gap remained virtually unchanged. On the other hand, the time of delay in the cutting discharge gap breakdown gradually increased (at a fixed gap): in the 100–1000 Hz frequency interval, the trailing front width increased from 100 to 200 ps. This decrease was observed when the electric field strength in the gap decreased by 13%. At the same time, the pulse width determined by the cutting discharge gap operation remained stable, with a scatter in the pulse width at half height not exceeding 100 ps.

As a drop in the breakdown voltage changed further (from 13 to 23%), the instant of the cutting discharge gap operation lost stability. In the time pattern of the stroboscopic oscillograph, this instability in the pulse width was manifested by the appearance of a chaotic sequence of peaks on the trailing front background (Fig. 3a, curve *3*). Apparently, these data by no means characterize the rate of the electric strength recovery in the gas medium of the cutting discharge gap. For any value of the pulse repetition frequency in the entire 100–2000 Hz range studied, the discharge gap could be adjusted (decreased) so as to provide for the output pulse width of approximately the same shape as that depicted in Fig. 3a (curve *1*), but at a somewhat reduced pulse amplitude.

Figure 3b shows the analogous oscillograms recorded for the discharge gaps filled with nitrogen. An analysis of these curves showed a considerable decrease in the output pulse amplitude (i.e., in the sharpening discharge breakdown voltage) with increasing modulator pulse repetition frequency. Here, the absolute amplitude drop reached 32–33% (Fig. 2, curve *4*). In comparison with the charging pulse amplitude actually provided by the nanosecond driver (Fig. 2, curves *1* and *2*), the decrease in amplitude reached 15%. Even at a pulse repetition of 100 Hz, the pulse duration uncertainty measured at half height reached 200–300 ps.

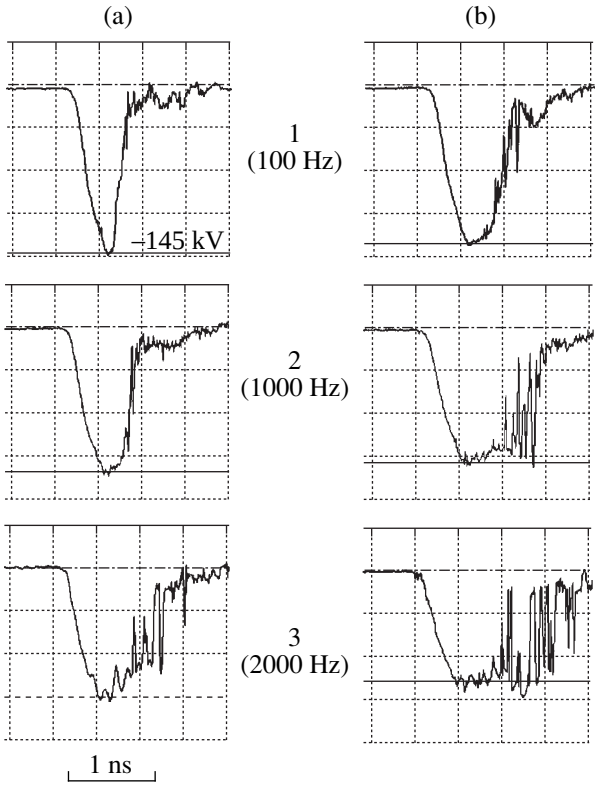

Fig. 3. Oscillograms of the subnanosecond modulator output pulses obtained at various pulse repetition rates for the discharge gaps filled with (a) hydrogen and (b) nitrogen.

Conclusion. Thus, preliminary results of testing of a new subnanosecond pulse modulator showed that integration of a charging device based on a high-voltage nanosecond pulse driver with solid-state commutators and pulse shaper with ultrahigh- pressure hydrogen-filled discharge gaps offers a promising way to solving the task. The hybrid device ensures the obtaining of stable pulses with an amplitude of ~150 kV and above at a pulse width of less than ~500 ps and a repetition rate exceeding 1000 Hz. In the experiments reported above, the number of pulses in a train obtained at a repetition rate of 2 kHz reached 10^4. This number is not limited by any physical factor.

REFERENCES

1. L. Yu. Astanin and A. A. Kostylev, *Principles of Ultra-Broadband Radio-Sounding Measurements* (Radio i Svyaz', Moscow, 1989).
2. V. G. Shpak *et al.*, in *Proceedings of the Xth IEEE International Pulsed Power Conference, Albuquerque, 1995*, p. 666.
3. F. J. Agee *et al.*, Proc. SPIE **2557**, 98 (1995).
4. N. S. Ginzburg *et al.*, Phys. Rev. E **60**, 3297 (1999).

5. V. M. Tuchkevich and I. V. Grekhov, *New Principles of High-Power Switching with Semiconductor Devices* (Nauka, Leningrad, 1988).
6. I. V. Grekhov, Izv. Akad. Nauk, Énerg., No. 1, 53 (2000).
7. B. M. Koval'chuk *et al.*, Prib. Tekh. Éksp., No. 6, 73 (1976).
8. G. A. Mesyats *et al.*, Proc. SPIE **2154**, 262 (1994).
9. V. G. Shpak *et al.*, in *Proceedings of the XIIth IEEE International Pulsed Power Conference, Monterey, 1999*, Vol. 2, p. 692.
10. M. G. Grothaus *et al.*, in *Proceedings of the IXth IEEE International Pulsed Power Conference, Albuquerque, 1993*, Vol. 1, p. 475.
11. A. S. El'chaninov *et al.*, Prib. Tekh. Éksp., No. 4, 162 (1979).
12. N. M. Bykov *et al.*, Prib. Tekh. Éksp., No. 6, 96 (1988).
13. V. G. Shpak *et al.*, in *Proceedings of the Xth IEEE International Pulsed Power Conference, Albuquerque, 1995*, Vol. 2, p. 544.
14. S. K. Lybutin *et al.*, in *Proceedings of the XIIth IEEE International Pulsed Power Conference, Monterey, 1999*, Vol. 2, p. 1226.
15. S. N. Rukin, Prib. Tekh. Éksp., Nos. 4, 5 (1999).

Translated by P. Pozdeev

Technical Physics Letters, Vol. 27, No. 1, 2001, pp. 41–44. Translated from Pis'ma v Zhurnal Tekhnicheskoĭ Fiziki, Vol. 27, No. 2, 2001, pp. 1–8.

Real Structure of a Microchannel Silicon Studied by X-ray Diffraction

E. V. Astrova, V. V. Ratnikov, A. D. Remenyuk, A. G. Tkachenko, and I. L. Shul'pina

Ioffe Physicotechnical Institute, Russian Academy of Sciences, St. Petersburg, 194021 Russia

Received August 9, 2000

Abstract—The crystal lattice structure of a microchannel silicon and variation of this structure in the course of thermal oxidation were studied by X-ray diffraction and topography techniques. © *2001 MAIK "Nauka/Interperiodica".*

Most devices employing microchannel silicon (MCS) are fabricated by the technologies involving thermal oxidation [1–3]. The purpose of this work was to study the degree of MCS matrix crystal lattice perfection and the effect of thermal oxidation processes on this crystal structure.

The process used to obtain deep cylindrical channels in a silicon matrix was described previously [4]. This study was performed on a silicon plate of the 9H-25 type with through pores, which was prepared using a honeycomb pattern template (Fig. 1). The distance between the neighboring initial etch pits in this template was 6 μm, and the etched channel diameter was 3 μm. MCS oxidation was performed by exposure for 100 min at $T = 1200$°C in water vapor, after which the oxide was etched off in hydrofluoric acid (HF). The samples were subject to multiply repeated oxidation–etching cycles, during which the channel diameter increased to ~7 μm.

The results of this treatment are illustrated in Fig. 1 showing the scanning electron microscopy (SEM) images of a sample obtained upon accomplishing seven oxidation–etching cycles. As seen in the front face image, the channel structure is not quite perfect: some extra narrow pores are observed that have appeared during etching besides the main channels determined by the initial etch pits. The additional narrow pores penetrate down to a depth of <10 μm. At the same time, the view from the rear face indicates that not all the main channels initiated at the front face have penetrated through the plate: some of these ceased to propagate and stopped at intermediate depths.

The diffraction properties of the MCS structure were evaluated by determining halfwidths of the symmetric 004 Bragg and 220 Laue reflection profiles measured with a tricrystal diffractometer (TCD). The Bragg measurements provided integral information about the crystallographic planes parallel to the sample surface, while measurements in the Laue geometry characterized the planes perpendicular to the surface. Contributions to the crystal lattice disorder due to the microscopic misorientations (shear component ε_{ij} of the microdistortion tensor) and microdeformations (diagonal components ε_{ii} of the tensor) were separated by

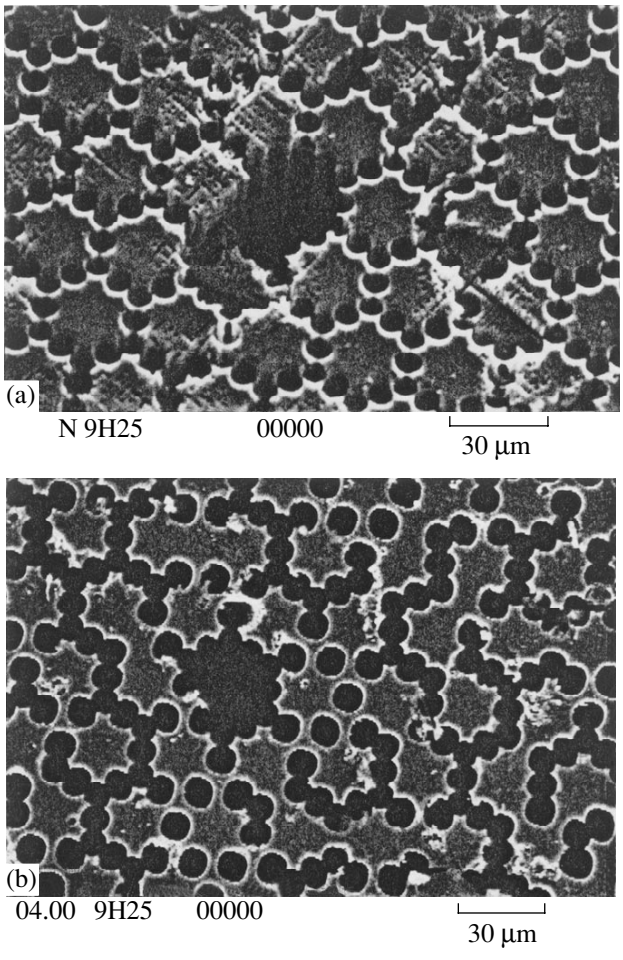

Fig. 1. SEM image of an MCS sample after seven oxidation–etching cycles: (a) front face of the sample; (b) rear face of the sample; (c) a silicon column that fell out of the sample upon etch-off of the oxide walls penetrating through the silicon plate.

1063-7850/01/2701-0041$21.00 © 2001 MAIK "Nauka/Interperiodica"

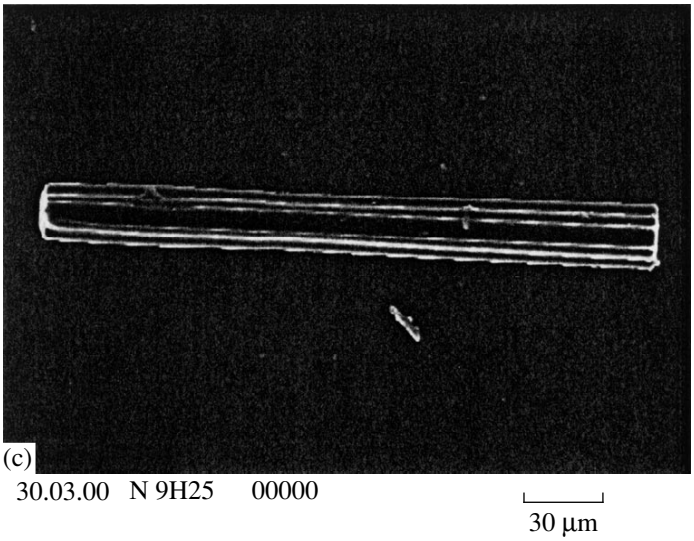

Fig. 1. (Contd.)

measurements in the θ and (θ – 2θ) scanning modes. We have also measured the halfwidth of the asymmetric 224 Bragg reflection at a glancing incidence angle with the aid of a bicrystal diffractometer (BCD).

All the X-ray diffraction measurements were performed using nondispersive (*n*, *–n*, *n*) and (*n*, *–n*, *n*) schemes (for BCD and TCD, respectively) [5]. The measured values of the reflection halfwidth ω (full width at half maximum, FWHM) were corrected for the sample bending. The MCS sample curvature radius changed magnitude and even sign after every oxidation–etching cycle (see table).

The X-ray topograms were measured from both front and rear faces of a sample scanned in the X-ray beam using the backscattering technique in the single- and bicrystal modes [5]. The measurements were performed with CuK_α radiation for the 422 asymmetric reflection.

The results of the X-ray diffraction measurements for the initial silicon wafer used for the MCS sample preparation showed high crystal lattice perfection and homogeneity over the sample area. The BCD and θ-TCD ω (FWHM) values presented in the table are close to the values calculated using the dynamic X-ray scattering theory [5]. Measurements of the unoxidized MCS samples upon electrochemical etching showed an increase up to 50% in the ω values for both BCD (asymmetric 224 reflection) and θ-TCD profiles. As can be seen, the anodic etching did not lead to any significant disturbances in the crystalline matrix.

After the channel formation, the surface area of the sample increased approximately 40 times. This led to broadening of the reflection profiles as a result of increased surface stresses in the MCS crystal lattice. Another factor responsible for the broadening of the Bragg θ-profiles in the initial MCS samples may be a change (decrease) in the X-ray coherence length. The Bragg $\omega_{\theta-2\theta}$ values for the unoxidized MCS and the initial silicon wafer are the same, while the Laue $\omega_{\theta-2\theta}$ values for MCS are two times those for the initial wafer.

X-ray diffraction characteristics of MCS samples

Sample	Oxide	*R*, m	ω, arcsec			ω, arcsec	
			Bragg geometry			Laue geometry	
			BCD ω (224)	TCD		TCD	
				ω_θ (004)	$\omega_{\theta-2\theta}$ (004)	ω_θ (220)	$\omega_{\theta-2\theta}$ (220)
Initial silicon Si	Initial oxide	∞	8.5	5.0	3.5	6.5	3.5
MCS 9H-25	Initial oxide	∞	13.0	7.5	3.5	8.5	7.2
		5.6	115.0	29.5	6.7	69.0	17.0
	Oxide removed	–20.3	75.0	7.5	3.5	18.0	7.2

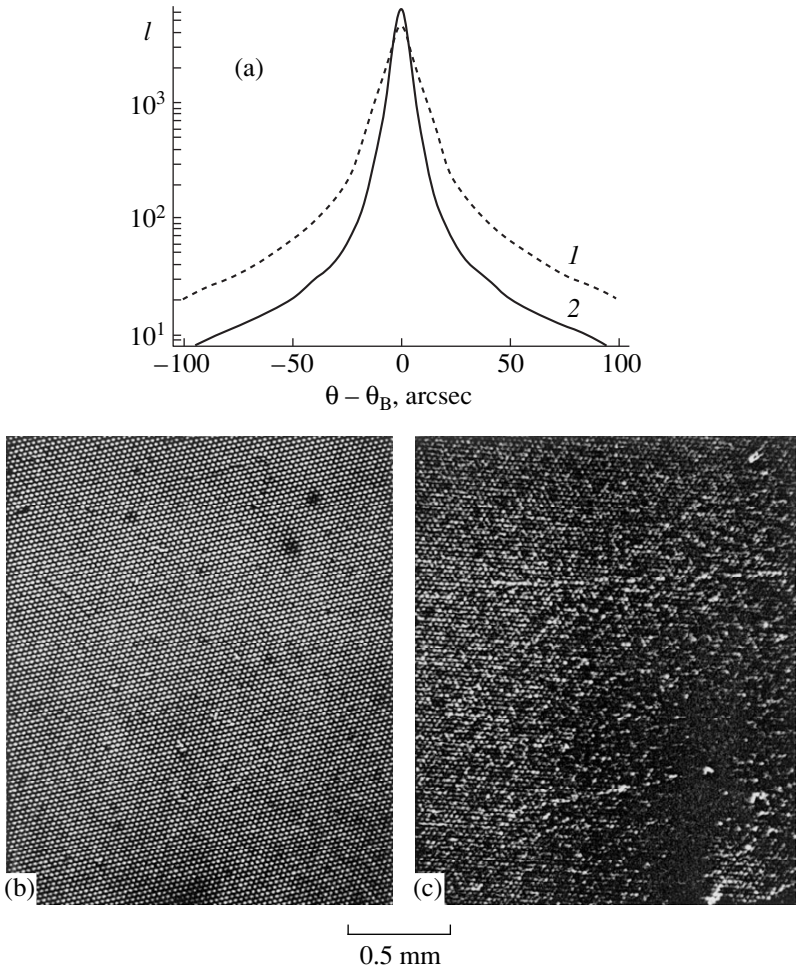

Fig. 2. X-ray diffraction patterns and topograms of MCS samples: (a) rocking curves of (*1*) MCS and (*2*) initial silicon wafers; (b, c) fragments of the X-ray topograms of oxidized MCS measured using the CuK_α radiation in the asymmetric 224 reflection from the (b) front and (c) rear face of the sample.

This indicates that the crystal planes parallel to the sample surface are hardly distorted, in contrast to the perpendicular planes (i.e., those parallel to the channel walls).

The effect of microchannels upon the X-ray diffraction is analogous to the effect of surface roughnesses of the step type and, hence, must lead to incoherent (diffuse) scattering. Indeed, a comparison of the BCD reflection profiles shows a considerable increase in the reflection intensity for MCS in the region of the symmetric 004 Bragg and, especially, of the asymmetric 224 Bragg reflections (Fig. 2a). Thus, the real crystal structure of MCS is markedly different from that of a microporous silicon in which the lattice distortions immediately upon the anodic treatment are so large that they even produce a separate Bragg reflection from a porous layer, shifted noticeably relative to a reflection from the substrate [6–8].

Oxidized MCS samples exhibit a sharp increase in the width of both Bragg and Laue θ and $(\theta - 2\theta)$ profiles. Note that the increase is more pronounced in the Laue than in the Bragg geometry and is greater for the θ than for the $(\theta - 2\theta)$ profiles. This behavior indicates that the level of local misorientations is higher for the planes perpendicular to the surface than for the parallel planes and that the contribution into broadening is greater for the micromisorientations ε_{ij} than for the microdeformations ε_{ii}. A considerable change in ω is also observed for the asymmetric 224 profile. This reflection, the diffraction vector of which forms an angle of 35° with the normal to the sample surface, is sensitive with respect to the lattice distortions characterized by the displacement vectors both parallel and perpendicular to the surface.

The increase in ω observed for the oxidized samples is explained by distortions of the silicon lattice beneath the oxide film. As is known [9], a large difference between the thermal expansion coefficients of Si (3.1×10^{-6} K^{-1}) and SiO_2 (5×10^{-7} K^{-1}) leads, on cooling a sample down to room temperature, to stresses in the crystal lattice, which contract the oxide and expand sil-

icon. These stresses may lead (for the samples heated to $T > 700°C$) to the plastic straining accompanied by the formation of dislocations in silicon. The results of our investigations showed incomplete relaxation of the macrobending after the oxide removal, which is indicative of a partial plastic straining of the samples upon cooling. Thus, the broadening of the reflection profiles is due to large stresses developed in the silicon beneath the oxide film.

After removal of the oxide, the θ and $(\theta - 2\theta)$ curves for the 004 Bragg reflection restore their initial halfwidths. Thus, the diffraction characteristics of the planes parallel to the sample surface are completely recovered in the oxide-free MCS. At the same time, the halfwidths of the asymmetric 224 profile and the θ profile of the symmetric 220 Laue reflection are still markedly greater than the analogous values for unoxidized MCS. Incomplete relaxation of the diffraction characteristics of the planes perpendicular to the surface is related for the most part to the retained high level of the local misorientation. This conclusion follows from the fact that the $(\theta - 2\theta)$-TCD curves measured in the Laue geometry restore their halfwidths observed for the unoxidized MCS (this indicates that microdeformations of the planes perpendicular to the sample surface are released upon oxide removal). This behavior is probably related to the formation of dislocations.

The X-ray topography data confirm the conclusions concerning changes in the real structure of MCS, which were derived from the results of the X-ray diffraction measurements. Figures 2b and 2c show the fragments of the X-ray topograms measured for both faces of the same MCS sample upon oxidation. Figure 2b showing the undistorted regular network of the channels indicates that there are virtually no structural defects on the front face of the sample. At the rear face (Fig. 2c), the channel network image is significantly distorted by dislocations. The dislocations interact with each other and with the dislocations formed at the neighboring channels, forming a superstructural network of their own. No such a pattern was observed prior to the oxidation of the samples. Fig. 2c shows a fragment of a bicrystal topogram that provides for a better and more detailed resolution as compared to the single-crystal pattern. The reason for the appearance of dislocations on the rear face of the sample is not fully clear. This may be related to a difference in the pore structure on the front and rear faces (cf. Figs. 1a and 1b).

Thus, the X-ray diffraction data showed that the crystal lattice of unoxidized microchannel silicon is almost undisturbed. The presence of channels is manifested by an additional diffuse X-ray scattering. Oxidation leads to a considerable distortion of the crystallographic planes and gives rise to the formation of dislocations. Deformations developed in the microchannel silicon as a result of thermal oxidation exhibit a mixed elastic-plastic character.

Acknowledgments. This work was supported in part by the Russian Foundation for Basic Research (project nos. 98-02-18309, 99-02-17103, 00-02-16760) and by a grant from the Ministry of Science of the Russian Federation (project no. 99-1107).

REFERENCES

1. S. Ottow, V. Lehman, and H. Foll, J. Electrochem. Soc. **143**, 385 (1996).
2. V. Lehman, W. Honlein, H. Reisinger, *et al.*, Thin Solid Films **276**, 138 (1996).
3. E. V. Astrova, I. V. Grekhov, A. V. Nashchekin, *et al.*, Pis'ma Zh. Tekh. Fiz. **25** (23), 72 (1999) [Tech. Phys. Lett. **25**, 958 (1999)].
4. E. V. Astrova, I. L. Shul'pina, A. G. Tkachenko, *et al.*, Pis'ma Zh. Tekh. Fiz. **26** (24), 31 (2000) [Tech. Phys. Lett. **26**, 1087 (2000)].
5. D. K. Bowen and B. K. Tanner, *High-Resolution X-ray Diffractometry and Topography* (Taylor and Francis, London, 1998).
6. K. Barla, R. Herino, G. Bomchil, *et al.*, J. Cryst. Growth **68**, 727 (1984).
7. E. V. Astrova, V. V. Ratnikov, R. V. Vitman, *et al.*, Fiz. Tekh. Poluprovodn. (St. Petersburg) **31**, 1261 (1997) [Semiconductors **31**, 1084 (1997)].
8. D. Papadimitriou, J. Bitsakis, J. M. López-Villegas, *et al.*, Thin Solid Films **349**, 293 (1999).
9. R. J. Jaccodine and W. A. Schlegel, J. Appl. Phys. **37** (6), 2429 (1966).

Translated by P. Pozdeev

Technical Physics Letters, Vol. 27, No. 1, 2001, pp. 45–48. Translated from Pis'ma v Zhurnal Tekhnicheskoĭ Fiziki, Vol. 27, No. 2, 2001, pp. 9–16.

The Ion Charge–Current Strength Relationship in Stationary and Pulsed Vacuum Discharges

I. A. Krinberg

Irkutsk State University, Irkutsk, 664003 Russia

Received August 8, 2000

Abstract—It is shown that the electron temperature in the region where the vacuum-discharge plasma is in equilibrium with the intrinsic magnetic field is proportional to the discharge current I and inversely proportional to the coefficient of erosion of the cathode material. For $I \geq 300$ A, this region features additional electron-impact ionization of ions coming from the near-cathode layer. As a result, the average ion charge Z increases with the current strength, the $Z(I)$ dependence being more pronounced at a lower discharge pulse duration. © *2001 MAIK "Nauka/Interperiodica".*

Introduction. As is known [1, 2], the ion composition of the vacuum arc discharge plasma is independent of the discharge current strength I in the range from 50 to 500 A, being characterized by an average ion charge $Z_0 = 1$–3 depending only on the cathode material. The constant ion composition is naturally explained by a specific mechanism of the vacuum arc plasma formation, involving the electrode material evaporation from small surface areas (1–10 μm in size) called the cathode microspots (or emission centers and fragments) [3]. The plasma formed by this mechanism is characterized by an electron temperature of $T_0 \approx 2$–5 eV and a high electron density $N_0 \approx 10^{20}$–10^{21} cm^{-3} [4–6] that facilitates the attainment of the ionization equilibrium described by the Saha equations. An increase in the discharge current strength I leads only to a proportional growth in the number of cathode microspots and plasma microjets emitted from these spots, while not changing the T_0 and N_0 values and, hence, not affecting the ion charge $Z_0(T_0, N_0)$.

With increasing distance r from the cathode surface, the ion velocity V increases up to the limiting value $V_0 \approx (20Z_0T_0/m)^{1/2} \approx (0.5–2) \times 10^6$ cm/s [7, 8], the electron density drops by several orders in magnitude, and the electron temperature decreases by a factor of several tens [6, 7]. However, the plasma cannot relax so rapidly to a new equilibrium ion charge distribution corresponding to these $T_e(r)$ and $N_e(r)$ values. For this reason, the relative ion composition remains almost unchanged ("frozen") [5], corresponding approximately to the initial T_0 and N_0 values in the near-cathode layer [9].

At a discharge current strength of $I > 500$ A, however, the stationary vacuum arcs exhibit some increase in the average ion charge $Z(I)$ with the ion current I [10], which is especially pronounced in the case of a pulsed vacuum discharge [8, 11]. The main physical mechanism that accounts for the growth in the ion charge with the current is apparently a contraction of the cathode plasma column (formed upon the merging of a manifold of plasma microjets) under the action of its own magnetic field, which leads to the appearance of an additional "hot zone" outside the cathode layer [6, 12–14]. Previously [6, 14], we performed numerical calculations of the electron temperature for some particular cases and qualitatively estimated the degree of the ion charge growth due to the additional ionization in this "hot zone."

In this study, we have obtained a general analytical solution describing the electron temperature as a function of the current strength and other vacuum discharge parameters. We also derived analytical relationships for calculating the ion composition under the nonequilibrium ionization conditions in the "hot zone." Based on these solutions, we have studied in more detail the ion charge as function of the current strength at various discharge pulse durations.

Plasma equilibrium in a magnetic field. The results of numerical model calculations [6, 13, 14] show that a slow increase in the discharge current strength (pulse duration $\tau > \tau_L$, where $\tau_L \approx L/V \approx 0.1$–$1$ μs is a characteristic time for plasma to fill the interelectrode gap with a length L) is accompanied by the uniform magnetic contraction of the plasma column, whereby the magnetic pressure (at a distance $r \geq 1$ mm from the cathode and a current of $I \geq 300$ A) becomes equal to the plasma pressure $P = T_eN_e + T_+N_+$ ($N_+ = N_e/Z$ and T_+ are the ion density and temperature, respectively). The conditions for this equilibrium are as follows:

$$-\nabla P + \mathbf{j} \times \mathbf{B}/c = 0, \quad (1)$$

$$\nabla \times \mathbf{B} = 4\pi\mathbf{j}/c, \quad (2)$$

where $\mathbf{B}$ is the magnetic induction, $\mathbf{j}$ is the current density, and c is the speed of light.

1063-7850/01/2701-0045$21.00

Let us assume that the plasma column has a cone shape with a slowly varying semi-apex angle $\alpha(r)$ and a surface obeying the condition $N_e = 0$. Using the spherical coordinates (r, θ, φ) and taking into account the axial symmetry of the plasma column, we obtain the following relationship from Eqs. (1) and (2):

$$-\frac{dP}{d\theta} + \frac{1}{8\pi\sin\theta}\frac{dB^2}{d\theta} = 0. \quad (3)$$

Multiplying (3) by $\sin\theta$ and integrating it with respect to θ from 0 to α, we obtain the pressure $\bar{P} = B_\alpha^2/8\pi$ averaged over a plasma column cross-section representing an element of the spherical surface $S(r) = 2\pi r^2(1 - \cos\alpha)$. Using Eq. (2), we may also determine the magnetic field strength $B_\alpha = 2I/(cR)$ on the side surface of the column (with a radius of $R = r\sin\alpha$). Taking into account the inequality $T_e \gg T_+/Z$ and neglecting variations in the electron density and temperature in the plasma column cross section, we obtain an expression:

$$\bar{P} = N_e T_e = \frac{I^2}{2\pi R^2 c^2}, \quad (4)$$

which coincides with the Bennett equilibrium criterion for a cylindrical plasma column [15].

Since the total discharge current is determined by the relationship $I = jS = eN_eU_eS$ (where U_e and e are the current velocity and electron charge), Eq. (4) yields the formula $T_e = eU_eSI/(2c^2\pi R^2)$. Using a dimensionless erosion coefficient $\eta = ZeG/mI = I_+/I = V/U_e$ (where $G = mN_+VS = mI_+/Ze$ is the erosion rate and I_+ is the ion current), we may replace the current velocity of electrons by the velocity of ions. Then, taking into account that we may assume with a sufficient accuracy (for $\alpha < \pi/4$) that $\pi R^2/S = (1 + \cos\alpha)/2 \approx 1$, we arrive at an expression

$$T_e = \left(\frac{e}{2c^2}\right)\frac{V}{\eta}I, \quad (5)$$

where $e/2c^2 = 5 \times 10^{-10}$ (eV s)/(A cm). As is seen from formula (5), the electron temperature in the "hot zone" is proportional to the discharge current ($T_e = kI$) and independent of the column cross section. Since, according to the calculations [6], the ion velocity in this region of the cathode column is almost unchanged, we may assume that $V \approx V_0$. Then, using typical values of the erosion coefficient $\eta = 0.06$–0.11 [16] and the ion velocity $V_0 = (0.5$–$2) \times 10^6$ cm/s [8], we may estimate the proportionality factor in the above relationship: $k \approx 0.005$–0.01 eV/A.

Now we can readily obtain an estimate for the "hot zone" temperature T_e, which must exceed that in the cathode layer (where $T_e = T_0 \approx 2$–5 eV) for a current of 300–500 A [5]. Indeed, it is this very interval of currents where a significant increase in the ion charge was observed [8, 10, 11, 17].

Nonequilibrium Ionization. According to the results of numerical model calculations [6, 14], the electron temperature and density, as well as the ion velocity, vary rather weakly along the plasma column. Therefore, in calculating the ion composition in the "hot zone" we may assume that $T_e = \text{const}$, $N_e = \text{const}$, and $V = V_0 = \text{const}$. Under these assumptions, the ion number balance equation is as follows [18]:

$$\frac{dN_n}{dt} = V_0\frac{dN_n}{dr} = k_nN_{n-1}N_e - k_{n+1}N_nN_e - r_nN_nN_e^2 + r_{n+1}N_{n+1}N_e^2, \quad (6)$$

where N_n is the density of ions of the nth type (with the ne charge). The approximate values of the electron-impact ionization coefficients $k_n(T_e)$ were taken from [14] and the coefficient of triple recombination r_n can be evaluated from the detailed balance equation $k_n/r_n = AT_e^{3/2}\exp(-E_n/T_e)$ [18], where $A \approx 6 \times 10^{21}$ cm^{-3} eV$^{-3/2}$. Assuming $N_n \cong N_{n-1}$, the condition of ionization dominating over recombination can be written in the form of inequality: $k_n/r_nN_e \gg 1$. This inequality holds for $N_e \le 10^{17}$ cm^{-3}, which is valid in the "hot zone" at a distance $r \ge 1$ mm from the cathode. Neglecting the recombination rate, Eq. (6) can be transformed to

$$\frac{df_n}{dr} = \frac{f_{n-1}}{\lambda_n} - \frac{f_n}{\lambda_{n+1}}, \quad (7)$$

where $\lambda_n = V_0/k_nN_e$, $f_n = N_n/N_+$ are the relative densities of ions, and $N_+ = \sum N_n$ is the total on density. The initial values of ion fractions f_n^0 (for $r = r_0$) can be determined from the results of measurements at small currents ($I = 50$–200 A) [1, 5], where the additional ionization at $r \ge 1$ mm is absent.

Taking into account the inequality $\lambda_{n+1} \gg \lambda_n$, we obtain a simple solution to Eq. (7):

$$f_n(r) = C_n\exp\left(-\frac{r - r_0}{\lambda_{n+1}}\right) - C_{n-1}\exp\left(-\frac{r - r_0}{\lambda_n}\right), \quad (8)$$

where $C_n = \sum_{k=1}^{n} f_k^0$. The average ion charge can be determined using the formula $Z = \sum_{n=1} nf_n$.

Results of numerical calculations. We have calculated the ion composition and average charge using solution (8) for the cathodes of W, Al, and Cu for $r - r_0 = 1$ cm, which is a typical length of the interelectrode gap. The f_k^0, Z_0, and T_0 values were taken from [1, 5], the erosion coefficients $\eta = 0.1$ (Al) and 0.07 (W) were taken from [19], and the $G/I = 2 \times 10^{-5}$ g/C ($\eta = 0.06$) and $G/I = 4 \times 10^{-5}$ g/C ($\eta = 0.12$) for the pulsed and

stationary vacuum arc with Cu cathode were taken from [16].

In order to take into account the function $\lambda_n(T_e, N_e)$ which is significant in determining the nonequilibrium ion composition, we have to evaluate the electron temperature and density. The temperature can be evaluated using Eq. (5), while the electron density can be determined from the current value through the relationship $N_e = \eta I/(eV_0S)$ (for the known column cross section S). The latter can be estimated taken this cross section equal to the total area of cathode spots. Using the corresponding experimental data, we have studied three typical cases. The first was a stationary vacuum arc with an Al cathode, for which the spots were assumed to occupy the whole cathode surface: $S = S_{\text{cath}} = 0.3$ cm^2 (for an experimental setup with a cathode diameter of 0.62 cm [11]). Another case was a microsecond-pulse discharge with a W cathode, for which we assumed $S = S_1 I/I_1$, where S_1 is a single cathode spot area and I_1 is the current passing through this spot (I/I_1 being the number of spots). The third case was a discharge with the time-dependent cross section at a Cu cathode, the time variation of the total spot area being modeled by the relationship

$$S(t) = \frac{S_1 T(t)}{I_1}\left(1 + \frac{t}{\tau_S}\right), \qquad (9)$$

where t is the discharge operation time, $t_S \cong S_1/D$ is a characteristic time of the spot spreading over the cathode surface, and D is the diffusion coefficient for the random spot motion. The resulting experimental estimates of the spot parameters varied within a rather broad range: $S_1 = 10^{-4}$–10^{-3} cm^2; $I_1 = 20$–150 A; $D = 5$–20 cm^2/s [20–23]. Taking these values into account, we accepted $S_1/I_1 = 3 \times 10^{-6}$ cm^2/A for tungsten and $S_1/I_1 = 10^{-6}$ cm^2/A for copper ($\tau_S = 1$ μs).

As seen from Fig. 1, the additional nonequilibrium ionization of ions in the near-cathode plasma leads to a markedly stronger dependence of the average ion charge on the current $Z(I)$ in short-pulse discharges than in stationary arcs, because the ionizing electron density [for the same current strength determining the electron temperature according to formula (5)] increases with decreasing cathode spot area (i.e., with decreasing plasma column cross section). This tendency is also illustrated in Fig. 2 showing that the dependence of the average ion charge on the current decreases with the duration of the vacuum arc discharge operation. It must also be noted that the on charge is markedly affected by the rate of the cathode material erosion: the values calculated for $t = 2000$ μs coincide with the experimental data only when the erosion coefficient is doubled, which is observed upon going from pulsed to stationary arc discharge [16].

Conclusions. The results of the investigations described above lead to the following conclusions:

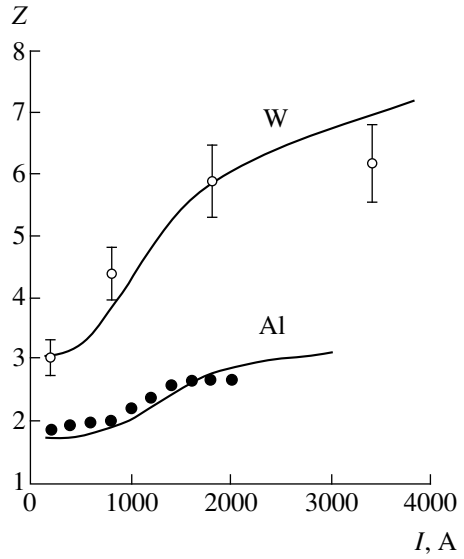

Fig. 1. The plots of average ion charge vs. current strength for a stationary (Al cathode) and pulsed (W cathode) vacuum arc discharge: solid curves, numerical calculation; open circles, experimental data from [11]; back circles, experimental data from [10].

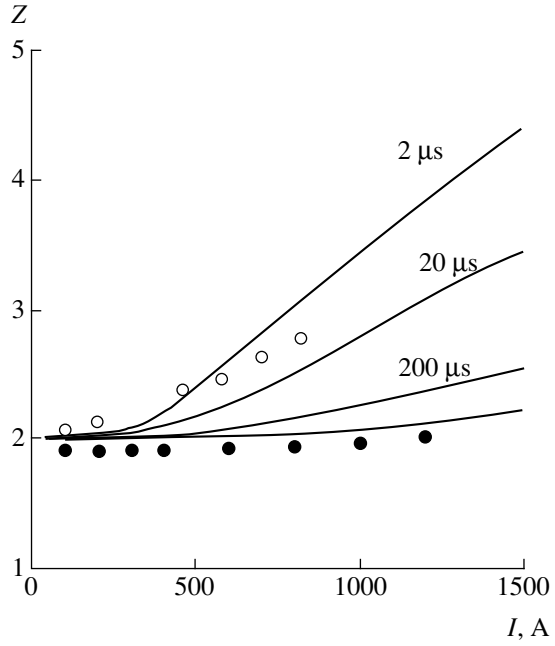

Fig. 2. The plots of average ion charge versus current strength for a Cu cathode for various discharge pulse durations: thick solid curve, calculation for $\eta = 0.06$; thin solid curve, calculation for $\eta = 0.12$; open circles, experimental data for $t = 1$–6 μs [17]; back circles, experimental data for $t = 200$ μs [10].

1. In a plasma column region sufficiently far from the cathode, where the vacuum-discharge plasma is in equilibrium with the intrinsic magnetic field, the electron temperature is proportional to the discharge cur-

rent strength I and inversely proportional to the coefficient of erosion of the cathode material.

2. For the discharge currents $I \geq 300$ A, the electron temperature in this region exceeds the value in the near-cathode layer. This leads to additional electron-impact ionization of ions supplied from the near-cathode layer. As a result, the average ion charge increases with the discharge current.

3. Dependence of the average ion charge on the discharge current becomes less pronounced with increasing discharge pulse duration. This is explained by increasing cathode erosion, which leads to a decrease in the electron temperature, an increase in the plasma column cross section, and a drop in the electron density (for randomly distributed cathode spots). Close coincidence of the theoretical and experimental $Z(I)$ curves indicates that the intrinsic magnetic field strongly influences the vacuum arc discharge parameters.

Acknowledgments. This work was supported by the Russian Foundation for Basic Research, project nos. 00-02-16792 and 99-02-18163.

REFERENCES

1. J. E. Galvin, I. G. Brown, and R. A. MacGill, Rev. Sci. Instrum. **61** (1), 583 (1990).
2. A. G. Nikolaev, E. M. Oks, and G. Yu. Yushkov, Zh. Tekh. Fiz. **68** (5), 39 (1998) [Tech. Phys. **43**, 514 (1998)].
3. G. A. Mesyats, Usp. Fiz. Nauk **165** (6), 601 (1995) [Phys. Usp. **38**, 567 (1995)].
4. A. Anders, S. Anders, B. Juttner, and H. Luck, IEEE Trans. Plasma Sci. **24** (1), 69 (1996).
5. A. Anders, Phys. Rev. E **55** (1), 969 (1997).
6. I. A. Krinberg and E. A. Zverev, Fiz. Plazmy **25** (1), 88 (1999) [Plasma Phys. Rep. **25**, 82 (1999)].
7. I. A. Krinberg, M. P. Lukovnikova, and V. L. Papernyĭ, Zh. Éksp. Teor. Fiz. **97** (3), 806 (1990) [Sov. Phys. JETP **70**, 451 (1990)].
8. A. S. Bugaev, V. I. Gushenets, A. G. Nikolaev, *et al.*, IEEE Trans. Plasma Sci. **27** (4), 882 (1999).
9. I. A. Krinberg and M. P. Lukovnikova, J. Phys. D **28** (4), 711 (1995).
10. E. M. Oks, A. Anders, G. Brown, *et al.*, IEEE Trans. Plasma Sci. **24** (3), 1174 (1996).
11. A. Anders, I. G. Brown, M. R. Dickinson, and R. A. MacGill, Rev. Sci. Instrum. **67** (3), 1202 (1996).
12. I. A. Krinberg and E. A. Zverev, Pis'ma Zh. Tekh. Fiz. **23** (1), 47 (1997) [Tech. Phys. Lett. **23**, 435 (1997)].
13. E. A. Zverev and I. A. Krinberg, Pis'ma Zh. Tekh. Fiz. **24** (18), 50 (1998) [Tech. Phys. Lett. **24**, 728 (1998)].
14. E. A. Zverev and I. A. Krinberg, Pis'ma Zh. Tekh. Fiz. **26** (7), 43 (2000) [Tech. Phys. Lett. **26**, 288 (2000)].
15. L. D. Landau and E. M. Lifshitz, *Course of Theoretical Physics*, Vol. 8: *Electrodynamics of Continuous Media* (Nauka, Moscow, 1982; Pergamon, New York, 1984).
16. G. A. Mesyats and D. I. Proskurovskiĭ, *Pulsed Electric Discharge in Vacuum* (Nauka, Novosibirsk, 1984).
17. E. N. Abdullin and G. P. Bazhenov, in *Proceedings of the 18th International Symposium on Discharges and Electrical Insulation in Vacuum, Netherlands, Eindhoven, 1998,* Vol. 1, p. 207.
18. L. M. Biberman, V. S. Vorob'ev, and I. T. Yakubov, *Kinetics of Nonequilibrium Low-Temperature Plasmas* (Nauka, Moscow, 1982; Consultants Bureau, New York, 1987).
19. J. E. Daalder, Physica B+C (Amsterdam) **104** (1), 91 (1981).
20. P. Siemroth, T. Schulke, and T. Witke, IEEE Trans. Plasma Sci. **23** (6), 919 (1995).
21. I. Beilis, B. E. Djakov, B. Juttner, and H. Pursch, J. Phys. D **30** (1), 119 (1997).
22. A. Anders, S. Anders, B. Juttner, and I. G. Brown, IEEE Trans. Plasma Sci. **21** (3), 305 (1993).
23. B. Juttner, IEEE Trans. Plasma Sci. **27** (4), 836 (1999).

Translated by P. Pozdeev

Technical Physics Letters, Vol. 27, No. 1, 2001, pp. 49–51. Translated from Pis'ma v Zhurnal Tekhnicheskoĭ Fiziki, Vol. 27, No. 2, 2001, pp. 17–23.

Laser Deposition and Study of $CuInS_{2x}Se_{2(1-x)}$ Crystals and Films

E. P. Zaretskaya, I. A. Victorov, V. F. Gremenok, and A. V. Mudryĭ

Institute of Solid State and Semiconductor Physics, National Academy of Sciences of Belarus, Minsk, 220072 Belarus

e-mail: gremenok@ifftp.bas-net.by

Received March 29, 2000

Abstract—Single-phase films of $CuInS_{2x}Se_{2(1-x)}$ solid solutions with a chalcopyrite structure were deposited by laser evaporation of $CuInS_{2x}Se_{2(1-x)}$ crystal targets ($0 \le x \le 1$). The structural and optical characteristics of the films depend on the chalcogen concentrations. © *2001 MAIK "Nauka/Interperiodica".*

$CuInS_2$ is a semiconductor compound with a bandgap width of E_g = 1.5 eV and an optical absorption coefficient $\alpha > 10^5$ cm^{-1}, which is a promising material for high-efficiency thin-film solar cells. The solar to electric energy conversion efficiency of the photovoltaic cells based on polycrystalline $CuInS_2$ films reaches 15% [1–4]. Using solid solutions of the $CuInS_{2x}Se_{2(1-x)}$ system, it is possible to obtain materials with controlled properties and the bandgap width adjusted so as to be close to the solar emission peak position.

As is known, the structural and electric characteristics of $CuInSe_2$ are determined by the deviation of the crystal composition from stoichiometry [5–7]. It can be suggested that the dependence of the properties of crystals and films of solid solutions of the $CuInS_{2x}Se_{2(1-x)}$ system must be similar to that established for $CuInSe_2$, but the available experimental data are highly contradictory. The $CuInS_2$ films were prepared by pyrolysis [8] and by sulfiding Cu–In layers in an H_2S atmosphere [9], while the $CuInS_{2x}Se_{2(1-x)}$ layers were deposited either by evaporating components from various sources or by diffusing Cu and S into In_2Se_3 films [10]. A common disadvantage of all these methods is the inhomogeneity of deposits and their tendency to phase separation, which predetermines the ambiguity of data on the physical properties and structural characteristics of $CuInS_2$ and $CuInS_{2x}Se_{2(1-x)}$ films [5–11].

The purpose of our experiments was to study the effect of the S–Se anion substitution on the properties of bulk crystals and films of $CuInS_{2x}Se_{2(1-x)}$ solid solutions obtained by the pulsed laser deposition technique. A characteristic feature of this method is the congruent character of the mass transfer of evaporated substances from target to deposit, which provides for a reproducible composition of this multicomponent semiconductor containing a highly volatile component [12].

The initial target materials were $CuInS_{2x}Se_{2(1-x)}$ crystals with Cu/In ≈ 1, synthesized by directional crystallization from the melt of elementary components (V3 grade copper, 000 grade indium, special-purity grade sulfur and selenium) taken in a stoichiometric ratio. In order to obtain spatially homogeneous crystals, the synthesized ingots were homogenized by annealing for 720 h at 1073 K.

The films were deposited in a vacuum of $(2–4) \times 10^{-5}$ Torr with the aid of a Nd laser operated in a free lasing mode (λ = 1.06 μm; $\tau = 10^{-3}$ s; E = 150–180 J). The deposits were obtained as described in [12] at an average rate of $(3–6) \times 10^5$ Å/s on Cornig glass 7059 substrates heated to T = 573–723 K. The deposited layer thickness was 0.3–1.0 μm.

The structures of the $CuInS_{2x}Se_{2(1-x)}$ crystals and films were studied by X-ray diffraction using Ni-filtered CuK_α radiation (λ_{av} = 1.54178 Å). The measurements were conducted in the range of diffraction angles 2θ = 15–100° and interpreted (phase identification) using the JCPDS Tables.

It was established that $CuInS_{2x}Se_{2(1-x)}$ polycrystals possess a homogeneous single-phase structure. The X-ray diffractograms obtained from annealed powders exhibit a single series of diffraction lines characteristic of the chalcopyrite structure (112, 200/204, 312/116, 400/008, 316/332, etc.) with well-resolved doublets (Fig. 1a). The angular positions of the diffraction reflections exhibit an x-dependent shift, and the 112 reflection has a symmetric profile, which is evidence for the formation of a homogeneous solid solution. The presence of the superstructure reflections (101, 103, 211, 211/105) is indicative of the cation sublattice ordering and the crystallization according to the I42d group [1]. The lattice constants a and c vary with the composition as described by the linear relationships

$$a = 5.778 - 0.272x \text{ (Å)},$$

$$c = 11.596 - 0.486x \text{ (Å)}.$$

It was found that the laser-deposited $CuInS_{2x}Se_{2(1-x)}$ films are also single-phase in the entire range of com-

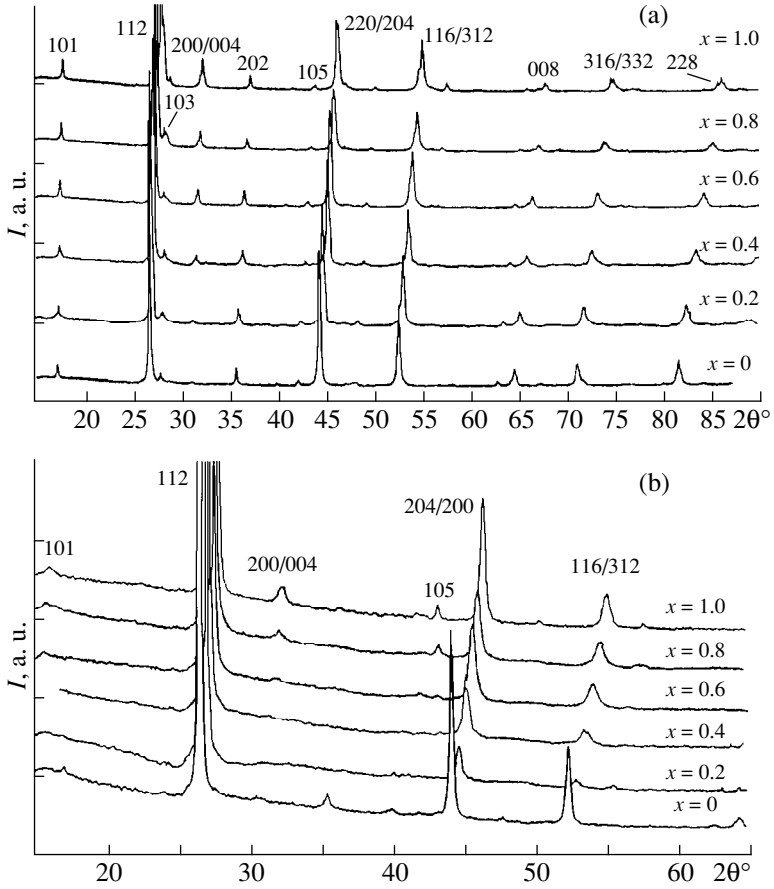

Fig. 1. X-ray diffractograms of (a) powdered $CuInS_{2x}Se_{2(1-x)}$ crystals and (b) $CuInS_{2x}Se_{2(1-x)}$ laser-deposited films with various chalcogen concentrations.

positions ($0 \le x \le 1$) and possess the crystal lattice parameters that are close to the analogous values of the initial materials. The layers deposited at $T > 673$ K exhibited a preferred orientation in the [112] direction, with their structural characteristics depending on the ratio of chalcogen concentrations. The $CuInS_{2x}Se_{2(1-x)}$ films with a high content of selenium ($x \le 0.3$) possessed an ordered chalcopyrite structure and were highly oriented in the [112] direction. The degree of orientation, determined from the I_{112}/I_{220} ratio, exceeded 10, while the halfwidth of the 112 reflection was $FWHM_{112} = 0.15°$.

As the sulfur content increased ($x > 0.3$), the crystal quality was deteriorated. This was evidenced by a decrease in the I_{112}/I_{220} ratio and by an increase in the 112 peak width ($FWHM_{112} = 0.33°$ for $x = 0.8$), which was indicative of a reduced crystal grain size in the films. The X-ray diffractograms of these films still contained a series of lines typical of the chalcopyrite structure, but the superstructure peaks 101, 103, 211 were no longer observed, which is characteristic of a disordered cation sublattice (Fig. 1b).

The optical properties of the films were studied in the 0.4–2.8 μm wavelength range on a Carry-17 UV-VIS-NIR spectrophotometer. Figure 2a shows typical spectral dependences of the room-temperature (T = 300 K) optical density $D(\lambda)$ for the $CuInS_{2x}Se_{2(1-x)}$ films with various compositions. The main feature of these spectra is a high optical density level in the transmission region and a shift of the $D(\lambda)$ curves toward shorter wavelengths with increasing sulfur content.

Figure 2b shows the plots of $(\alpha h\nu)^2$ versus photon energy for several compositions, which exhibit large linear portions obeying the relationship $\alpha h\nu \approx A(h\nu - E_g)^{1/2}$ typical of direct interband optical transitions. In the region of small α, the spectral characteristics deviate from the quadratic relationship. The presence of the so-called "tails" may be due to additional energy states at the forbidden band edges. These states may be related to the structural defects of various types (grain boundaries, etc.) and to the deviation from stoichiometry.

The bandgap width E_g determined for the $CuInS_{2x}Se_{2(1-x)}$ films by extrapolating the $(\alpha h\nu)^2$ versus $h\nu$ plot varies linearly with the composition: from

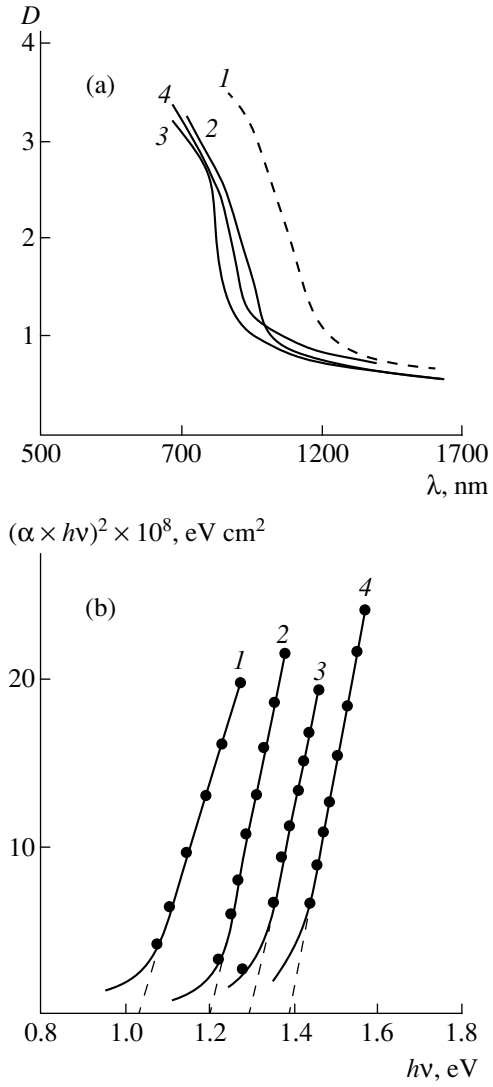

Fig. 2. Optical properties of laser-deposited $CuInS_{2x}Se_{2(1-x)}$ films characterized by (a) the plots of optical density D vs. wavelength λ and (b) the plots of $(\alpha h\nu)^2$ vs. photon energy $h\nu$ for the samples with x = 1 (*1*); 0.8 (*2*); 0.6 (*3*); 0 (*4*).

1.03 at x = 0 to 1.43 eV for x = 1. Understated bandgap widths obtained for the films with high sulfur content, characterized by a disoriented structure and a small grain size (and, accordingly, by a high density of structural defects), are probably explained by the optical transitions between the aforementioned additional energy states. The observed E_g values fall within the interval reported for $CuInS_{2x}Se_{2(1-x)}$ [9].

In concluding, it must be noted that deterioration of the crystal structure (decrease in the grain size and the degree of preferential orientation) in single-phase laser-deposited $CuInS_{2x}Se_{2(1-x)}$ films with increasing S/(S + Se) ratio is indicative of the presence of different growth mechanisms. A similar phenomenon of disordering is a general trend observed in the course of the S–Se anion exchange in $CuInS_{2x}Se_{2(1-x)}$ films. According to [13], this behavior may be related to the chalcopyrite–spinel phase transition.

Acknowledgments. The work was supported by the Belarus Republic Foundation for Basic Research.

REFERENCES

1. T. Walter, M. Ruckh, K. L. Velthaus, and H. W. Shock, in *Proceedings of the 11th E.C. Photovoltaic Solar Energy Conference, 1992* (Harwood Academic, Chur, 1993), p. 124.
2. T. Walter, R. Menner, Ch. Koble, and H. W. Schock, in *Proceedings of the 12th E.C. Photovoltaic Solar Energy Conference, Amsterdam, 1994*, p. 1755.
3. R. Scheer, T. Walter, H. W. Schock, *et al.*, Appl. Phys. Lett. **63** (24), 3294 (1993).
4. Y. Ogawa, A. Jager-Waldau, Y. Kashimoto, and K. Ito, Jpn. J. Appl. Phys. **33**, 1775 (1994).
5. D. Braunger, D. Hariskos, T. Walter, and H. W. Schock, Sol. Energy Mater. Sol. Cells **40**, 97 (1996).
6. R. Noufi, R. Axton, C. Herington, and S. K. Deb, Appl. Phys. Lett. **45**, 668 (1984).
7. J. D. Tuttle, D. Albin, R. J. Matson, and R. Noufi, J. Appl. Phys. **66**, 4408 (1989).
8. R. Díaz, M. Leon, and F. Rueda, Jpn. J. Appl. Phys. **31**, 4408 (1992).
9. M. Ortega-López and A. Morales Asevedo, Thin Solid Films **330**, 96 (1998).
10. S. P. Grindle and C. W. Smith, Appl. Phys. Lett. **35** (1), 24 (1979).
11. T. Walter, O. Ch. Koblle, R. Herberholz, and H. W. Shock, Cryst. Res. Technol. **31**, 431 (1996).
12. E. P. Zaretskaya, V. K. Gremenok, I. A. Victorov, *et al.*, in *Proceedings of the 11th ICTMC Conference, Salford, 1997*, p. 361.
13. T. Walter and H. W. Schock, Jpn. J. Appl. Phys., Suppl. **32**, 116 (1993).

Translated by P. Pozdeev

Technical Physics Letters, Vol. 27, No. 1, 2001, pp. 52–54. Translated from Pis'ma v Zhurnal Tekhnicheskoĭ Fiziki, Vol. 27, No. 2, 2001, pp. 24–29.

Liquid-Crystalline Microlenses in Optical Limitation Systems

M. V. Gryaznova, V. V. Danilov, Yu. A. Kuznetsov, V. V. Ryl'kov, P. A. Shakhverdov, and A. I. Khrebtov

Institute of Laser Physics, St. Petersburg, Russia

e-mail: vdanilov@ilph.spb.ru

Received July 25, 2000

Abstract—Model arrays of nonsymmetric microlenses based on a nematic liquid crystal composition with $\Delta\varepsilon = 10$ were manufactured and their optical characteristics were studied. The efficacy of using these devices in the optical limitation systems is demonstrated for a C_{70} fullerene solution in toluene. © *2001 MAIK "Nauka/Interperiodica".*

The systems of eye protection have to obey rather contradictory conditions, including high transmission in the low-intensity irradiation regime, fast response to the light pulses of a few femtoseconds in duration, and high radiation resistance. Operation of these devices, called optical limiters, is based on the nonlinear response of some media to intensive light action.

According to the standards adopted in some countries [1, 2], the maximum level of radiant energy considered as safe for human vision is $(2–5) \times 10^{-7}$ J/cm^2, depending on the irradiation conditions. However, in most of the physical mechanisms employed in optical limitation devices, the threshold of the limitation effect never decreases below 10^{-1}–10^{-2} J/cm^2 [3]. For this reason, the required radiation intensity level at the output of the optical limiter can be obtained only by using some additional methods. An analysis of the published data indicates that the most effective solutions employ telescope systems, in which a cell with the nonlinear medium is situated near the conjugated telescope focus. However, the use of conventional lens systems in optical limiters has disadvantages such as a cumbersome design and high cost.

In recent years, considerable progress has been achieved in the development of liquid-crystalline (LC) microlenses [4]. These are optical devices with controlled focal distance, which employ the effect of the nematic liquid crystal (NLC) director orientation in an inhomogeneous electric field. An NLC is placed into a cell with two electrodes, one or both having round holes (Fig. 1a). In the first case, the system represents an array of nonsymmetric microlenses (this variant is used in our work), while in the second case, the LC microlenses are symmetric.

The application of a voltage to the electrodes gives rise to an inhomogeneous electric field in the region of holes. The NLC molecules with a positive anisotropy of the dielectric permittivity ($\Delta\varepsilon$) tend to align in the field direction. The reorientation of molecules leads to an inhomogeneous distribution of the refractive index for the extraordinary wave propagating in the NLC. As a result, the cell with a planar NLC orientation features the appearance of a nearly quadratic phaseshift profile [5]. The LC microlenses formed in such a cell exhibit focusing properties at a voltage below 7 V and defocusing—at higher voltages.

The best optical properties were observed for LC microlenses with small ratio of the hole diameter L to the NLC layer thickness d (L/d = 1–5). In particular, for an LC layer thickness below 100 μm (which provides for a sufficiently good orientation of NLC molecules) the lens diameter must not exceed a few hundred microns. By their focusing properties, the nonsymmetric planar LC microlens arrays are comparable with their symmetric counterparts [5], while a simpler structure makes the former more promising in microoptical applications.

Using the Fresnel approximation, the focal distance of an LC microlens can be determined by the formula

$$f = \frac{\pi(L/2)^2}{(\Delta\varphi(0) - \Delta\varphi(L/2))\lambda}, \quad (1)$$

where $\Delta\varphi(0)$ and $\Delta\varphi(L/2)$ are the phaseshifts between the ordinary and extraordinary rays of light with a wavelength λ at the center and at the edge of the cell. For an arbitrary point in the aperture,

$$\Delta\varphi_i = 2\pi\Delta n_i d/\lambda, \quad (2)$$

where Δn_i is the liquid crystal birefringence.

Let us estimate the focal distance of an LC microlens. According to formula (2), the maximum phaseshift $[\Delta\varphi(0) - \Delta\varphi(L/2)]_{max} = 2\pi(n_e - n_0)d/\lambda$, where n_e and n_0 are the refractive indices for the extraordinary and ordinary light rays, respectively. For the visible light, the Δn value in NLCs reaches 0.2–0.3. For an

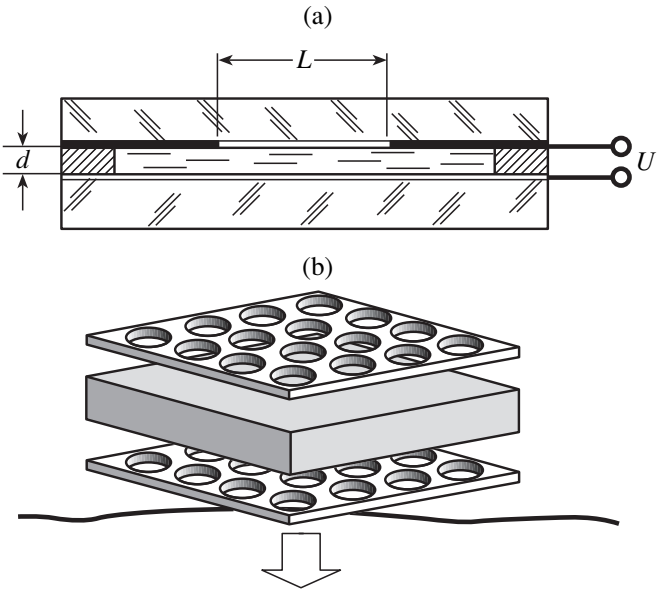

Fig. 1. Schematic diagrams showing (a) an LC microlens unit and (b) a telescope system employing an LC microlens array.

NLC layer thickness of 50–100 μm and a hole diameter of several hundred of microns, the focal distance of a microlens is on the order of a few millimeters.

The optical elements described above operate at small control voltages, exhibit low power consumption, are simple to manufacture, and allow a relatively low cost of production. It should be noted that optical systems implementing these elements have sufficiently small dimensions. Here we suggest for the first time the employment of an LC microlens array in the optical limitation system (Fig. 1b).

An array of nonsymmetric LC microlenses was fabricated in the form of a flat LC cell with electrodes deposited onto the inner faces of glass plates. One electrode represented a transparent ITO film ($SnO_2 + In_2O_3$) and the other—an aluminum film with round holes made with the aid of a conventional photolithographic process. A SiO_2 film formed by the oblique deposition technique on the electrode surfaces provided for a planar NLC orientation in the cell. The cell was filled with a nematic liquid crystal composition possessing $\Delta\varepsilon = 10$. We have prepared and studied the microlens arrays with various geometric parameters. The hole diameter was varied from 55 to 300 μm; the NLC layer thickness d was 60 or 100 μm. The focal distance of the LC microlenses was determined by the edge segment technique. A He–Ne laser radiation transmitted through a cell placed between crossed polarizers entered a microscope connected to a CCD matrix detector. The resulting image was displayed on a PC monitor.

We have studied the focusing properties of LC microlenses with different L/d ratios at various applied voltages. In a zero applied voltage, the system exhibited no focusing properties and transmitted well the incident radiation. As a voltage was applied, each element in the LC microlens array focused the light. Measurements of the focal distance for all the arrays studied showed that, as the applied voltage was increased, the absolute value of the focal distance initially decreased, then passed through a minimum, and began to increase. On further increase in the applied voltage, the optical properties of microlenses exhibit inversion.

In experiments on the optical limitation, an LC microlens array was brought into optical contact with a cell containing a medium possessing nonlinear absorp-

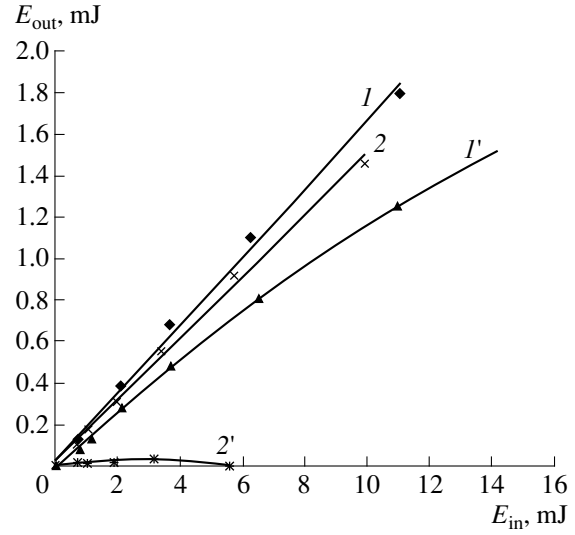

Fig. 2. Plots of the output versus input radiation energy illustrating the optical limitation effect in an LC microlens array in contact with a nonlinearly absorbing medium (fullerene C_{70} solution in toluene): (*1*, *1*') **E** ∥ **n**; (*2*, *2*') **E** ⊥ **n**; (*1*, *2*) zero applied voltage; (*1*', *2*') nonzero applied voltage.

tion properties. For this purpose, we have used a C_{70} fullerene solution in toluene. The fullerene concentration was 2.3×10^{-3} mol/l. The cell thickness was selected so as to place the absorbing medium at a focal plane of the microlens array. The medium was exposed to a high-intensity radiation pulses of a Nd:YAG laser ($\lambda = 532$ nm; pulse duration, 1 ns). The radiation was detected by calibrated FD-23 photodiodes and an IEK-1 calorimeter. The output radiation energy was studied as a function of the incident laser radiation energy.

Figure 2 shows typical experimental curves of E_{out} versus E_{in}. The measurements were performed for both parallel and perpendicular polarization of the incident light relative to the LC director orientation. The incident radiation polarized perpendicularly to the LC director was virtually not transmitted through the cell with applied voltage (Fig. 2, curve *2*') because of strong scattering. The results for the radiation with a parallel polarization show the effect of optical limitation (on a level of ~3 mJ) in the system studied (cf. curves *1* and *1*' in Fig. 2).

Thus, we have demonstrated the possibility of using LC microlens arrays in the optical limitation systems. Obvious advantages of such systems are a considerable reduction in size, low cost, and simple production technology.

REFERENCES

1. *ANSI Z136. 1-1993*, American National Standard for the Safe Use of Lasers. TB MED 524, 20 June 1985.
2. M. J. Miller, A. G. Mott, and B. P. Ketchel, Proc. SPIE **3472**, 24 (1998).
3. Nonlinear Opt., **21** (1999).
4. T. Nose, S. Masuda, and S. Sato, Jpn. J. Appl. Phys. **31**, 1644 (1992).
5. A. Gvozdarev and G. Nevskaya, Mol. Cryst. Liq. Cryst. **329**, 81 (1999).

Translated by P. Pozdeev

Technical Physics Letters, Vol. 27, No. 1, 2001, pp. 55–57. Translated from Pis'ma v Zhurnal Tekhnicheskoĭ Fiziki, Vol. 27, No. 2, 2001, pp. 30–35.

High-Quality ZnO/GaN/α-Al_2O_3 Heteroepitaxial Structures Grown by CVD

B. M. Ataev*, I. K. Kamilov*, W. V. Lundin, V. V. Mamedov*, A. K. Omaev*, and Sh.-M. O. Shakhshaev****

** Institute of Physics, Dagestan Scientific Center, Russian Academy of Sciences, ul. 26 Bakinskikh Komissarov 94, Makhachkala, 367003 Dagestan, Russia*

*** Ioffe Physicotechnical Institute, Russian Academy of Sciences, St. Petersburg, 194021 Russia*

e-mail: caucasus@datacom.ru

Received June 2, 2000

Abstract—The first results on the preparation of (0001)ZnO/(0001)GaN/(0001)α-Al_2O_3 heteroepitaxial structures by CVD in a low-pressure flow-type reactor are reported. Study of the surface morphology and X-ray diffraction patterns showed high structural perfection of the zinc oxide layer, with a block misorientation in the basal plane not exceeding 21′. The photoluminescence spectra of samples exhibited dominating emission in the exciton region. *© 2001 MAIK "Nauka/Interperiodica".*

In recent years, extensive investigations have been devoted to the structure of group III nitrides, which are related primarily to the search for effective sources of light, including the induced emission, in the short-wavelength region of the visible spectral range. High hopes in this respect are also connected with zinc oxide—a material exhibiting effective exciton luminescence in the near-UV spectral region (binding energy, 60 meV) and capable of producing stimulated high-temperature emission.

Solving the task is hindered by the absence of defect-free single crystals of sufficiently large size and by the difficulties in growing high-quality heteroepitaxial structures (in view of the absence of proper substrates). The heteroepitaxial structures are usually grown on sapphire substrates, despite a considerable lattice mismatch: Al_2O_3 (a = 4.754 Å, c = 12.99 Å); GaN (a = 3.189 Å, c = 5.185 Å); ZnO (a = 3.250 Å, c = 5.213 Å). Note that, according to [1], it is difficult to grow (0001)-oriented zinc oxide layers on the sapphire substrates of basal orientation by a conventional CVD method; the lattice mismatch in this system reaches 38%.

Apparently, using substrates possessing a lower lattice mismatch with the deposit would provide for a markedly better layer quality, especially in the transition region. A close matching between the ZnO and GaN crystal lattices can be used for obtaining high-quality heteroepitaxial structures of both ZnO on GaN and vice versa. This combination offers some additional advantages, such as a small difference of the thermal expansion coefficients or closely similar band structures. Although the good prospects of the ZnO/GaN based heteroepitaxial structures are obvious, only a few papers have been devoted to the growth of ZnO on the GaN surface [2, 3] and no data at all have been reported on the CVD of these structures in low-pressure flow-type reactors.

Below we report the first results on the growth of high-quality epitaxial layers of (0001)ZnO on the surface of a (0001)GaN/(0001)α-Al_2O_3 structure by CVD in a low-pressure flow-type reactor. The lattice mismatch of the ZnO/GaN system does not exceed 1.8%. We have also evaluated the structural perfection and studied the photoluminescence spectra of the heteroepitaxial structures obtained.

The epitaxial layers of (0001)GaN on (0001)α-Al_2O_3 were obtained by MOCVD using a low-temperature buffer layer technique [4]. The GaN layer thickness on sapphire was 2–3 μm. These structures were transferred into a low-pressure flow-type reactor without preliminary cleaning and polishing procedures. The ZnO layers were grown in a flow of hydrogen (1 l/h) at a substrate temperature of 620°C. The low-pressure flow-type reactor and the process of temperature and gasodynamic regime optimization were described elsewhere [5]. The final ZnO layer thickness was 3–5 μm.

Figure 1 shows a microphotograph illustrating the surface morphology of a (0001)ZnO layer (MII-4 interference microscope; magnification, ×560) with clearly revealed regular hexagons typical of the c plane. This surface morphology is characteristic of the layers grown at a substrate temperature T below 610°C. As the substrate temperature increased, the growth figures decreased in size, and, at T > 620°C, no relief such as that displayed in Fig. 1 was manifested (at the same magnification) and the surface became mirror smooth.

The X-ray diffraction measurements were performed on a DRON-2 diffractometer using a CuK_α radiation monochromated with a pyrographite crystal.

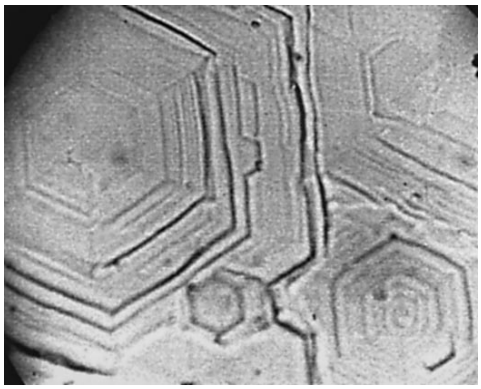

Fig. 1. A microphotograph showing the growth morphology of a CVD (0001)ZnO/(0001)GaN/(0001)α-Al_2O_3 heteroepitaxial structure (h = 3 μm; T = 610°C; magnification, ×560).

Figure 2 shows a typical diffraction pattern of the ZnO layer grown as described above. The diffractogram shows clearly pronounced (000*l*) orientation in the absence of reflections characteristic of the other orientations. Note that the (0002)ZnO and GaN peaks were not resolved because of the close crystal structures of these materials. The top inset in Fig. 2 shows the possibility of resolving the (0004)ZnO and (0004)GaN peaks, but the increase in resolution is accompanied by the appearance of peaks due to fine structure of the CuK_α line.

Study of the rocking curve of the (0002) reflection showed that misorientation of the crystal blocks in the *c* plane does not exceed 21′. However, the presence of only a series of (000*l*) reflections in the X-ray diffractogram does not allow us to draw a final conclusion concerning the degree of crystal structure perfection, since the focusing method employed reveals only the reflections from blocks parallel to the film surface. For this reason, the ZnO layers were additionally studied by electron diffraction on an EMR-100 electronograph. Based on the results of these combined investigations, it was possible to judge the high structural perfection of the (0001)ZnO layers grown by CVD on the (0001)GaN surface. We believe this result to be primarily due to the high degree of matching of the ZnO and GaN crystal lattices.

Of special interest was to study the UV photoluminescence (PL) of the epitaxial ZnO layers, since an analysis of fine features of the exciton spectra may provide additional information on the crystal structure perfection of samples (see, e.g. [6]). We have studied the exciton luminescence spectra measured at 77 K using the heteroepitaxial structures immersed directly into liquid nitrogen. Figure 3 shows a typical structure recorded in a standard setup based on an SPM-2 monochromator. It should be noted that the luminescence intensity in the UV spectral region was markedly (by a factor of more than 30) greater than in the green band (see the inset in Fig. 3).

The spectrum of exciton luminescence was characteristic of high-quality ZnO films and exhibited a dominating contribution of emission due to the free exciton A1 and a less intense emission due to the bound exciton J_d (the spectra were identified as in [7]). The ratio of intensities of the phonon replicas 1LO/2LO and their halfwidths were also indicative of a highly perfect sample structure, at least in the near-surface region of the ZnO films studied (the absorption coefficient in the spectral range of excitation and detection of the UV photoluminescence is ~10^4 cm^{-1}). A perfect structure in the transition region of such heteroepitaxial systems was also reported in [2].

Thus, the use of GaN buffer layers on sapphire for the subsequent growth of ZnO layers with the basal ori-

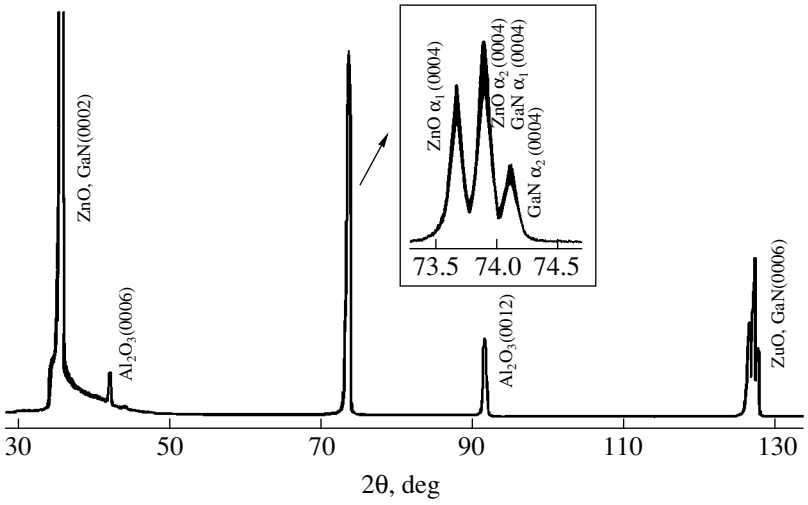

Fig. 2. X-ray diffraction pattern of a CVD (0001)ZnO/(0001)GaN/(0001)α-Al_2O_3 heteroepitaxial structure.

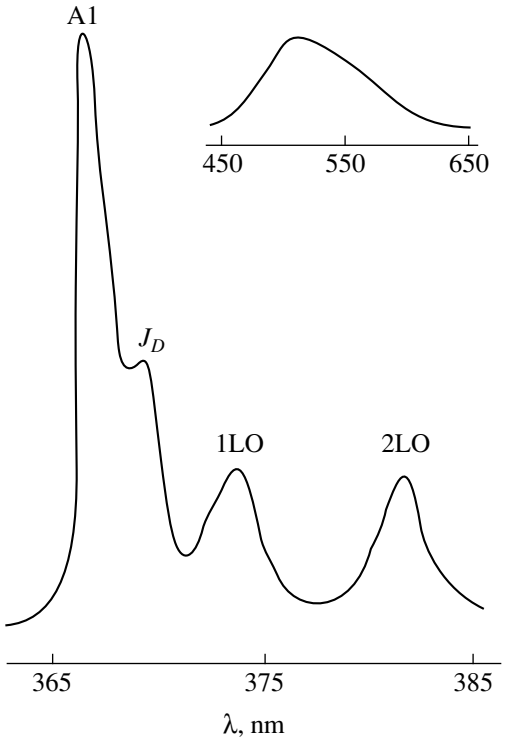

Fig. 3. Photoluminescence spectrum (77 K) of a high-quality epitaxial ZnO layer grown on an (0001)GaN/(0001)α-Al_2O_3 substrate.

entation allowed us to significantly increase both crystal perfection and the luminescent characteristics of the epitaxial zinc oxide layers (which opens the way to creating a UV laser based on these structures). This result is primarily due to the considerably reduced crystal lattice mismatch. Further progress can be related to optimization of the technological parameters used for preparation of both the buffer GaN layer and the ZnO layers in relation to their particular application. The results of these investigations and the study of stimulated emission from heterostructures will be reported soon.

Acknowledgments. The work was supported by the Russian Foundation for Basic Research, project no. 98-02-16141.

REFERENCES

1. S. A. Semiletov, G. F. Kuznetsov, A. M. Bagamadova, *et al.*, Kristallografiya **23** (2), 357 (1978) [Sov. Phys. Crystallogr. **23**, 197 (1978)].
2. S.-K. Hong, H.-J. Ko, Y. Chen, and T. Yao, J. Cryst. Growth **209**, 537 (2000).
3. R. D. Vispute, V. Talyansky, S. Choopun, *et al.*, Appl. Phys. Lett. **73**, 348 (1998).
4. W. V. Lundin, B. V. Pushnyi, A. S. Usikov, *et al.*, Inst. Phys. Conf. Ser. **155**, 319 (1997).
5. A. Kh. Abduev, B. M. Ataev, and A. M. Bagamadova, Izv. Akad. Nauk SSSR, Neorg. Mater., No. 11, 1928 (1987).
6. B. M. Ataev, A. M. Bagamadova, and V. V. Mamedov, Thin Solid Films **283**, 5 (1996).
7. A. Kh. Abduev, A. D. Adukov, B. M. Ataev, *et al.*, Opt. Spektrosk. **50** (6), 1137 (1981) [Opt. Spectrosc. **50**, 626 (1981)].

Translated by P. Pozdeev

Technical Physics Letters, Vol. 27, No. 1, 2001, pp. 58–59. Translated from Pis'ma v Zhurnal Tekhnicheskoĭ Fiziki, Vol. 27, No. 2, 2001, pp. 36–41.

100-Watt Laser Bars Based on Phase-Locked Arrays

D. M. Demidov, A. N. Ivkin, N. I. Katsavets, S. V. Kokin, R. V. Leus, A. L. Ter-Martirosyan, and V. P. Chalyĭ

Poluprovodnikovye Pribory, Joint Stock Company, St. Petersburg, 194156 Russia

Received September 14, 2000

Abstract—High-power diode laser bars (DLBs) based on InGaAlAs quantum-confinement heterostructures with an output optical power of no less than 100 W in a quasi-continuous wave regime (pulse duration, 200–400 μs; repetition rate, 50–100 Hz) were fabricated and investigated. A bar of this type consists of a set of strip emitters, each representing an optimized phase-locked array of single-mode emitters. This design provides for a considerably improved temporal and spatial stability of the DLB emission, with a simultaneous decrease in the optical noise level. © *2001 MAIK "Nauka/Interperiodica"*.

The development of the rare-earth solid-state lasers employing high-power diode lasers (DLs) and diode laser bars (DLBs) as an optical pump source, the so-called diode-pumped solid-state lasers (DPSSLs), is an important field of activity in science and technology. This field has expanded rapidly during recent years, since DPSSLs combine the advantages of semiconductor lasers (the small size and high efficiency of electrical to optical energy conversion) with the high quality of the output beam typical of solid-state lasers (high temporal and spatial coherence and narrow radiation diagram).

However, a problem with DPSSLs is the spatial and temporal instability of their emission and increased noise level. This is mainly related to the so-called emission filamentation exhibited by DLs and DLBs with a wide continuous strip contact [1]. This effect is manifested by the lasing via temporally and spatially unstable channels formed in the DL cavity due to nonlinear optical phenomena.

Previously [2, 3], we proposed a new high-power DL design for solid-state laser pumping. This kind of laser represents a phase-locked array of single-mode emitters with optimized optical coupling, characterized by increased uniformity of the optical power density distribution over the mirror, which provides for higher output power and enhanced DL reliability [4]. At the same time, elimination of the filamentation effect results in a considerably increased stability with simultaneous reduction in the optical noise [5].

In the present paper we report on the development and investigation of high-power ($P \geq 100$ W) DLBs based on phase-locked arrays, operating in the quasi-continuous wave regime (pulse duration, 200–400 μs; repetition rate, 50–100 Hz).

DLBs were fabricated from heterostructures with separate electron and optical confinement. The structures, which have a strained InAlGaAs quantum-confinement active region, were grown by MOCVD on [100]-oriented GaAs substrates. The wide-gap n-$Al_{0.6}Ga_{0.4}As$:Si and p-$Al_{0.6}Ga_{0.4}As$:Zn emitting contacts were about 1.5 μm thick. The aluminum content in the $Al_xGa_{1-x}As$ waveguide layers (with a total thickness of 0.3 μm) was varied from $x = 0.6$ at the contacts to $x = 0.3$ at the active layer.

Fabricated DLBs have the form of a 200-μm-period system of strip emitters integrated on a single substrate, but not optically coupled with each other. Each strip emitter has a 160-μm-wide emitting region representing a phase-locked array of single-mode emitters. The heterostructure profiling is performed by ion etching through a photoresist mask by a partially neutralized collimated beam of argon ions with energies below 1000 eV. The total width of the DLB emitting region amounts to 11000 μm. The optical coupling between the single-mode emitters is optimized by the choice of the p-contact profiling depth. The DLB back and front facets are covered, respectively, by a multilayer reflective coating with a reflectivity of about 95% and an antireflection coating with a reflectivity of about 10%. After deposition of these coatings, DLB is soldered with its p-layer to a nickel-plated copper heat sink.

The current–power characteristics were recorded using a LaserMate (Coherent Co.) calibrated bolometric power meter. The optical pulse power was calculated as $P_1 = P_2\nu$, where P_2 is the DLB output optical power time-averaged by the bolometer and ν is the duty factor of the laser pulses. The spectral measurements were carried out using an automated measuring complex based on an MDR-23 monochromator. The near-field DLB radiation pattern was recorded by a CCD matrix, and the far-field one, by a conventional technique using the DLB angle scanning.

Figure 1a shows a typical DLB current–power characteristic. A standard DLB operating current, corresponding to the output optical power of 100 W, is 115 A, and a threshold current density is not exceeding 200 A/cm^2. The differential quantum efficiency equals 1 W/A (65%), and the efficiency of electrical to optical

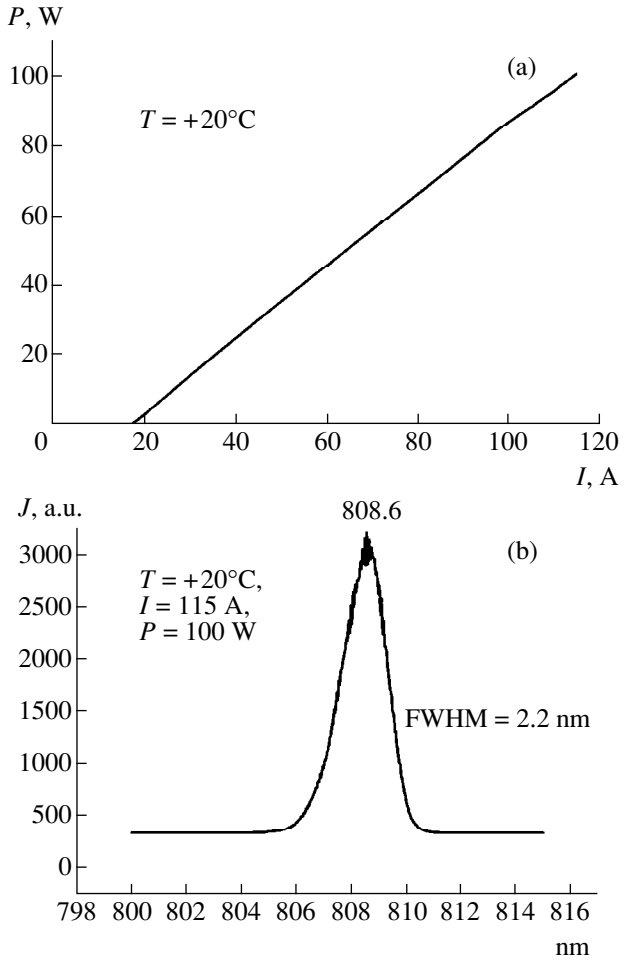

Fig. 1. (a) DLB current–power characteristic (pulse duration, 200 μs; repetition rate, 50 Hz). (b) DLB lasing spectrum.

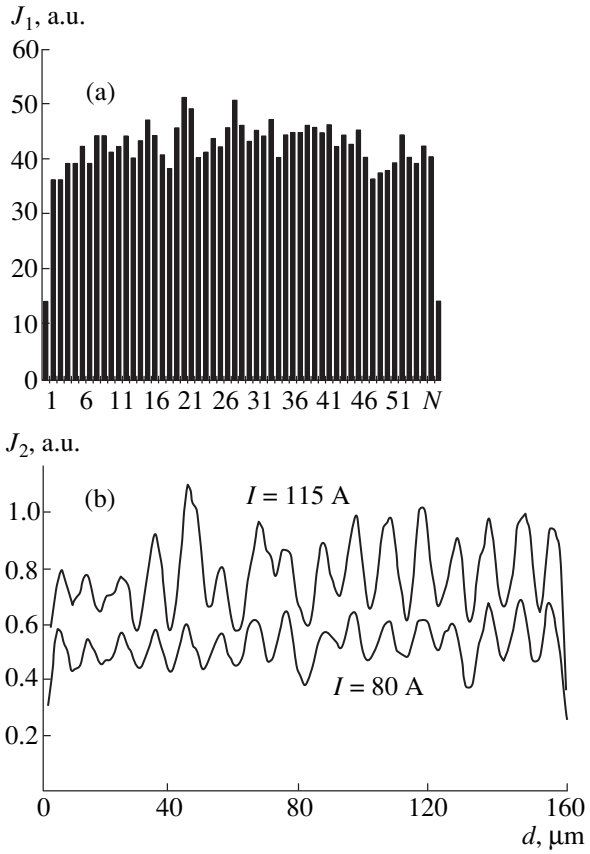

Fig. 2. (a) Distribution of the optical power between the DLB strip emitters (J_1 stands for the lasing intensity and N, for the strip emitter number). (b) Distribution of the optical power in the near-field region of a strip emitter for different pump currents (J_2 stands for the radiation intensity and d, for the distance along the DLB mirror).

power conversion is higher than 40%. The laser emission spectrum width at the operating current does not exceed 2.2–2.5 nm (Fig. 1b).

Distribution of the radiation power between strip emitters is highly uniform over the whole width of the emitting region (see Fig. 2a), which gives evidence of the heterostructure quality and the perfection of all postgrowth technological processes involved in the DLB fabrication. With the implemented DLB design, variations in the bar pump current or heat-sink temperature do not result in a shift of the optical power maxima in the near-field region of individual strip emitters (see Fig. 2b). Thus, the emission filamentation, which shows up as spontaneous chaotic redistribution of the emission maxima at the DL mirror, is not observed.

Owing to the high output optical power, narrow lasing spectrum, and good spatial and temporal stability of emission, DLBs based on phase-locked arrays are promising as pump sources for low-noise rare-earth-ion solid-state lasers. In addition, with an optimized heat sink design, the developed DLBs can be used as basic elements for assembling laser matrices with output powers of 1 kW or higher.

Acknowledgments. This study was supported by the Russian Ministry of Science and Technology (State Contract no. 35/5 of December 24, 1998) under the "Scientific Instrumentation" Program.

REFERENCES

1. H. C. Casey, Jr. and M. B. Panish, *Heterostructure Lasers*, Part B: *Materials and Operating Characteristics* (Academic, New York, 1978).
2. D. M. Demidov, N. I. Katsavets, R. V. Leus, *et al.*, Pis'ma Zh. Tekh. Fiz. **23** (8), 90 (1997) [Tech. Phys. Lett. **23**, 331 (1997)].
3. H. Grempel, N. I. Katsavets, D. M. Demodov, *et al.*, Proc. SPIE **3682**, 47 (1998).
4. D. M. Demidov, N. I. Katsavets, A. L. Ter-Martirosyan, and D. Kroupsky, Proc. SPIE **4059**, 225 (2000).
5. D. M. Demidov, N. I. Katsavets, A. L. Ter-Martirosyan, and V. P. Chalyĭ, Kvantovaya Élektron. (Moscow) **25** (9), 789 (1998).

Translated by M. Skorikov

Technical Physics Letters, Vol. 27, No. 1, 2001, pp. 6–8. Translated from Pis'ma v Zhurnal Tekhnicheskoĭ Fiziki, Vol. 27, No. 1, 2001, pp. 12–18.

Instability of a Homogeneous Plastic Flow and Strain Localization in Structurally Inhomogeneous Media

V. F. Badaeva, P. P. Kaminskiĭ, and Yu. A. Khon

Institute of Strength Physics and Materials Science, Siberian Division, Russian Academy of Sciences, Tomsk, 634055 Russia

Received July 27, 2000

Abstract—Changes in the internal structure of a deformed medium are described, in addition to the defect densities, by the kinetic variables (order parameters) related to the collective modes of the macroscopic plastic deformation. The kinetic equations for two order parameters represent a system of nonlinear equations of the reaction–diffusion type. It is demonstrated that instability of a homogeneous solution with respect to inhomogeneous perturbations appears when the characteristic variation lengths of the order parameters markedly differ from each other. *© 2001 MAIK "Nauka/Interperiodica".*

The phenomenon of localization of a macroscopic strain at the end of a homogeneous plastic flow stage is an important feature of the process of irreversible shape variation in solids. The further straining under the same deformation conditions proceeds mostly at the expense of changes in the internal structure in the strain localization region. The localization of a strain may be accompanied by the neck formation in a sold subject to tensile deformation, which is followed by the accumulation of discontinuities and breakage of the sample. It is the latter circumstance that explains a large number of publications devoted to elucidation of the mechanisms of deformation and construction of the models describing the phenomenon of strain localization in solids (see, e.g., [1–7]). Below, we will consider some of the major laws governing this process, which are established in these investigations.

Localization of the macroscopic strain may take place in materials possessing various internal structures, including single crystals, polycrystalline solids, submicrocrystalline and amorphous materials, etc. The mechanisms and the corresponding modes of the homogeneous plastic deformation can be different as well. For example, single-crystal fcc metals may exhibit shear by two conjugated crystallographic systems of slip planes [1]. In a submicrocrystalline structure of copper, the nondislocation mechanisms caused by the appearance of a platelike mesastrips with a thickness on the order of 10 μm dominate [7]. In any case, at least two deformation modes are operative before the onset of strain localization. During this period, changes in the internal structure possess a collective character and take place over volumes with the characteristic dimensions varying from a fraction of micron to the whole sample [1].

The internal structure of the localized strain zone may exhibit a gradual qualitative variation with increasing degree of straining, which is reflected by different stages observed in the plastic flow curve [8]. At least two deformation modes are operative in each stage. It was pointed out [1] that the problem of description of the macroscopic strain localization in a crystal cannot be solved within the framework of the dislocation models. There is sufficient ground to believe that point defects, in particular, vacancies, play a significant role as well [9]. The contribution of diffusion processes to the plastic deformation of crystals cannot be considered as small even at relatively low temperatures. Deformation modes related to the motion of point defects are of the accommodation type with respect to the shear along the slip planes (both crystallographic and noncrystallographic) [7]. As a result, the internal structure changes in such a manner that the material exhibits a viscous flow without significant hardening [1].

Thus, the internal structure changes in the stage of both homogeneous and localized flow via at least two deformation modes. Each of these modes is characterized by a length, exceeding which the change takes place, and by the corresponding variation time. A question naturally arises as to what is a relationship between these values for which a homogeneous plastic flow becomes unstable with respect to inhomogeneous perturbations in then internal structure. Since the phenomenon of strain localization is observed in all systems irrespective of their internal structure, we may expect that an answer to this question can be obtained in the general form. Below, we describe one possible variant of solving this task.

Changes in the internal structure mediating the plastic deformation process always proceed within the local stress concentrator bands (SCBs) [10]. Below, we will refer these bands as active. The mechanisms of macroscopic plastic deformation in the active SCBs can be

1063-7850/01/2701-0006$21.00

diverse, including the production and evolution of defect ensembles in the in the crystalline lattice, diffusion of atoms, structure and phase transformations, reorientation of grains and mutual displacement of grains in polycrystals, formation of pores and microcracks, and some others. At a preset temperature and a given macroscopic deformation rate, each active SCB features a combination of interrelated mechanisms and corresponding deformation modes, which provides for the required variation in the sample shape at a minimum applied stress.

The spatial distribution of active SCBs determines the character of straining; their number, the local value of the macroscopic plastic strain. For a homogeneous straining, the density of active bands is the same at each point of the sample; that is, their homogeneous distribution is stable with respect to any small perturbation. The transition to localized straining implies that the homogeneous distribution of active SCBs becomes unstable with respect to inhomogeneous density perturbations. Therefore, it would be expedient to use the active SCB concentrations as variables describing the macroscopic plastic straining [11]. By their meaning, these variables appear as the order parameters. The number of the order parameters is determined by that of the dominating plastic straining modes. Below, we will consider the case of a system with two order parameters (p and q).

Equations for the order parameters are essentially the usual balance equations for the number of particles, which can be written in the following form [11]:

$$t_p \partial p/\partial t = P(p, q, \tau/\tau_p, \tau/\tau_q) + l_p^2 \Delta p, \quad (1)$$

$$t_q \partial q/\partial t = Q(p, q, \tau/\tau_p, \tau/\tau_q) + l_q^2 \Delta q, \quad (2)$$

where t is the time; t_p, t_q are the characteristic times; l_p, l_q are the characteristic lengths of variation of the parameters p and q, respectively; and τ, τ_p, τ_q are parameters of the nonlinear source functions P and Q, the value of τ representing the local stress and p and q, the characteristic stresses corresponding to excitation of the local deformation modes related to the order parameters p and q, respectively. The characteristic lengths $l_P = (D_P t_P)^{1/2}$ and $l_Q = (D_Q t_Q)^{1/2}$ in Eqs. (1) and (2) are determined by the corresponding transfer coefficients D_P and D_Q. Thus, the set of the particle number balance equations written in the form of Eqs. (1) and (2) implies that the flux densities of the order parameters are proportional to their gradients Δp and Δq. Being proportional to the transfer coefficients, the factors at the gradients reflect a random character of the internal stress variation within the active SCBs in structurally inhomogeneous media.

Once determined, the solutions $p = p(\mathbf{r}, t, \tau/\tau_p, \tau/\tau_q)$ and $q = q(\mathbf{r}, t, \tau/\tau_p, \tau/\tau_q)$ to Eqs. (1) and (2), where r is the radius-vector of a given point in the sample, determine the spatial and temporal variation of the macroscopic plastic strain tensor components for various stress levels and loading conditions. Equations of the type of (1) and (2) are well known in the theory of self-sustained wave processes and self-organization in the physical, chemical, and biological systems. For this reason, various possible types of solutions for the kinetic variables have been studied in sufficient detail [12]. Introduction of the order parameters reduces the task of describing the localization of plastic flow to analysis of the possible scenarios of the strained medium self-organization under the action of stress representing the control parameter. The subsequent analysis refers to an ideal homogeneous system representing a medium without macroscopic structural inhomogeneities, featuring constant stresses at each point.

For $\tau \ll \tau_p$ and $\tau \ll \tau_q$, the strain possesses an elastic character and the SCBs exhibit no structural changes, which implies that the only solution to Eqs. (1) and (2) is $p = q = 0$. Moreover, this solution must be stable with respect to the small perturbations of any type, so that the derivatives $P'_p \equiv \partial P/\partial p$ and $Q'_q \equiv \partial Q/\partial q$ at this point must be negative. For a stress level $\tau_0/\tau_p \approx \tau_0/\tau_q \approx 1$, the presence of a homogeneous plastic straining stage indicates that there must be at least one more homogeneous solution $p_h > 0$, $q_h > 0$. The p_h and q_h values can be determined by solving the system of equations $P = Q = 0$. The solution stability with respect to small perturbations δp, $\delta q \propto \exp(-\gamma t + l\mathbf{kr})$, where $\mathbf{k}$ is the wavevector, determines the character of straining at the point p_h, q_h. The condition of stability with respect to small homogeneous perturbations ($\mathrm{Re}\gamma > 0$, $k = 0$) has the following form:

$$t_q P'_p + t_p Q'_q < 0, \quad (3)$$

$$P'_p Q'_q - P'_q Q'_p > 0, \quad (4)$$

where the derivatives are calculated at the point p_h, q_h.

The solution is stable with respect to small inhomogeneous perturbations related to the stress variations (the Turing instability) provided that the system satisfies, in addition to conditions (3) and (4), the following inequality:

$$k^4 l_p^2 l_q^2 - (l_q^2 P'_p + l_p^2 Q'_q) k^2 + P'_p Q'_q - P'_q Q'_p < 0. \quad (5)$$

To this end, one of the derivatives (e.g., Q_q) must be positive and the other (P'_p), negative. The wavevector magnitude fall within the interval

$$k_0^2 - D^{1/2} \le k^2 \le k_0^2 + D^{1/2}, \quad (6)$$

where D is the discriminant of Eq. (5) considered as a quadratic equation with respect to k^2 and

$$k_0^2 = (l_q^2 P'_p + l_p^2 Q'_q)/2 l_p^2 l_q^2. \quad (7)$$

The condition of positive D value implies that the

derivative Q'_q must satisfy the following inequality:

$$Q'_q > -\varepsilon^2 P'_p + 2\varepsilon(P'_p Q'_q - P'_q Q'_p)^{1/2}, \quad (8)$$

where $\varepsilon = l_q/l_p = (D_Q t_Q/D_P t_P)^{1/2}$.

The smaller the ε value, the more readily the last inequality is fulfilled. In other words, the strain localization is favored by deformation modes such that (i) $D_Q \ll D_P$ with $t_Q \approx t_P$ or (ii) $t_Q \approx t_P$ with $D_Q \approx Q_P$ or $D_Q t_Q \ll D_P t_P$. A reason for the instability is that the parameter p varies only slightly over the length $l_q \ll l_p$, while small perturbations δq increase for $Q'_q > 0$ [12]. As a result even small distances on the order of l_q feature a sharp increase in the value of variable q.

The validity of inequality (6) depends on dimensions of the sample. Indeed, the wavevector of a parallelepiped sample obeys (to within a constant factor depending on the boundary conditions) the relationship

$$k^2 \approx (m^2/X^2 + n^2/Y^2 + i^2/Z^2), \quad (9)$$

where m, n, i are integers varying from zero to infinity and X, Y, Z are the sample length, width, and height (thickness), respectively. For $X \gg Y$, $X \gg Z$, and a fixed value of $k^2 = k_0^2$, condition (9) is fulfilled only for $n = i = 0$. If the value $m = 1$ corresponds to a single localized strain band. If the X size decreases below certain critical level, condition (9) is no longer valid and the strain is not localized for the old l_p and l_q values.

Thus, a physical reason for the instability of a homogeneous plastic flow and the strain localization in a structurally inhomogeneous medium at $\tau > \tau_0$ is the appearance of mechanisms and the corresponding deformation modes with markedly different characteristic length of the internal structure variation. An example is offered by a system where one deformation mode is related to shears via certain system of slip planes and the other, to the diffusion of atoms. Here, a high vacancy concentration appears as a result of the intersection of dislocations under the action of external stresses [1]. All other deformation modes either appear at higher stresses or possess large characteristic times of the internal structure variation.

In conclusion, it should be recalled that condition (5), corresponding to the strain localization, was derived for the ideal homogeneous state. The presence of even very small inhomogeneities in the system may dramatically change its self-organization scenarios and lead to the appearance of localized structures at a level of stresses markedly lower than that required to induce separation in a homogeneous state [12]. Analysis of the conditions necessary for the formation of such structures requires separate investigation.

Acknowledgments. The authors are grateful to E. E. Slyadnikov for fruitful discussions.

REFERENCES

1. V. I. Al'shits and G. V. Berezhkova, in *Physical Crystallography: Collection of Scientific Works* (Nauka, Moscow, 1992), pp. 129–151.
2. F. R. N. Nabarro, in *Proceedings of the 7th International Conference on the Strength of Metalls and Alloys (ICSMA-7), Montreal, 1985*, Ed. by H. J. McQueen *et al.* (Pergamon, Oxford, 1986), Vol. 3, p. 1667.
3. J. C. Cowie and F. R. Tuller, Mater. Sci. Eng. **95** (1), 93 (1987).
4. C. A. Pampillo and D. E. Polk, Acta Metall. **22** (6), 741 (1974).
5. A. S. Argon, Glass Sci. Technol. (Amsterdam) **5**, 79 (1980).
6. V. Z. Bengus, E. D. Tabachnikova, V. V. Gaĭko, *et al.*, Metallofizika (Kiev) **8** (5), 3 (1986).
7. V. E. Panin, L. S. Derevyagina, and R. Z. Valiev, Fiz. Mezomekh. **2** (1–2), 89 (1999).
8. N. A. Koneva and É. V. Kozlov, Izv. Vyssh. Uchebn. Zaved., Fiz. **33** (2), 89 (1990).
9. H. Mecking and Y. Estrin, Scr. Metall. **14** (7), 815 (1980).
10. V. E. Panin, Fiz. Mezomekh. **1** (1), 4 (1998).
11. P. P. Kaminskiĭ and Yu. A. Khon, Fiz. Mezomekh. (2000) (in press).
12. B. S. Kerner and V. V. Osipov, Usp. Fiz. Nauk **160** (9), 2 (1990) [Sov. Phys. Usp. **33**, 679 (1990)].

Translated by P. Pozdeev

Technical Physics Letters, Vol. 27, No. 1, 2001, pp. 60–62. Translated from Pis'ma v Zhurnal Tekhnicheskoĭ Fiziki, Vol. 27, No. 2, 2001, pp. 42–47.

"Hidden" Recording of Phase Holograms with Self-Amplification in a Polymer with Photoinduced Diffusion

V. V. Mogil'nyĭ and Yu. V. Gritsaĭ

Belarussian State University, Minsk, 220080 Belarus

Received July 24, 2000

Abstract—The possibility of minimizing the diffraction efficiency of a volume phase holographic grating while recording in a medium with diffusion self-amplification is considered. The recording process is modeled to demonstrate that the diffraction efficiency can be varied from 0.02 to 0.003 (50–250 gain). The results of the analysis are confirmed by the experimental data. © *2001 MAIK "Nauka/Interperiodica".*

The interest in the holographic media with postexposure self-amplification is related to the possibility of recording initially low-intense interference patterns without introducing substantial distortions in the distribution of its light field [1, 2]. The nonlinearities in the amplification may also contribute to distortions in the hologram [2, 3]. A purely diffusion mechanism differs from all the known mechanisms of the postexposure self-amplification by pronounced linearity with respect to the final image [2–4]. An example of the diffusion mechanism is represented by the diffusion degradation of the distribution of unreacted photosensitive molecules in a glassy polymer medium [4]. If the diffusion uniformly distributes the photosensitive molecules, the hologram is formed by the distribution of the photoproduct following the intensity variations in the interference pattern. Note that the realization of this simple and exquisite scheme using a solution of phenathrenequinone in poly(methylmethacrylate) (PMMA) meets additional problems related to the dependence of the amplification coefficient on the spatial frequency [4].

Previously [5], we demonstrated the self-amplification of phase holograms in PMMA layers containing photodimerizing anthracene derivatives and a residual solvent. Being frequency-independent, this phenomenon is caused by the diffusion of solvent molecules trapped by the photodimers formed in the course of exposure. Inherent in such a self-amplification is the inversion of the shape of the distribution of the refractive index n. It takes place either in the course of exposure or in the postexposure period depending on the relationship between the rate of formation of the trapping centers (photodimers) and the diffusion rate. This phenomenon is predicted by expressions derived in [4], although the authors did not make the corresponding conclusions. The inversion is realized if the photochemical modulation of the refractive index is in antiphase with the distribution of the light field intensity, so that the photoreaction leads to decreasing molecular refraction and polarizability. Diffusion always modulates the refractive index in phase with the distribution of the light field.

Nonmonotonic variation of the amplitude of modulation of the refractive index and the inversion of this modulation lead to characteristic kinetics of the diffraction efficiency (DE) featuring a maximum in the initial part (at t_0) and a zero point t_i where the inversion takes place (Fig. 1a). The maximum emerges due to the com-

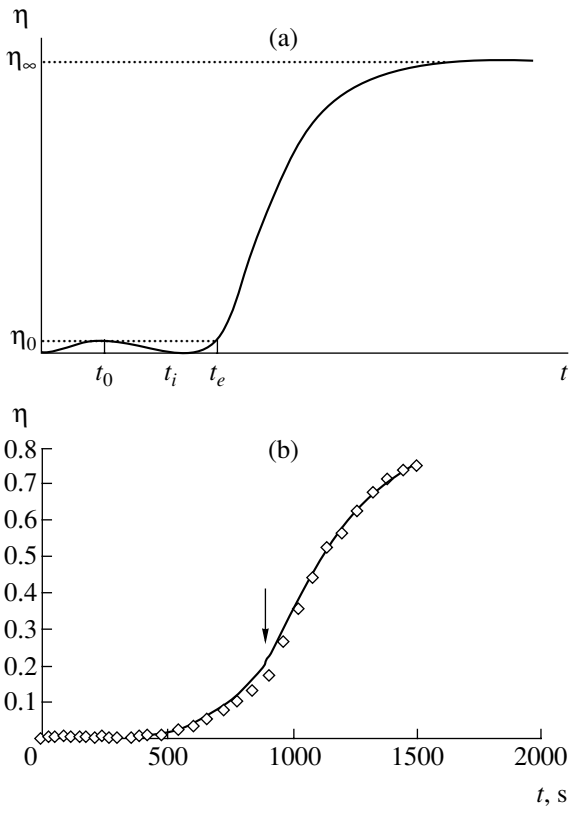

Fig. 1. (a) Typical DE kinetics; (b): (symbols) experimental data and (solid line) model curve calculated by formulas (1)–(3) for the DE evolution with time upon the recording of a volume phase holographic grating.

1063-7850/01/2701-0060$21.00 © 2001 MAIK "Nauka/Interperiodica"

petition between the photochemical and diffusion modification of the refractive index in the course of exposure. The qualitative considerations show that, by leveling the rates of the competing processes, we may decrease the first DE maximum and maintain the DE on a relatively low level for a sufficiently long time. To the best of our knowledge, no one has ever considered such a possibility, apparently because of the diversity and complexity of the processes of optical recording and amplification in such holographic media.

The "hidden" recording of the volume phase holographic can be modeled using expressions (1) and (2) from [5] for the amplitude of modulation of the refractive index Δn:

$$\Delta n = -\frac{(n^2+2)^2}{6n}k\left[\frac{R_S\delta}{\gamma}(1-\exp(-\gamma t)) + (2R_M - R_D - R_S\delta)t\right], \quad t < t_e, \tag{1}$$

$$\Delta n = \frac{(n^2+2)^2}{6n}k[R_S\delta(t_e - \gamma^{-1}\exp(-\gamma t) \times (\exp(\gamma t_e) - 1)) - (2R_M - R_D)t_e], \quad t \geq t_e, \tag{2}$$

where R_M, R_D, and R_S are the molar refractions of the photodimerizing molecules, photodimer, and photoneutral impurity (residual solvent), respectively; $\gamma = 4\pi^2\Delta\Lambda^{-2}$; D is the diffusion coefficient of the photoneutral molecules; Λ is the period of the holographic grating; δ is the trapping coefficient (the ratio of the number of the trapped photoneutral molecules to the number of photodimers); t is the current time; and t_e is the exposure time. For an optically thin layer, we have $k = I_0\varepsilon\varphi c\ln 10/(h\nu N_A)$, where I_0 and $h\nu$ are the amplitude of the intensity modulation and energy quantum of the recording light, respectively; ε is the molar extinction ratio; φ is the quantum efficiency of photodimerization; N_A is the Avogadro number; and c is the initial concentration of the photosensitive substance (anthracene derivative). The diffraction efficiency η of the volume phase holograms is given by the formula [6]:

$$\eta = \sin^2\left(\frac{\pi h\Delta n}{\lambda\cos\Theta}\right), \tag{3}$$

where h is the thickness of the recording layer, λ is the wavelength, and Θ is the incidence angle of the recording beams. It is expedient to terminate exposure after inversion, when DE reaches the first maximum value η_0 (Fig. 1a). The corresponding time t_e can be determined from the equality of the values of $|\Delta n|$ at t_0 and t_e (Fig. 1a). We can determine the value of t_0 from (1) using the condition that the derivative $d\Delta n/dt$ equals zero:

$$t_0 = -\frac{1}{\gamma}\ln\left(\frac{R}{R_S\delta}\right), \tag{4}$$

where $R = R_S\delta - 2R_M + R_D$. A relationship between γ and t_e is given by the transcendent equation following from (4) and (1):

$$2R_M - R_D + R\ln\left(\frac{R}{R_S\delta}\right) = -R_S\delta(1-\exp(-\gamma t_e)) + R\gamma t_e. \tag{5}$$

Using (1) and (2) with the allowance for (3) and (4), one can easily obtain an equation relating the maximum DE value attained in recording (η_0) to the value achieved in the amplification process (η_∞):

$$\eta_0 = \sin^2\left(\left(2R_M - R_D + R\ln\left(\frac{R}{R_S\delta}\right)\right) \times (R\gamma t_e)^{-1}\arcsin\sqrt{\eta_\infty}\right). \tag{6}$$

As the value of γ is normally predetermined by the recording conditions (the diffusion coefficient D and the period of the grating cannot be changed arbitrarily), the implementation of the "hidden" recording necessitates the proper choice of the recording light intensity. An expression for k (that is proportional to the recording light intensity) follows from (2) with the allowance of (3) and the condition $t \longrightarrow \infty$:

$$k = \frac{6n}{(n^2+2)^2}\frac{\lambda\cos\Theta\arcsin\sqrt{\eta_\infty}}{\pi h R t_e}. \tag{7}$$

In the experiment, the "hidden" recording was realized by forming a volume transmission phase holographic grating with a period of 3 μm in a PMMA layer with a thickness of 100 μm. The layer contained 10 mol % of a monosubstituted anthracene and about 10 mol % of a residual solvent (chloroform). Figure 1b shows experimental (symbols) and calculated (solid line) curves of the DE evolution with time for this experiment; the arrow indicates the moment of the exposure termination. The model curve was calculated by formulas (1)–(3) using the following values of the parameters: $\gamma = 0.0032\ s^{-1}$, $\delta = 1.92$, $k = 7.6 \times 10^{-7}$ mol/(cm^3 s) (which corresponds to recording by an argon laser with a wavelength of 488 nm and an intensity of 5 mW/cm^2) and the known quantities: $R_S = 21.5$, $R_M = 62.4$, and $R_D = 110$ cm^3/mol [5]. Under this regime, the DE is close to zero (up to exposures of about 2 J/cm^2) owing to the mutual compensation of the photochemical and diffusion contributions to the phase response of the medium.

Let us estimate the possible values of η_0 in the course of the "hidden" recording. Assume that $\eta_\infty = 1$ possesses the limiting value of unity. Then, for the given values of R_S, R_M, and R_D, the value of η_0 depends only on δ. Figure 2 shows a plot of η_0 versus δ calculated by formula (5) and (6). It is seen that $\eta_0 \approx 0.02$ at

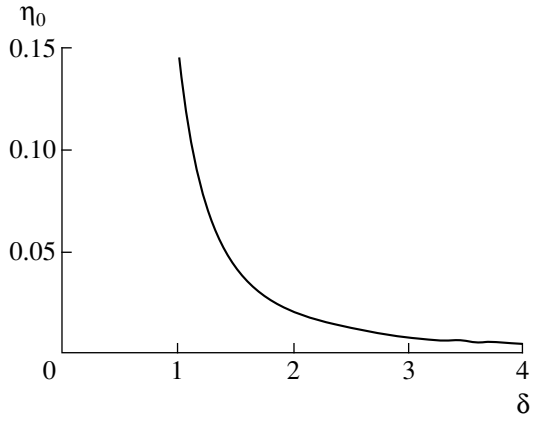

Fig. 2. A plot of the maximum DE in the course of the "hidden" recording versus the trapping coefficient.

a typical value of $\delta \approx 2$ [5]. In some experiments, we could increase δ to 4 [7], while decreasing η_0 down to 0.003–0.005. One can additionally decrease η_0 by using low-molecular-mass photoneutral components with greater molecular refraction.

Acknowledgments. The work was supported by the Belarussian Foundation for Basic Research.

REFERENCES

1. A. P. Popov, V. F. Goncharov, A. V. Veniaminov, *et al.*, Opt. Spektrosk. **66** (1), 3 (1989) [Opt. Spectrosc. **66**, 1 (1989)].
2. É. S. Gyul'nazarov, T. N. Smirnova, and E. A. Tikhonov, Zh. Tekh. Fiz. **61** (1), 111 (1991) [Sov. Phys. Tech. Phys. **36**, 66 (1991)].
3. T. A. Lukina and A. F. Skochilov, Opt. Zh. **66** (12), 84 (1999) [J. Opt. Technol. **66**, 1081 (1999)].
4. A. V. Veniaminov, V. F. Goncharov, and A. P. Popov, Opt. Spektrosk. **70** (4), 864 (1991) [Opt. Spectrosc. **70**, 505 (1991)].
5. V. V. Mogil'nyĭ and Yu. V. Gritsaĭ, Opt. Spektrosk. **83** (5), 832 (1997) [Opt. Spectrosc. **83**, 770 (1997)].
6. K. K. Shvarts, *Physics of Optical Recording in Dielectrics and Semiconductors* (Zinatne, Riga, 1986).
7. V. V. Mogilny and Y. V. Gritsai, Proc. SPIE **3402**, 100 (1998).

Translated by A. Chikishev

Technical Physics Letters, Vol. 27, No. 1, 2001, pp. 63–64. Translated from Pis'ma v Zhurnal Tekhnicheskoĭ Fiziki, Vol. 27, No. 2, 2001, pp. 48–50.

Edge Luminescence from Zinc Selenide Doped with Isovalent Magnesium Impurity

M. M. Sletov

Chernovtsy State University, Chernovtsy, Ukraine

Received June 27, 2000

Abstract—The electric and luminescent properties of zinc selenide crystals doped with the isovalent magnesium impurity were studied. It is demonstrated that low-resistivity *n*-type ZnSe layers with a dominating edge luminescence component can be obtained. © *2001 MAIK "Nauka/Interperiodica".*

Among the wide-bandgap $A^{II}B^{VI}$ compounds, zinc selenide is among the most promising materials for the fabrication of dark and pale blue light-emitting injection diodes [1]. Solving the task of preparing this material requires developing methods of obtaining reproducible low-resistivity ZnSe crystals and films of both *n*- and *p*-type with a dominating edge luminescence component.

As a result of the self-compensation effect, the bulk impurity-free stoichiometric ZnSe crystals possess a low intrinsic-defect conductivity of the electron type. The photoluminescence (PL) spectra of such samples exhibit blue (*B*) and orange (*O*) emission bands. The latter component is related to the donor–acceptor pairs involving negative doubly-charged zinc vacancies (V''_{Zn}) [2]. A decrease in concentration of the latter defects is usually achieved through prolonged annealing (hundreds of hours) of ZnSe in liquid Zn, which leads to a considerable increase in conductivity [3]. However, this treatment does not always lead to complete suppression of the *O*-band. Below we discuss a possible way to obtain low-resistivity *n*-ZnSe layers with a dominating edge luminescence component.

The idea consists in additionally doping ZnSe with an isovalent impurity, which can provide for a significant increase in the edge emission component. This effect is explained by two factors: (i) the formation of a bound exciton at the isovalent impurity and (ii) the "healing" of vacancies (which serve the centers of spurious recombination) [4, 5]. The binding of excitons at the isovalent impurity centers is related to the difference between the electronegativities of a replaced atom (χ_a) and a substituted impurity (χ_i) [5]. The difference must be as large as possible, because a decrease in $\Delta\chi = \chi_a - \chi_i$ would increase the probability of formation of the corresponding solid solutions. In order to ensure that the isovalent impurity would exhibit the donor properties (thus being capable of binding the hole), it is necessary to provide for the condition $\chi_i < \chi_a$. In addition, the effective "healing" of vacancies would be favored by the proximity of the covalent radii of the impurity and the vacancy-forming atom. Taking into account the above criteria, we selected magnesium as the isovalent impurity.

The initial ZnSe crystals were grown from the melt in an inert gas atmosphere under pressure. Around room temperature, these crystals were characterized by the conductivity $\sigma_n \approx 10^{-10}\ \Omega^{-1}\ cm^{-1}$, which was determined by the electron levels of interstitial Zn_i atoms at $E_d \approx 0.6$ eV. The PL spectrum of these crystals exhibits two bands (*B* and *O*) peaked at 2.68 and 1.97 eV, respectively (see the figure). The Mg-doped ZnSe crystals were obtained by the method of diffusion in a closed volume containing the initial ZnSe substrate and a charge mixture with a variable Zn and Mg content. Using the charge with Mg leads to the virtually complete disappearance of the *O*-band from the PL spectrum of samples, while annealing in the atmosphere containing only Zn decreases the *O*-band intensity rel-

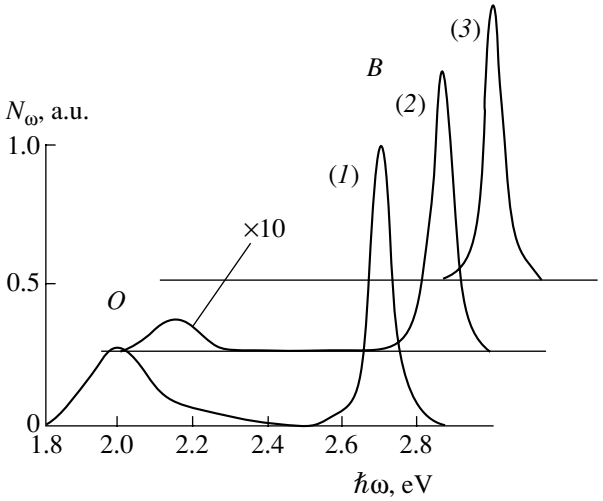

The photoluminescence spectra of ZnSe crystals: (*1*) initial; (*2*, *3*) diffusion-doped with magnesium to the Zn/Mg ratio (*2*) 1 : 0 and (*3*) 0.5 : 0.5 (T = 300 K).

1063-7850/01/2701-0063$21.00

ative to the *B*-band only by one order of magnitude (see the figure).

Study of the shape, intensity, and position of the *B*-band of PL from the doped ZnSe⟨Zn,Mg⟩ crystals depending on the excitation level showed evidence of the exciton character of this emission. Note that this behavior of the *B*-band is retained when the Zn/Mg ratio varies form 90 : 10 to 10 : 90. An increase in the Mg concentration leads to a growth of the edge emission component intensity, while not changing the energy position of the fundamental absorption edge of ZnSe. The latter fact indicates that no solid solutions of the $Mg_xZn_{1-x}Se$ type (at least, with large x) are present in the system.

In concluding, it should be noted that the conductivity of the diffusion-doped ZnSe⟨Zn,Mg⟩ layers increases up to 10^{-1} Ω^{-1} cm^{-1}. The room-temperature activation energy of the electrically active donors is $E_d \approx 0.02$ eV, which correlates with the energy levels of a positive singly-charged selenium vacancy [1]. Thus, the results of our experiments give convincing evidence of the possibility of obtaining diffusion-doped *n*-ZnSe⟨Zn,Mg⟩ layers with a dominating edge emission component.

Acknowledgments. The author is grateful to Prof. V.P. Makhniĭ for valuable remarks and fruitful discussion of the results.

REFERENCES

1. A. N. Georgobiani and M. B. Kotlyarevskiĭ, Izv. Akad. Nauk SSSR, Ser. Fiz. **49** (10), 1916 (1985).
2. *Physics of II–VI Compounds*, Ed. by A. N. Georgobiani and M. K. Sheĭnkman (Nauka, Moscow, 1986).
3. D. D. Nedeoglo and A. V. Simashkevich, *Electrical and Luminescent Properties of Zinc Selenide* (Shtiintsa, Kishinev, 1984).
4. V. K. Bazhenov and V. I. Fistul', Fiz. Tekh. Poluprovodn. (Leningrad) **18** (8), 1345 (1984) [Sov. Phys. Semicond. **18**, 843 (1984)].
5. I. I. Hopfild, D. I. Thomas, and R. T. Lynch, Phys. Rev. Lett. **17** (6), 312 (1966).

Translated by P. Pozdeev

Technical Physics Letters, Vol. 27, No. 1, 2001, pp. 65–66. Translated from Pis'ma v Zhurnal Tekhnicheskoĭ Fiziki, Vol. 27, No. 2, 2001, pp. 51–55.

Thulium Vapor Discharge Step-Tunable Laser

V. A. Gerasimov and L. N. Starkova

Institute of Atmospheric Optics, Siberian Division, Russian Academy of Sciences, Tomsk, 634055 Russia

Received July 12, 2000

Abstract—A thulium vapor discharge tunable laser using transitions between collision-populated upper levels was studied. Five new laser transitions were found in the 1000–1400 nm spectral range. © *2001 MAIK "Nauka/Interperiodica".*

The first communication concerning lasing under the gas discharge conditions in thulium vapors was published in 1968 [1] and reported on twelve laser transitions in the 1300–2380 nm wavelength range. Later [2, 3], the lasing spectrum was expanded so as to extend from 589 to 2384 nm, and the number of operating laser lines was increased to 18.

A special feature of the thulium vapor laser is that the upper levels of all laser transitions except one (589.947 nm) represent nonresonance atomic levels. This circumstance hinders the direct electron-impact population of these levels under the gas discharge conditions. It was suggested [3] and then experimentally confirmed [4] that the main mechanism of the population inversion is the collisional excitation of the upper laser level via nearby ($\Delta E < kT_g$) resonance levels. The resonance transition should be trapped so as to make this resonance level an effective donor.

The collision partners can be represented both by thulium atoms in the ground state and by the buffer (inert) gas atoms. Representing the lanthanoid group of elements, thulium possesses a very rich structure of levels and, accordingly, rather small energy differences between these levels. When the resonance level has several nearby levels not directly excited under the gas discharge conditions, the laser frequency can be discretely switched by using a selective cavity. To our knowledge, this type of switching was previously employed only in CO lasers (see, e.g., [5]).

Figure 1 shows a schematic diagram of the experimental laser setup. The laser tube represents an aluminum oxide gas-discharge channel with a diameter of 20 mm and an active zone length of 400 mm. The tubular niobium electrodes are arranged at the ends of the gas-discharge channel. Pieces of metallic thulium were placed onto the internal surface of the channel and distributed over the entire channel length.

The laser operates in the self-heating regime. A 2.35 nF capacitor is charged to 4.5 kV and connected to the laser tube via a hydrogen-filled thyratron of the TGI1-1000/25 type with a working frequency of 1.4 kHz. Measured by a W–Re thermocouple, the temperature in the gas-discharge channel reached 1100°C at a thulium saturated vapor pressure of P_{Tm} = 1 Torr. The buffer gas is helium at a pressure of P_{He} = 2 Torr.

The selective resonator was based on a diffraction grating (300 lin/mm) with a blaze angle of 30°. The grating was mounted and adjusted so that the first-order beam (k = 1) would be coaxial with the gas-discharge channel. The second-order beam (k = 2) was used for visual monitoring of the lasing with the aid of an electrooptical converter. The dispersion resolution of the grating in the wavelength range studied (for the given resonator configuration) was $\Delta\lambda < 0.1$ nm.

The instrumental broadening of an MDR-23 monochromator used to select the laser radiation in our experiments did not exceed 0.05 nm [6]. The Laser radiation was monitored with a FEU-62 photomultiplier tube (capable of detecting laser radiation in a range of wavelengths up to 2000 nm [7]) and an S1-75 oscillograph.

The experimental procedure was as follows. After attaining the working temperature and detecting the laser radiation by the electrooptical converter, mirror M_2 (forming a flat resonator with mirror M_1) was removed

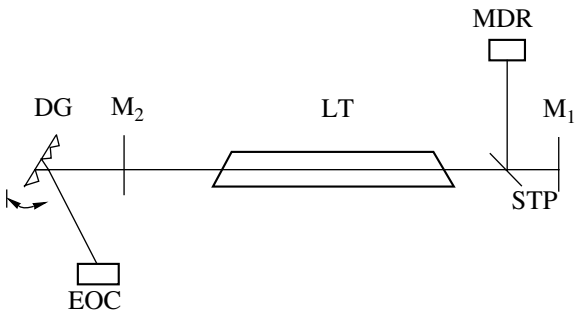

Fig. 1. A schematic diagram of the experimental setup: (LT) laser tube; (M_1) aluminum-coated flat mirror; (STP) semitransparent glass plate; (M_2) dielectric mirror with a reflection coefficient of 20–40% in the 1000–1500 nm wavelength range; (MDR) grating monochromator of the MDR-23 type; (DG) diffraction grating; (EOC) electrooptical converter.

1063-7850/01/2701-0065$21.00 © 2001 MAIK "Nauka/Interperiodica"

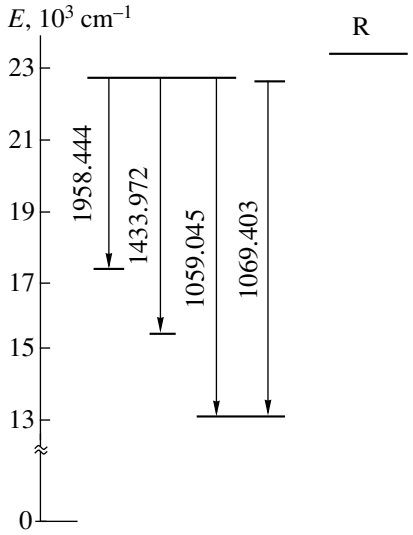

Fig. 2. A schematic diagram of the energy levels involved in the competing laser transitions; R indicates the resonance level (wavelengths of the laser transitions are indicated in nm).

to suspend the lasing, which was restored with the aid of the diffraction grating. Then the grating was rotated, the sequential laser lines were selected by the monochromator, and their wavelengths were determined.

Using this measuring procedure, we have detected ten laser transitions, five of which are reported for the first time. Two of these new transitions (λ = 1059.045 and 1113.11 nm) were identified using the data from [8, 9]. The other three (λ = 1101.0, 1305.4 and 1309.45 nm) remained unidentified.

We should like to note the proximity of the wavelength of the two laser transitions—the known with λ = 1101.115 nm and the newly observed one with λ = 1101.0 nm. The laser line with λ = 1101.0 nm could be separated only provided that the grating had been adjusted so that the second-order beam (k = 2) was coaxial with the laser tube (in which case the grating resolution became two times better).

Among the identified laser transitions, λ = 1113.11 nm is a typical self-confined transition and is not manifested in a usual cavity (with M_1 and M_2 mirrors) as a result of competition for the bottom level with the $25717_{7/2}$–$8771_{5/2}$ transition (λ = 589.95 nm). The transition with λ = 1059.045 nm (Fig. 2) most probably associates the excitation energy for two upper levels with a small energy difference (91 cm^{-1}).

Upon going from simple mirror resonator to the tuned grating scheme, the previously known laser transitions show an approximately tenfold increase in power. It is expected that the use of higher Tm concentrations and the study of other spectral regions corresponding to $\lambda > 1400$ nm and $\lambda < 1000$ nm would markedly increase the number of known lasing transitions in the thulium vapor laser.

Laser transitions determined in this study

λ, nm	Transition, cm^{-1}
1059.045	$22559_{9/2}$–$13119_{11/2}$
1069.403	$22468^{0}_{11/2}$–$13119_{11/2}$
1101.00	–
1101.115	$25536^{0}_{15/2}$–$16456_{17/2}$
1113.11	$17752_{5/2}$–$8771^{0}_{5/2}$
1304.322	$26357_{13/2}$–$18893_{15/2}$
1305.40	–
1309.45	–
1310.057	$22902_{13/2}$–$15271_{15/2}$
1338.009	$22742_{13/2}$–$15271_{15/2}$

REFERENCES

1. Ph. Cahuzac, Phys. Lett. A **27A** (8), 473 (1968).
2. V. A. Gerasimov, V. E. Prokop'ev, V. G. Sokovikov, *et al.*, Kvantovaya Élektron. (Moscow) **11** (3), 624 (1984).
3. V. A. Gerasimov and B. P. Yunzhakov, Kvantovaya Élektron. (Moscow) **16** (12), 2386 (1989).
4. V. A. Gerasimov, Proc. SPIE **3403**, 165 (1998).
5. V. I. Masychev, V. G. Plotnichenko, and V. K. Sysoev, Kvantovaya Élektron. (Moscow) **8** (7), 1540 (1981).
6. M. S. Arteev and S. S. Sulakshin, Prib. Tekh. Éksp., No. 4, 156 (1988).
7. V. M. Klimkin and V. E. Prokop'ev, Prib. Tekh. Éksp., No. 5, 215 (1976).
8. P. Camus, G. Guelachvili, and J. Verges, Spectrochim. Acta B **24**, 373 (1969).
9. J. Sugar and W. F. Meggers, J. Res. Natl. Bur. Stand., Sect. A **77**, 1 (1973).

Translated by P. Pozdeev

Technical Physics Letters, Vol. 27, No. 1, 2001, pp. 67–70. Translated from Pis'ma v Zhurnal Tekhnicheskoĭ Fiziki, Vol. 27, No. 2, 2001, pp. 56–62.

Electromagnetic Waves Generated by Opposite Acoustic Waves

I. A. Kolmakov

Received June 28, 2000

Abstract—An acoustic wave of a combined frequency (formed upon the superposition of the opposite acoustic waves of close frequencies) from a moving source generates electromagnetic waves of the same frequency with the amplitude increasing in the longitudinal direction. The problem is solved for the first time, assuming the absence of electric charges and neglecting the frequency dispersion. It is shown that the running acoustic wave is accompanied by weak electromagnetic waves. This effect may find new applications, in particular, in the space energetic. © *2001 MAIK "Nauka/Interperiodica".*

This study proceeds from the concept of the interrelation and mutual influence of the fields of various natures (types)—electromagnetic and acoustic—and on their common "material base." This concept is used to describe the generation of an electromagnetic wave by a running acoustic wave and the generation of electromagnetic waves with a combined frequency $\omega_c = \omega_1 + \omega_2$ by the opposite acoustic waves with close frequencies ω_1 and ω_2 ($\omega_1 > \omega_2$) in the regime of linear growth with respect to the longitudinal coordinate.

The results of the Fizeau experiments, the effect of light pressure, and some other facts lead to the conclusion of the interrelation and mutual influence between various physical fields, in particular, between the acoustic and electromagnetic fields studied below. Indeed, in the two-field approximation considered here, the "material base" of the electromagnetic field is the same as that of the acoustic field because electrons (as well as the other elementary particles), atoms, molecules, their macroscopic aggregates, etc., are eventually of electromagnetic origin. However, the moving particles constituting the acoustic field possess markedly greater inertial properties compared to those of the electromagnetic "matter," which accounts for a sharp difference between the velocities of propagation of the electromagnetic and acoustic waves.

However, the common "material base" of both types of field unavoidably leads to the motion of one of these fields necessarily involving, to a greater or smaller extent, the other field in that motion as well. From this standpoint, we may conclude that a running acoustic wave, involving the accelerated motion of particles of a medium, must generate electromagnetic waves (although of very small intensity) separating from their acoustic sources and traveling with the speed of light c in the direction of the acoustic wave propagation.

Based on the above general considerations, let us solve the tasks formulated above, assuming the absence of frequency dispersion and free electric charges in the system. In what follows, we will use the notations introduced in [1, 2]. The equations of motion follow from the laws of conservation of the acoustic and electromagnetic fields, $\partial T^{ik}/\partial x^k = 0$. The electromagnetic field is assumed to be linear (Maxwellian), while the acoustic field is described to within the quadratic terms. In the three-dimensional formulation, we obtain

$$\frac{1}{4\pi}\left\{\frac{1}{c}\frac{\partial}{\partial t}[\mathbf{E},\mathbf{H}]_x + \frac{\partial}{\partial x}(E_x^2 + E_y^2) + \frac{\partial}{\partial y}(E_xE_y + H_xH_y)\right.$$
$$\left. + \frac{\partial}{\partial z}(E_xE_z + H_xH_z)\right\} - \frac{\partial W}{\partial x} + \frac{1}{c^2}\left\{\frac{\partial}{\partial t}(wv_x) - \frac{\partial}{\partial x}(wv_x^2)\right.$$
$$\left. - c^2\frac{\partial P}{\partial x} - \frac{\partial}{\partial y}(wv_xv_y) - \frac{\partial}{\partial z}(wv_xv_z)\right\} = 0;$$

$$\frac{1}{4\pi}\left\{\frac{1}{c}\frac{\partial}{\partial t}[\mathbf{E},\mathbf{H}]_x + \frac{\partial}{\partial x}(E_xE_y + H_xH_y) + \frac{\partial}{\partial y}(E_y^2 + H_y^2)\right.$$
$$\left. + \frac{\partial}{\partial z}(E_yE_z + H_yH_z)\right\} - \frac{\partial W}{\partial y} + \frac{1}{c^2}\left\{\frac{\partial}{\partial t}(wv_y) - \frac{\partial}{\partial x}(wv_xv_y)\right. \quad (1)$$
$$\left. - \frac{\partial}{\partial y}(wv_y^2) - c^2\frac{\partial P}{\partial y} - \frac{\partial}{\partial z}(wv_yv_z)\right\} = 0;$$

$$\frac{1}{4\pi}\left\{\frac{1}{c}\frac{\partial}{\partial t}[\mathbf{E},\mathbf{H}]_z + \frac{\partial}{\partial x}(E_xE_z + H_xH_z) + \frac{\partial}{\partial y}(E_yE_z + H_yH_z)\right.$$
$$\left. + \frac{\partial}{\partial z}(E_z^2 + H_z^2)\right\} - \frac{\partial W}{\partial z} + \frac{1}{c^2}\left\{\frac{\partial}{\partial t}(wv_z) - \frac{\partial}{\partial x}(wv_xv_z)\right.$$

$$-\frac{\partial}{\partial y}(wv_y v_z)-\frac{\partial}{\partial z}(wv_2^2)-c^2\frac{\partial P}{\partial z}\Bigg\} = 0;$$

$$\frac{\partial W}{\partial t}-\mathrm{div}\mathbf{S}+\left\{\frac{\partial e}{\partial t}-\mathrm{div}(w\mathbf{v})\right\} = 0,$$

where w is the enthalpy per unit volume, e is the internal energy density, and P is the pressure.

For simplicity, we will restrict the consideration to flat waves. The acoustic waves with the frequency ω_1 (or the waves from a source of the combined frequency $\omega_c = \omega_1 + \omega_2$ formed upon the superposition of two opposite waves with the frequencies ω_1 and ω_2) propagate along the x-axis of a Cartesian coordinate system (the wavevectors of the primary sound waves $\mathbf{k}_1 \uparrow\downarrow \mathbf{k}_2$ and of the combined source $\mathbf{k}_c \uparrow\uparrow \mathbf{k}_1 \uparrow\uparrow \mathbf{x}$, as well as the acoustic and electromagnetic waves with the frequency ω_c generated by the source also propagate along the x-axis). The second approximation applied to Eqs. (1) leads to the following expressions:

$$\frac{1}{c}\left\{\frac{\partial e''}{\partial t}-\frac{\partial}{\partial x}(wv_x'')\right\}+\frac{\partial W''}{\partial t}$$

$$-\frac{1}{4\pi}\frac{\partial}{\partial x}(E_z'H_y'-E_y'H_z') = 0;$$

$$w = e + P; \qquad (2)$$

$$\frac{1}{c^2}\left\{\frac{\partial}{\partial t}(wv_x'')-\frac{1}{2}\frac{\partial v_x'^2}{\partial x}\right\}-\frac{\partial P''}{\partial x}$$

$$+\frac{1}{4\pi}\left\{\frac{1}{c^2}\frac{\partial}{\partial t}(E_z'H_y'-E_y'H_z')-4\pi\frac{\partial W''}{\partial x}\right\} = 0.$$

Equations (2) are reduced to the wave equation for simultaneously excited acoustic P'' and electromagnetic waves with the energy density W'':

$$\left(\frac{\partial^2 P''}{\partial t^2}-c_{ac}^2\frac{\partial^2 P''}{\partial x^2}\right)+\frac{c_{ac}^2}{c^2}\left(\frac{\partial^2 W''}{\partial t^2}-c^2\frac{\partial^2 W''}{\partial x^2}\right)$$
$$= \frac{\rho_0 c_{ac}^2}{2}\frac{\partial^2}{\partial x^2}(v_x'^2), \qquad (3)$$

where $c_{ac} = \sqrt{(\partial P/\partial\rho)_s}$ is the velocity of sound in the given medium.

The running harmonic waves described by Eq. (3) may exhibit "interactions" (this means that the motions of the acoustic and electromagnetic fields are interrelated: the motion of one field induces the motion of another and vice versa, see above) depending on the phase factors characterizing these waves. For example, the source in Eq. (3) is characterized by the phase factor $\exp[i(\omega_c t - k_\Omega x)]$, where $k_\Omega = \omega_\Omega c_{ac}^{-1} = \omega_c V_c^{-1}$, $\omega_\Omega = \omega_1 - \omega_2$, and V_c is the velocity of the acoustic source with the frequency ω_c. The source generates the electromagnetic waves $\exp[i(\omega_c t - k_c x)]$ (with $k_c = \omega_c c^{-1}$) and the acoustic waves $\exp[i(\omega_c t - k_c^{ac} x)]$ ($k_c^{ac} = \omega_c c_{ac}^{-1}$).

These phase relationships indicate that the synchronous interactions are possible only between the source and the electromagnetic waves, because the source velocity V_c may, in principle, acquire infinitely large values (in particular, close or equal to the speed of light [3, 4]). Note that such superfast energy fluxes may be created in the paraxial region of conic waves [5] formed by the high-intensity shock waves, that is, in the relativistic variant of this problem (see below).

Therefore, for the acoustic wave velocity on the order of c ($V_c \sim c$), the acoustic wave is virtually not generated, while the electromagnetic wave may grow linearly along the coordinate x (the acoustic source with the velocity V_c generates a weak electromagnetic wave at each point on its path, in phase with the running electromagnetic waves). Indeed, a solution to Eq. (3), even assuming that all energy of the source is spent for the sound excitation (i.e., for $W'' = 0$), yields

$$P'' = \rho\frac{c_{ac}^2}{V_c^2}|v_{12}'(0)|\sin\left(\frac{x}{2}k_c^{ac}\right)\sin\left(\omega_c t-\frac{x}{2}k_c^{ac}\right), \qquad (4)$$

where $|v_{12}'(0)| = |v_1'(0)||v_2'(0)|$ are the amplitudes of waves with the frequencies ω_c, ω_1, and ω_2 at the entrance of the interaction region ($X = 0$).

Equation (4) shows that for $V_c \sim c$ the value $P'' \sim c_{ac}^2 V_c^{-2}$ is negligibly small, which means that such sources generate sound. Therefore, the acoustic field can be excluded from Eq. (3) in considering the problem of the electromagnetic wave generation by a fast acoustic source. In this approximation, a solution to Eq. (3) taking into account the boundary conditions ($x = 0$, $W'' = 0$; $|v_{12}'(x)| = |v_{12}'(0)|$) and assuming a small mismatch between the wave velocities $\pm\Delta c = c - V_c$, has the following form:

$$W'' = \frac{\rho}{2}\frac{c}{V_c}\frac{|V_{12}'(0)|}{(1+cV_c^{-1})}k_\Omega x$$

$$\times\left\{\left\{\frac{\sin\left[\frac{x}{2}k_c(1-cV_c^{-1})\right]}{\left[\frac{x}{2}k_c(1-cV_c^{-1})\right]}\right\}\sin\left[\omega_c t-\frac{x}{2}k_c(1+cV_c^{-1})\right]\right. \qquad (5)$$

$$+\frac{\Delta c}{c}\frac{\cos(\omega_c t - k_\Omega x)}{(1 - cV_c^{-1})}\tan(\omega_c t - k_c x)\Bigg\}.$$

Under the synchronism conditions (here $V_c = c$), Eq. (5) yields

$$W'' = \frac{\rho}{2}|v'_{12}(0)|k_\Omega x \sin(\omega_c t - k_\Omega x), \quad (6)$$

which implies that the electromagnetic field amplitude grows infinitely with the coordinate x and, for sufficiently large x and the primary acoustic wave amplitude, may become very large.

Now let us consider the problem of an electromagnetic field accompanying the running acoustic wave and determine the ratio of their energies. This will be done using Eq. (2), but written in the first approximation (without linearities). Assuming that the amplitudes of the acoustic $|P'(x)|$ and electromagnetic $|W(x)|$ waves are slowly varying functions (neglecting the second derivatives of the amplitudes), we obtain from Eq. (2)

$$\frac{\partial|P'|}{\partial x} + 2k^*_{ac}|P'|\cot(k^*_{ac}x) = -2R^2\frac{k^*_{ac}}{\sin(k^*_{ac}x)}|\tilde{W}'|, \quad (7)$$

$$\frac{\partial|\tilde{W}'|}{\partial x} + 2k|\tilde{W}'|\cot(k^*_{ac}x) = 2\frac{k}{\sin(k^*_{ac}x)}|P'|, \quad (8)$$

where $R = c_{ac}c^{-1}$; $k^*_{ac} = k_{ac}(1 - c_{ac}c^{-1}) \approx k_{ac}$; $k_{ac} = \omega/c_{ac}$; and $k = \omega/c$. The term $|\tilde{W}'| = R^2|W'|$ determines the fraction of the electromagnetic field in the total energy balance under the conditions of coexistence of the acoustic and electromagnetic fields; $|W'|$ is the electromagnetic field density in the absence of sound (this value is determined from an expression for the action S of the electromagnetic field alone).

The solutions to Eqs. (7) and (8), with the additional conditions for the amplitudes $|P'| + |\tilde{W}'| = \text{const}$ and the boundary conditions ($x = 0$, $|P'| = |P'(0)|$; $|\tilde{W}'| = 0$), are given by the expressions

$$|P'| \approx |P'(0)|\Bigg\{1 - 2\sin\left(\frac{x}{2}k_{ac}\right) \times\left[1 - \frac{1}{2}\sin\left(\frac{x}{2}k_{ac}\right)\right]\Bigg\}\cos^{-1}\left(\frac{x}{2}k_{ac}\right), \quad (9)$$

$$|\tilde{W}'| \approx 2R|P'(0)|\tan\left(\frac{x}{2}k_{ac}\right). \quad (10)$$

Using Eqs. (9) and (10), the ratio of amplitudes of the acoustic and electromagnetic fields is

$$\frac{|P'|}{|\tilde{W}'|} \approx \frac{c}{c_{ac}}\cot\left(\frac{x}{2}k_{ac}\right) \sim R^{-1},$$
$$\frac{|E'_{ac}|}{|\tilde{W}'|} = \frac{v'}{c_{ac}}R^{-1}\cot\left(\frac{x}{2}k_{ac}\right), \quad (11)$$

where E'_{ac} and v' are the energy and the variational velocity of the acoustic wave.

Thus, according to Eqs. (9)–(11), the excitation of sound at the entrance of the wave region (boundary condition $X = 0$, see above) is accompanied by the simultaneous generation of electromagnetic waves with a very small amplitude $|\tilde{W}'|$ as compared to that of the acoustic waves $|P'|$ ($\sim R$). Because the R value is very small (for water, $R \sim 10^{-5}$), detection of the electromagnetic waves generated by the running acoustic waves by means of direct measurements may be difficult. However, this detection is facilitated in the case of the waves of a combined frequency considered above. As for the media obeying the relativistic equation of state, the sound velocity in this case is $\tilde{c}_{ac} = c/\sqrt{3}$ (see, e.g., [2]) and the R value can be large ($R = 1/\sqrt{3}$): in these media, a considerable proportion of the acoustic energy may transform to the electromagnetic wave energy.

In the ultrarelativistic case (high-intensity shock waves), the sound velocity may approach c, and R may tend to unity; however, the exact phase matching between the electromagnetic and acoustic waves (but not the waves with the combined frequency) in this case is not attained. We may also note that, as the source velocity V_c grows, an increasing "weight" in the energy flux belongs to the electromagnetic component; in the limit of $V_c = c$, the source apparently fully degenerates to the electromagnetic source. In terms of the quantum electrodynamics, this situation can be interpreted as the appearance of virtual phonons with a frequency ω_c and the velocity $V_c \sim c$ upon the collision of two opposing phonons with the frequencies ω_1 and ω_2. However, the phonons having such superhigh velocities become unstable and rapidly disappear, with the simultaneous production of photons with the frequency ω_c.

In concluding, it must be noted that the experimental verification of the phenomenon considered in this study could stimulate the investigations of unknown fields and numerous (principally new) applications of these effects (one possible application is space energetics, where an important problem consists in pumping energy from the distant cosmos to the Earth, with the energy being converted into electromagnetic or other forms).

Another aspect of this problem is that the simple concept on which the above analysis is based allows us to explain some widely employed but still unclear principles. An example is offered by the principle of super-

position, according to which the opposite waves of small amplitude pass through one another without distortions, as if they do not "see" each other. Another task is to explain the meaning of "infinitely large phase velocity" employed, for example, in acoustics, etc.

REFERENCES

1. L. D. Landau and E. M. Lifshitz, *The Classical Theory of Fields* (Nauka, Moscow, 1988; Pergamon, Oxford, 1975).
2. L. D. Landau and E. M. Lifshitz, *Fluid Mechanics* (Nauka, Moscow, 1988; Pergamon, New York, 1987).
3. I. A. Kolmakov and N. N. Antonov, Fiz. Plazmy **18** (10), 1372 (1992) [Sov. J. Plasma Phys. **18**, 708 (1992)].
4. I. A. Kolmakov, Zh. Tekh. Fiz. **66** (2), 201 (1996) [Tech. Phys. **41**, 225 (1996)].
5. I. A. Kolmakov, Pis'ma Zh. Tekh. Fiz. **25** (9), 35 (1999) [Tech. Phys. Lett. **25**, 354 (1999)].

Translated by P. Pozdeev

Technical Physics Letters, Vol. 27, No. 1, 2001, pp. 71–73. Translated from Pis'ma v Zhurnal Tekhnicheskoĭ Fiziki, Vol. 27, No. 2, 2001, pp. 63–69.

The Effect of MHD Interactions on the Input Shock Waves in a Supersonic Diffuser

S. V. Bobashev*, R. V. Vasil'eva*, E. A. D'yakonova*, A. V. Erofeev*, T. A. Lapushkina*, V. G. Maslennikov*, S. A. Ponyaev*, V. A. Sakharov*, and D. van Wie**

** Ioffe Physicotechnical Institute, Russian Academy of Sciences, St. Petersburg, 194021 Russia*

*** Johns Hopkins University, Laurel, Maryland, USA*

Received September 14, 2000

Abstract—The interaction with an external magnetic field modifies the variation of the shock wave configuration in a pure inert gas plasma at the entrance of a supersonic diffuser. The phenomenon was studied using an experimental setup based on a shock tube with a flat nozzle and the model supersonic diffuser. The experiments were conducted in krypton, for the shock wave Mach number in the shock tube $M = 7.8$ and the Mach number at the nozzle exit $M = 4.2$. The gasodynamic discontinuities and their structural variations induced by the magnetic induction changes were by visualized by the schlieren method and by photography of the intrinsic emission accompanying the process. Three regions of the MHD interaction affecting the shock wave configuration in the gas flow were revealed. © *2001 MAIK "Nauka/Interperiodica".*

In recent years, a considerable effort has been devoted to the study of interactions between supersonic flows in an inert gas and magnetic fields. These investigations were aimed at establishing the possibility of using these magnetohydrodynamic (MHD) interactions for the development of aircraft of a new generation [1, 2].

In this work, we have studied the effect of an external magnetic field on the oblique shock waves formed at the entrance of a supersonic diffuser with complete internal recompression of a low-temperature inert gas plasma flow. The experimental data were compared with the results of accompanying theoretical investigations [3, 4].

The use of an inert gas as the working fluid is explained by the possibility of using preionization at the entrance of the gasodynamic tract. Inert gases, characterized by a relatively slow three-particle recombination process [5], are capable of retaining the initial shock wave ionization level throughout the channel. This ionization level may be sufficient to provide for a significant MHD interaction. Evidently, the experiments using air as the working fluid would be the most interesting from the practical standpoint. Unfortunately, a decay of the initial ionization state in air (proceeded by a mechanism of the dissociative recombination of molecular ions formed upon ionization [6]) is several orders of magnitude faster than in inert gases. Another effective mechanism, leading to the loss of electrons from the air plasma, is the electron sticking to oxygen molecules. For these reasons, the experiments in air would require the working fluid to be continuously ionized throughout the MHD channel volume. Solving this task presently encounters considerable difficulties.

The model experiments in inert gases allow important general features of the MHD interactions to be established, which are determined by the main similitude criteria, including the Mach number, the Stewart parameter, and the Hall parameter.

The experimental setup used in our experiments consists of a shock tube, providing high stopping parameters and creating a high degree of ionization, a flat accelerating nozzle (separated from the shock tube by a thin diaphragm), and a model supersonic diffuser. Figure 1 shows a schematic diagram of the experimental MHD unit, comprising an accelerating nozzle and a diffuser with complete flow recompression, provided with the necessary control and monitoring electrodes. The nozzle and diffuser are mounted in a vacuum chamber connected to a ballast volume. A pulsed magnetic field with a strength of up to 1.5 T was created by the discharge of a capacitor bank through a Helmholtz coil. The experimental setup was described in more detail elsewhere [7, 8].

The experiments were conducted in Kr with a shock wave front Mach number in the shock tube $M = 7.8$ and an initial gas pressure of 20 torr in the low-pressure chamber. The flow deceleration parameters in the shock tube, calculated within the approximation of complete thermodynamic equilibrium, are given below by the quantities with the subscript "5" as temperature $T_5 = 9800$ K; degree of ionization, $\alpha_5 = 0.025$; plasma conductivity, $\sigma_5 = 3200$ S/m; gas density $\rho_5 = 1.08$ kg/m^3, particle concentration (number density) $n_5 = 7.75 \times 10^{24}$ m^{-3}. The distribution of flow parameters in the nozzle was calculated within a two-temperature plasma model with inhomogeneous ionization. The plasma parameters at the nozzle exit (in front of the diffuser

1063-7850/01/2701-0071$21.00

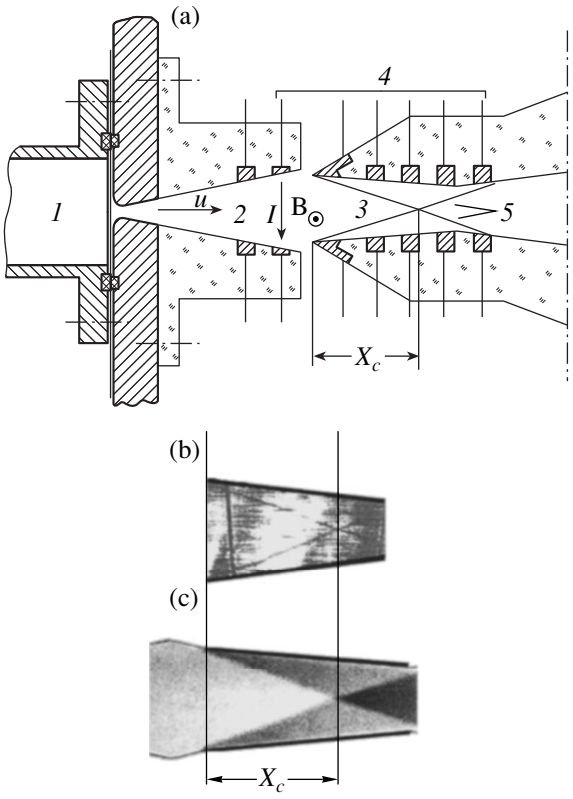

Fig. 1. Schematic diagrams of an MHD setup and shock wave configurations: (a) model unit scheme showing (*1*) shock tube, (*2*) accelerating nozzle, (*3*) diffuser, (*4*) electrodes connected to loads and (*5*) shock waves; (b) schlieren photograph; (c) calculated density field.

entrance) are as follows: gas temperature $T_0 = 1550$ K; flow velocity, $u_0 = 2.1 \times 10^3$ m/s; $\sigma_0 = 580$ S/m; $\rho_0 = 0.0645$ kg/m^3, $n_0 = 4.6 \times 10^{23}$ m^{-3}. The Mach number at the nozzle exit was $M_0 = 4.2$.

The flow structure was visualized by two methods. The first method consisted in using the schlieren system employing an OGM-20 ruby laser as the light source. This method gave a single schlieren pattern with a 30-ns exposure during the efflux time. The second method was based on the registration of the intrinsic optical emission from plasma. The intensity of this emission, related to the recombination continuum, is determined by the square electron concentration. At the sites of the gasodynamic discontinuity, the electron concentration changes by the same factor as the atomic concentration. For this reason, the regions of large emission intensity gradients are close to the regions of density gradient, which is confirmed by the comparison of the gasodynamic structure patterns provided by the schlieren method and by the gas emission photography. The time variations of the gasodynamic structures were followed by a high-speed camera capable of making 130 shots at a 1.5 μs exposure during the process. The experiments performed in the absence of the external magnetic field ($B = 0$) showed that a nonstationary stage of the gas efflux from the nozzle lasts for approximately 100 μs, while a quasi-stationary stage duration is abut 400 μs.

The MHD channel was operated in the Faraday cup regime with sectionated electrodes used to measure the current–voltage characteristics. The results of these measurements showed that the magnetic-field induced electrode potential drop is comparable with the induced emf. For this reason, the electric currents in the plasma were several orders of magnitude lower than expected. In order to compensate for the electrode potential drop and provide a current value sufficient for significant MHD interactions, an additional electric potential V_{LC} (formed by a special long line) was applied to the electrodes. In this case, the Ohm law for the circuit can be written as $V_{LC} + uBh = IR_{\text{in}} + IR_L$, where B is the magnetic induction, h is the interelectrode gap, I is the current strength, R_{in} is the internal resistance of the generator, and R_L is the load resistance. The results of electric measurements showed that the current density due to the combined action of the external and magnetic-field-induced emf is about 40 A/cm^2.

Thus, the pattern of flow is formed under the action of two factors: the magnetic field and the heat supplied from outside. Both these factors act in the same direction, retarding the supersonic flow and accelerating the subsonic flow. Estimates show that, under the experimental conditions studied, the ponderomotive force is dominating.

Figure 1a shows a schematic diagram of the diffuser geometry and the input shock configuration. The main geometric characteristics of the units are as follows: apex angle of the nozzle, 22°; supersonic nozzle length, 81 mm; output cross section, 37 × 38 mm; diffuser input cross section, 32 × 38 mm; diffuser side wall inclination angle relative to horizontal direction, –5.5°. Also indicated in Fig. 1a are the two inclined intersecting shock waves formed when the gas flow with $M_0 = 4$ moves through the diffuser.

Figure 1b shows the oblique shock waves visualized by the schlieren method at $B = 0$. Figure 1c presents the gas density distribution calculated [3] for the same conditions as those used in the experiment. The characteristic parameter is represented by the distance X_c from the diffuser entrance to the point of the shock wave intersection. As the magnetic field strength (and, hence, the MHD interaction intensity) increases, the flow pattern exhibits certain variations. Using the data obtained by the schlieren method and the high-speed photography of the plasma emission, it is possible to reveal and measure characteristic changes in the input shock configuration depending on the applied magnetic field strength. For a relatively weak field, the MHD interaction exhibits a quasi-stationary stage, in which the shock wave intersection point approaches the MHD channel entrance with increasing magnetic field strength. As the magnetic induction level increases, the flow character changes: the flow becomes nonstation-

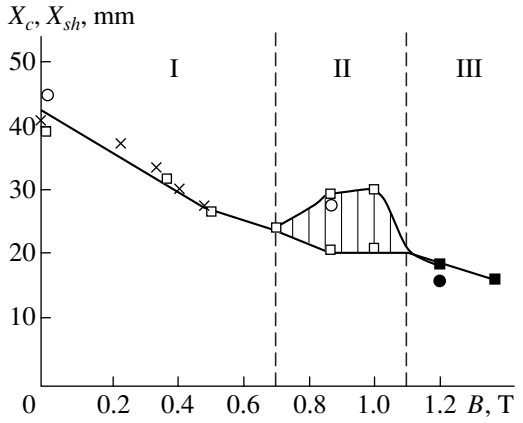

Fig. 2. Variation of the positions of the oblique shock wave intersection point X_c (open symbols) and the MHD deceleration shock point X_{sh} (black symbols) depending on the magnetic field strength: (open circles) data obtained by the schlieren method; (squares) high-speed photography of intrinsic emission; (crosses) calculated values. Cross-hatched region shows the interval of X_c variation with time. Roe numerals show the intervals of (I) weak, (II) transient unstable, and (III) strong MHD interactions.

ary and the point of the shock wave intersection shifts with time. A further increase in the magnetic field strength leads to the appearance of a direct MHD deceleration shock wave standing on two points at the channel walls and changing its position only slightly with time. A characteristic system parameter in this case is the distance X_{sh} from this shock to the diffuser entrance.

Figure 2 demonstrates the variation of the point of intersection X_c of the input shocks and the MHD deceleration shock X_{sh} depending on the magnetic field strength. As seen from this pattern, we may distinguish three types of MHD interactions in the system studied: weak, transient (unstable), and strong. The weak MHD interaction, occurring (for the gasodynamic regime studied) in the interval $0 < B < 0.7$ T, is characterized by a stable flow pattern: the inclination angle of the oblique shock waves increases with the magnetic field, the shock wave intersection point approaches the channel entrance, and the input shocks are followed by a system, of reflected oblique shock waves. The flow remains supersonic over the entire diffuser region.

During the transient unstable MHD interaction ($0.7 < B < 1.1$ T), the point of the shock wave intersection shifts with time both along the flow and in the transverse direction. The X_c may vary by 20% (Fig. 2) within a time period on the order of 10 μs. Behind the input shocks, the flow exhibits a complicated structure varying with time. Apparently, the flow instability in this regime is related to the formation of local subsonic waves. The time-averaged X_c value decreases with increasing magnetic induction and the shock wave intersection point approaches the diffuser entrance.

A strong MHD interaction ($B > 1.1$ T) is characterized by a strong change in the flow structure with the formation of a direct MD deceleration shock at the diffuser entrance, which transforms the flow in the diffuser from a supersonic to a subsonic regime. As the magnetic induction grows, the shock wave intersection point X_{sh} shifts toward the diffuser entrance. We may predict that, with a further increase in the magnetic field strength, the MHD deceleration shock will go out of the diffuser and move in the nozzle in the direction opposite to the flow direction.

Thus, we have demonstrated the effect of the MHD-induced flow deceleration on the shock wave configuration in a supersonic diffuser and established that there are three possible types of the MHD interaction in such systems: weak, transient (unstable), and strong.

Acknowledgments. The work was supported by the Russian Foundation for Basic Research, project no. 98-01-01121a.

REFERENCES

1. E. P. Gurijanov and P. T. Harada, AIAA Pap. **96-4609** (1996), in *Proceedings of the 7th Aerospace Planes and Hypersonic Technology Conference, Norfolk, 1996.*
2. D. I. Brichkin, A. L. Kuranov, and E. G. Sheikin, AIAA Pap. **98-1642** (1998), in *Proceedings of the 8th International Space Planes and Hypersonic Systems and Technologies Conference, Norfolk, 1998.*
3. Yu. P. Golovachev and S. Yu. Sushchikh, Zh. Tekh. Fiz. **70** (2), 28 (2000) [Tech. Phys. **45**, 168 (2000)].
4. Yu. P. Golovachev, S. Yu. Sushchikh, and David van Wie, AIAA Pap. **2000-2666** (2000).
5. L. M. Biberman, V. S. Vorob'ev, and I. T. Yakubov, *Kinetics of Nonequilibrium Low-Temperature Plasmas* (Nauka, Moscow, 1982; Consultants Bureau, New York, 1987).
6. Yu. P. Raĭzer, *The Physics of Gas Discharge* (Nauka, Moscow, 1987).
7. S. V. Bobashev, E. A. D'yakonova, A. V. Erofeev, *et al.*, in *Proceeding of International Conference on MHD Power Generation and High Temperature Technologies, Beijing, 1999*, p. 581.
8. S. V. Bobashev, E. A. D'yakonova, A. V. Erofeev, *et al.*, AIAA Pap. **2000-2647** (2000).

Translated by P. Pozdeev

Technical Physics Letters, Vol. 27, No. 1, 2001, pp. 74–76. Translated from Pis'ma v Zhurnal Tekhnicheskoĭ Fiziki, Vol. 27, No. 2, 2001, pp. 70–75.

Liquid-Crystalline Polarization Converter

O. A. Kapustina and N. A. Kolesnikova

Andreev Acoustics Institute, State Scientific Center of the Russian Federation, Moscow, 117036 Russia

Received April 18, 2000

Abstract—A new concept of the polarization converter based on a nematic liquid crystal is proposed for application in an acoustic imaging system. © *2001 MAIK "Nauka/Interperiodica".*

An image receiver is the integral part of any acoustic visualization system. The first receiver, implementing a sensor element based on a thin nematic liquid crystal (NLC) layer, was developed in the 1970s [1]. This device performed the direct acoustic to optical image conversion by changing the polarization of light transmitted through the receiver as a result of the acoustic-wave- induced reorientation of the ensemble of NLC molecules. However, subsequent investigations showed that this polarization image converter (PIC) possesses a very low sensitivity [2]. Among alternative ideas [3–6] proposed later for the PIC development, the most attractive consists in introducing an additional coherent perturbation into the NLC layer in order to increase the efficiency of the acoustic flow production that determines the mechanism of the orientational effect of the acoustic waves upon NLC molecules.

In this paper, we present a new PIC functioning concept and illustrate it by an example of visualization of a longitudinal acoustic wave field. The main idea consists in simultaneously "recording" in the NLC layer a system of two coherent waves with the intensities $\mathcal{I}_l$ (longitudinal wave) and $\mathcal{I}_s$ (shear wave), equal frequencies, and mutually perpendicular polarizations.

Figures 1a and 1b show a schematic diagram of the PIC device and a simplified visualization system used to test the idea. In the PIC, plate *1* and a shear wave emitter plate *2* make a flat cell filled with an NLC layer. Plate *2* is oriented so that the direction of the shear wave oscillations coincides with the *x*-axis. Spacers *3* placed at the edges of the NLC layer determine the cell thickness *d*, while the edges parallel to the *y*-axis are open. The NLC molecules in layer *4* possess a homeotropic orientation. A thin adhesive (salol) layer couples the PIC to the sound waveguide *5*. The longitudinal wave emitter plate *6* is mounted at the edge of waveguide *5* as depicted in the scheme. Emitter plates *2* and *6* are excited from the same generator. The acoustic wave intensity was monitored by measuring the voltage supplied to the emitters.

Variations in the NLC orientation state and the optical measurements in the PIC tested were visually monitored with the aid of a system based on a polarization microscope operated in a reflection mode. A beam of light with the intensity I_0 passed the input polarizer and the NLC layer of PIC and, upon reflection from a mirror coating *11* on plate *2*, passed through the analyzer and entered a photodiode detector to be converted into an electric signal measured with a voltmeter.

Figures 1c and 1d show fragments of an image of the field of emitter *6* in the NLC layer observed in the two- and single-wave visualization modes. The micrographs represent the patterns obtained in the region of the NLC layer between open boundary *7* and the center. Figure 2a shows a family of plots of the relative intensity I/I_0 of the light transmitted through the NLC layer and the analyzer versus intensity $\mathcal{I}_l$ of the longitudinal acoustic waves for the shear wave intensities $\mathcal{I}_s$ = 0, 0.1, 0.3, 0.7, and 1.3 W/cm^3 (curves *1–5*, respectively), where I_0 and I are the intensities of the light flux incident on the NLC and the photodiode, respectively.

The experimental data indicate that, irrespective of the visualization mode, the transmitted light intensity obeys a relationship $I/I_0 \sim \mathcal{I}_l^n$; on the passage from single- to two-wave visualization mode, the exponent n changes from 4 to 2. The optical response of PIC to the variation of $\mathcal{I}_l$ and $\mathcal{I}_s$ in the two-wave mode determines a relationship of the type $I/I_0 \sim \mathcal{I}_l^2\mathcal{I}_s^2$ (Fig. 2b), while the sensitivity with respect to the longitudinal wave intensity $\mathcal{I}_{0l}$ depends on the shear wave intensity: $\mathcal{I}_{0l} \sim 1/\mathcal{I}_s$. We took a $\mathcal{I}_{0l}$ value equal to the $\mathcal{I}_l$ value for which the NLC layer transmission is I/I_0 = 0.01. It is important to note that, as $\mathcal{I}_s$ increases from 0 to 1.3 W/cm^2, the $\mathcal{I}_{0l}$ (at the frequency employed) decreases to less than 1/10 of the initial level.

The above relationships can be interpreted within the framework of a model [6] describing the optical response of NLC to the wave field formed in a layer of thickness *d* as a result of the interaction between longi-

1063-7850/01/2701-0074$21.00

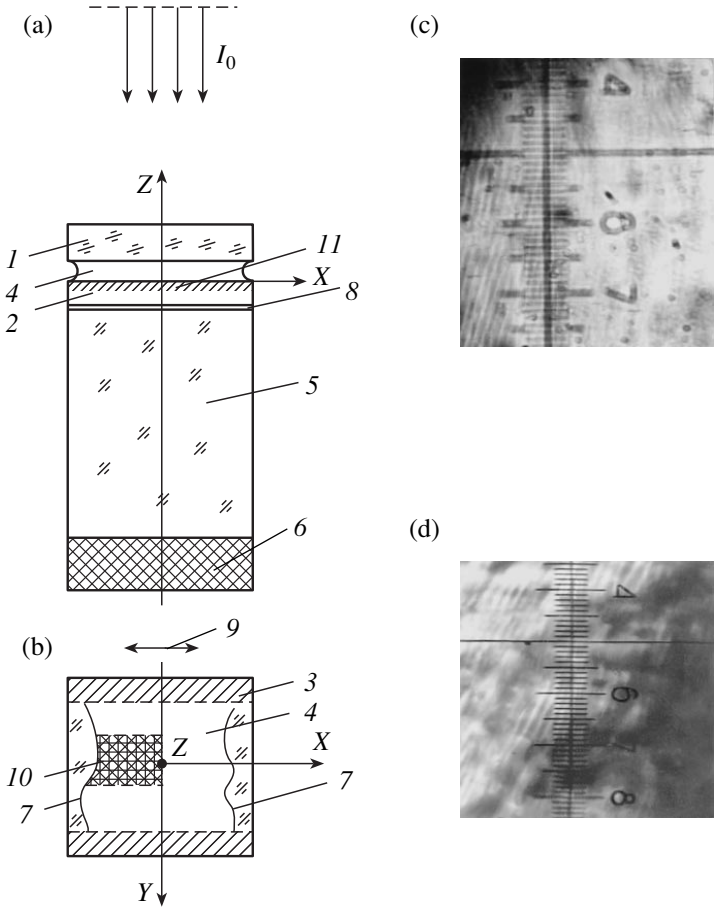

Fig. 1. Schematic diagrams showing a PIC structure in the (a) side and (b) top view and (c, d) the test results: (*1*) flat glass plate; (*2*) shear wave emitter plate (*Y*-cut quartz, intrinsic frequency 16.869 MHz); (*3*) spacers; (*4*) NLC layer (MBBA–EBBA eutectic mixture); (*5*) glass waveguide rod; (*6*) longitudinal wave emitter plate (71°-cut quartz, intrinsic frequency 16.878 MHz); (*7*) open boundaries of the NLC layer in the PIC cell; (*8*) adhesive (salol) layer; (*9*) direction of the shear wave oscillations; (*10*) imaged region of the NLC layer; (*11*) mirror coating. Micrographs (c) and (d) show the fragments of optical images of the acoustic field generated by emitter *6* visualized by PIC operated in the (c) two-wave and (b) single-wave modes in region *10* of the NLC layer indicated by cross hatching in Fig. 1b (crossed polaroids; NLC layer thickness 100 μm).

tudinal and shear oscillations in the frequency range where the wavelengths of the elastic λ_l and viscous λ_v waves obey a relationship $\lambda_l \ll \lambda_v$, where $\lambda_v \ll d$.

Implementation of the aforementioned model to the PIC test conditions employed yields the relationship $I/I_0 = \text{const}\mathcal{I}_l^2\mathcal{I}_s^2$, which agrees with the experimental results. For d = 100 μm and a frequency of ~16 MHz, the calculation leads to the following ratio of the selective sensitivities of the PIC with respect to the longitudinal $\mathcal{I}_{0l}$ and shear $\mathcal{I}_{0s}$ oscillations: $\mathcal{I}_{0l}\mathcal{I}_{0s}\sin^2(\pi/4 - \theta) = 2.84$ [mW/cm^2]^2. Here, θ is the phaseshift of these oscillations at the NLC–plate *2* boundary in the PIC. Under the given PIC test conditions, θ = 0.94 rad. This yields $\mathcal{I}_{0l}\mathcal{I}_{0s} = 1.15$ (mW/cm^2)^2, which is close to the experimental value. Thus, the model of Anikeev *et al.* [6] describes the main characteristics of PIC under the two-wave visualization conditions and can be used for the optical image analysis.

As was noted in [7] for the single-wave action upon an NLC layer, the layer compression in a longitudinal weave field leads to periodic motions of the open boundaries and the excitation of secondary waves. The interaction of these waves with the initial longitudinal wave gives rise to the acoustic flows on a $\lambda_l/2$ scale capable of rotating the NLC molecules. The secondary waves propagate from the open boundaries toward the center of the NLC layer and decay at a distance of ~$20\lambda_l$, so that the acoustic flows are developed only within a certain zone at the open boundaries. For this reason, a band structure with a period determined by the acoustic flow scale is observed in this boundary region. In the central part of the NLC layer, not reached by the secondary waves, the NLC molecules retain their initial homeotropic orientation (Fig. 1d).

The flow mechanism outlined above is also operative in the case of a two-wave visualization mode. However, in this case, a coherent viscous wave generated in

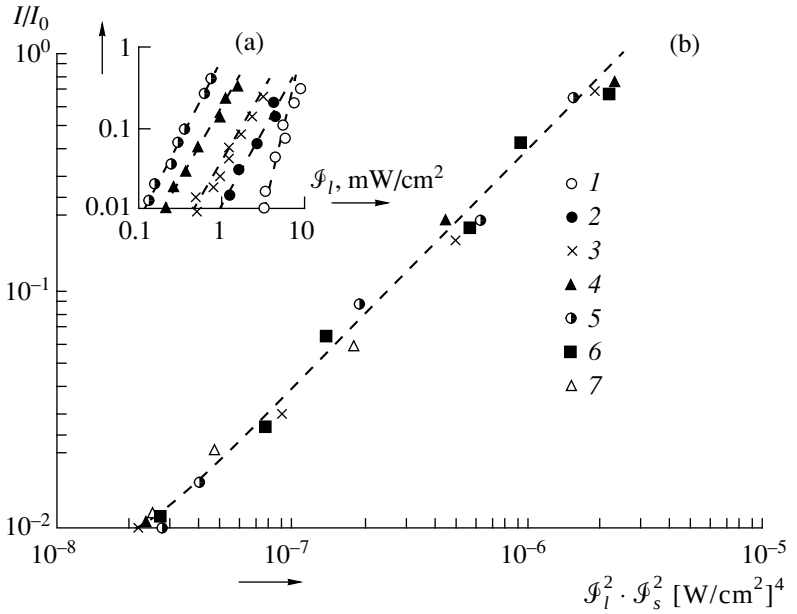

Fig. 2. The main characteristics of 100-μm-thick NLC-based PIC: (a) plots of the relative intensity I/I_0 of the light transmitted through the NLC layer and the analyzer versus intensity $\mathcal{I}_l$ of the longitudinal acoustic waves for the shear wave intensities $\mathcal{I}_s$ = 0 (*1*), 0.1 (*2*), 0.3 (*3*), 0.7 (*4*), 1.3 W/cm^3 (*5*) (crossed polaroids); (b) optical response of PIC in the two-wave mode to the variation of longitudinal $\mathcal{I}_l$ and shear $\mathcal{I}_s$ wave intensities (frequency of ~16 MHz; crossed polaroids) for $\mathcal{I}_s$ = 0.1 (*2*), 0.2 (*6*), 0.3 (*3*), 0.7 (*4*), 0.9 (*7*) 1.3 W/cm^3 (*5*) and $\mathcal{I}_l$ varied from 0.08 to 5 mW/cm^2.

the NLC by a shear wave adds to the longitudinal secondary waves and interacts with the initial longitudinal wave in the central part of the NLC layer. The firmer superposition enhances the boundary effect, while the latter interaction creates a new field of flows in the central region, the scale and configuration of which is determined by the wave field structure in the NLC layer. A homogeneous clearing observed in this region reflects a distribution of the amplitudes of oscillations (coherent and homogeneous in the acoustic beam cross- section) created by the emitter radiator *6* oscillating as a hard piston (Fig. 1c).

The above considerations show that the transition from a conventional single-wave mode to the two-wave PIC functioning leads to a more than tenfold increase in the sensitivity, allows the sensitivity level to be controlled in the course of the device operation, and ensures a homogeneous PIC response to the acoustic wave action, reflecting a real distribution of the amplitude of the reciprocating oscillations of emitter *6*. The results of these tests confirm the good prospects for the new concept of PIC functioning in acoustic visualization systems.

REFERENCES

1. P. Greguss, Acustica **29** (1), 52 (1973).
2. O. Kapustina, in *Handbook of Liquid Crystals*, Ed. by D. Demus *et al.* (Wiley, Weinheim, 1998), pp. 549–568.
3. J. Perbet and M. Hareng, Rev. Phys. Appl. **14** (4), 569 (1979).
4. A. Strigazzi and G. Barbero, Mol. Cryst. Liq. Cryst. **103** (4), 193 (1993).
5. R. S. Akopyan and B. Ya. Zel'dovich, Akust. Zh. **34** (4), 583 (1988) [Sov. Phys. Acoust. **34**, 337 (1988)].
6. D. Anikeev, Yu. Bocharov, and A. Vuzva, Liq. Cryst. **6**, 593 (1989).
7. E. N. Kozhevnikov, Akust. Zh. **27** (4), 533 (1981) [Sov. Phys. Acoust. **27**, 297 (1981)].

Translated by P. Pozdeev

Technical Physics Letters, Vol. 27, No. 1, 2001, pp. 77–80. Translated from Pis'ma v Zhurnal Tekhnicheskoĭ Fiziki, Vol. 27, No. 2, 2001, pp. 76–83.

Variation of the Adsorption Properties of Porous Silicon in the Course of Natural and High-Temperature Aging

A. M. Orlov, A. A. Skvortsov, A. G. Klement'ev, and A. V. Sindyaev

Ul'yanovsk State University, Ul'yanovsk, Russia

Received August 3, 2000

Abstract—The photo- and thermostimulated adsorption–desorption processes on the surface of porous silicon (por-Si) were studied in the course of natural and high-temperature degradation of the samples. The results of IR absorption, luminescence, and Auger electron spectroscopy measurements indicate that an active stage in the sample morphology variation under the natural aging conditions lasts for a prolonged time (exceeding 74 days) upon the por-Si layer formation and is accompanied by redistribution of the adsorbed molecules. The surface properties vary so as to favor the adsorption of oxygen, carbon, and, probably, OH groups. The high-temperature (1149 K) treatment of the por-Si surface in acetone vapor favors the formation of a carbonized layer possessing a characteristic photoluminescence spectrum with a maximum intensity at 458 nm. The IR spectra indicate the presence of a silicon carbide phase, identified as the cubic β-SiC, with a characteristic absorption at 800–833 cm^{-1}. A strong shift of the high-frequency wing of the IR absorption spectrum is explained by the carbon substitution for one oxygen in the O–Si–O groups. © *2001 MAIK "Nauka/Interperiodica".*

The nanoporous structures, exhibiting unique physical and chemical properties, find increasing use in various fields of modern science and technology. Possessing a highly developed surface, these materials are known to be excellent adsorbents and are capable of strongly changing their physical properties in accordance with the quantum-dimensional character of their structures.

An illustrative example is offered by the porous silicon (por-Si) exhibiting an intense red-orange photoluminescence (PL) not typical of the single-crystal silicon and possessing a markedly higher resistivity than the latter material [1]. Despite this fact, some researchers argue against a decisive role of the combined manifestation of both the quantum confinement phenomena and the adsorbate effects in the PL of por-Si [2, 3] and even of the adsorbate nature responsible for the visible PL [3–6].

This question could be elucidated by data on the photo- and thermostimulated processes on the surface of por-Si, but such information is very restricted [7, 8]. Even less data are available on the high-temperature controlled adsorption, where no complex investigations apparently have been ever conducted. The purpose of this study was to fill this gap.

The main task of our experiments was to investigate the surface state of por-Si samples subject to various natural factors and to high-temperature treatment and to assess the role of adsorption coating in the PL of por-Si. The controlled adsorbate was represented by the simplest ketone (acetone CH_3COCH_3), the molecules of which are characterized by extremely high surface activity. At the same time, the products of acetone pyrolysis (700–1000°C) may produce carbonization of the pore walls in the por-Si structure. The surface of the samples was analyzed by a combination of methods, the main ones being the IR absorption spectroscopy (400–4000 cm^{-1}), the Auger electron spectroscopy (AES), and the PL spectral analysis (300–850 nm). High-quality IR spectra were obtained using the samples prepared on silicon plates with a thickness not exceeding 200 μm, which was adjusted by etching dislocation-free single-crystal *p*-Si (B) wafers in a standard CP etchant prior to the por-Si layer formation.

The por-Si layers were formed on both sides of the {111}-oriented single-crystal silicon substrates ($\rho \approx 2.8\ \Omega$ cm) by 40-min electrochemical etching (j = 20 mA/cm^2) in a mixture of hydrofluoric acid and ethyl alcohol. During etching, a desired fragment of the silicon plate (~$10 \times 20 \times 0.2$ mm) was immersed into the etchant. An advantage of the anodic etching technology employed consisted in not using hermetic sealers (paraffin, wax, etc.), which excluded the appearance of spurious peaks due to these compounds in the IR spectra. The freshly prepared por-Si plates were subjected to stabilization annealing [7] for 1 h at 200–215°C and a pressure of 133×10^{-4} Pa.

Carbonization of the porous layer by the heat treatment in acetone vapor (140 s at 1131 K, $p \le 2.4 \times 10^4$ Pa) was accompanied (in the absence of atmospheric oxygen) by the pyrolytic decomposition of acetone to elementary carbon.

Figure 1 shows typical IR spectra of the initial silicon plate (spectrum *1*) and a freshly prepared por-Si on the same substrate (spectrum *3*). The clearly pro-

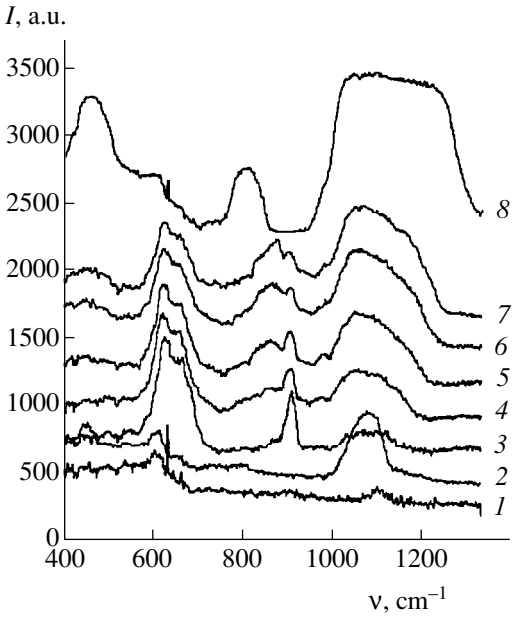

Fig. 1. IR absorption spectra: (*1*) initial single-crystal *p*-Si substrate; (*2*) *p*-Si oxidized for 1 h at 1273 K; (*3*) freshly prepared por-Si on the same substrate; (*4–7*) por-Si aged in air under the natural conditions for 5, 15, 46, and 74 days, respectively; (*8*) por-Si carbonized in acetone vapor. All spectra are shifted in an ordinate relative to spectrum *1*: the interval between sequential spectra *1–7* is 250 a.u.; the shift between spectra *1* and *2* is 2200 a.u.

nounced IR absorption bands (~610 and ~1080 cm^{-1}) are characteristic of the single-crystal silicon. The former band (610 cm^{-1}) represents essentially a combination of bands due to two (or more) phonons with equal vectors belonging to various lines of the vibrational spectrum [10]. The latter absorption band (1080 cm^{-1}) is due to the stretching vibrations of oxygen and silicon in a bridging structure of the O–Si–O type [8, 9, 11]. This peak reflects the state of the natural oxide on the silicon surface, as well as the state of oxygen dissolved in this layer. The amplitude of this peak increases with the temperature and the duration of oxidation. After a 60-min oxidation of the initial silicon plate at 1273 K, this band shows a 230% increase in intensity (Fig. 1, spectrum *2*). This treatment also leads to the appearance of a new band in the region of 460 cm^{-1}, which is probably due to the bending vibrations of O–Si–O groups. This peak is missing in the spectrum of the initial silicon plate, which does not allow us to assign it to the stretching vibrations of atoms in this chain (as was done for the spectrum of por-Si in [8]); the energy of the bending vibrations is markedly lower than that of the stretching ones, and the former have to be manifested at lower frequencies.

The formation of a porous layer during the anodic etching of single-crystal silicon in hydrofluoric acid solutions is accompanied by the active adsorption of hydrogen on the pore walls (Fig. 1, spectrum *3*): it is this hydrogen that accounts for the appearance of absorption bands at ~626, 904 cm^{-1} (SiH_2) and ~660, 2087 cm^{-1} (SiH) in agreement with the data of other researchers summarized in [8, 9]. Of special interest is the evolution of spectra in the course of subsequent aging of the freshly prepared por-Si samples in air. In particular, the increasing role of oxygen is especially clearly pronounced by the variation of absorption in the region of 1080 cm^{-1} (O–Si–O), where the maximum absorption intensity gradually shifts toward 1030 cm^{-1} (Fig. 1, spectra *3–6*). The same trends are manifested, albeit to a less pronounced extent, by the absorption at 460 cm^{-1}.

The intensity of the main absorption peak due to oxygen and, hence, the optical absorption in the corresponding frequency interval, increase with time by a law that is indicative of the diffusion limitations in the oxide layer formation in por-Si. Indeed, in the por-Si samples aged under the natural conditions in air for 46 and 74 days, the intensity of the band at 1080 cm^{-1} gradually increases by 344%. However, these changes are simultaneously accompanied by a decrease in the intensity of hydrogen-related peaks, this being indicative of a slow desorption of hydrogen. Intensities of the overlapping bands of SiH_2 (626 cm^{-1}) and SiH (660 cm^{-1}) decrease during the time indicated above by 8.9 and 3%, respectively. Another fact to be noted is the rapid growth of absorption in the region of 860 cm^{-1} (313% over the same period of time), which was very weakly pronounced in the spectrum of initial por-Si. This absorption cannot be related to oxygen, since a plasmachemical treatment leads to the complete disappearance of this band, but not of the bands due to oxygen. This band is probably related to the hydroxy groups (OH), evidencing gradual conversion of the $Si–H_x$ centers into Si–OH.

The high-temperature carbonization leads to a significant redistribution of the absorption components in the spectrum of por-Si (Fig. 1, spectrum *8*). The spectra of samples upon this treatment are characterized by the virtually complete absence of the bands due to hydrogen and a sharp increase in the role of oxygen- ($\nu \approx 460$ and 1080 cm^{-1}) and carbon-related (~806 and 1150–1220 cm^{-1}) absorption. In particular, the strong growth in intensity of the band at 1080 cm^{-1} is accompanied by its significant broadening: the absorption extends from ~1030 to 1230 cm^{-1}, which markedly exceeds frequently reported limits (1065–1100 cm^{-1}) [8, 9, 11].

While a small shift of the low-frequency absorption wing can be related to structural defects of the type of broken (or deformed) bonds or excess silicon atoms in the lattice (appearing due to the deficit of oxygen and thermal aggregation or as a result of the plasma action [11]), the strong shift of the high-frequency wing can be explained by an increase in the resonance vibration frequency upon the partial replacement of oxygen by lighter carbon atoms. Indeed, using the known expression [12] for the frequency of stretching

vibrations of two bound centers with the molecular masses M_x and M_y:

$$\nu = \frac{1}{2\pi c}\left(KN_A\frac{M_x + M_y}{M_xM_y}\right)^{0.5},$$

where c is the speed of light, K is the force constant of the bond ($K \approx 5 \times 10^2$ and 1×10^3 N/m for the single and double bonds, respectively), and N_A is the Avogadro number.

In order to obtain an estimate, let us reduce the three-center O–Si–O chain to a two-center system by replacing the O–Si pair with one particle possessing an effective mass $M_x = 13.34 \times 10^{-3}$ kg/mol (readily evaluated using the above equation and the known limiting value $\nu = 1080$ cm^{-1} determined by the stretching vibrations of the O–Si–O system). Upon substituting carbon for oxygen (M_y) in the two-center system leads to a value ($\nu = 1159$ cm^{-1}) that agrees well with experiment. The agreement is further corroborated by the increasing asymmetry of the high-frequency absorption band (~1080 cm^{-1}) observed in the course of the natural aging process in por-Si (Fig. 1). The asymmetry is related to a clear manifestation of the absorption peak at ~1155 cm^{-1}, which we attribute (see data for samples 1 and 2 in the table) to the active adsorption of carbon.

The pyrolytic decomposition of acetone to elementary carbon, accompanying the carbonization treatment, favors the formation of a surface silicon carbide film. The thickness of this film apparently does not exceed several nanometers, since this phase could not be detected by the methods of Raman light scattering and X-ray diffraction. Only the IR absorption spectra indicate the presence of the silicon carbide phase (Fig. 1, spectrum *8*) that can be identified by the absorption band position at ~806 cm^{-1} as the cubic β-SiC modification (typically reported values vary within the interval $\nu \approx 800$–833 cm^{-1} [13, 14], depending on the sample preparation conditions). This absorption band cannot be related to oxygen, since the high-temperature oxidative annealing of the initial silicon does not give rise to this feature in the spectrum (Fig. 1, spectrum *2*). Indirect evidence for the presence of the carbide phase can be found in the PL spectra (Fig. 2), which show a blue luminescence with a maximum at $\lambda_{max} = 458$ nm. This peak is shifted by more than 230 nm relative to the analogous feature in the spectrum of por-Si not subjected to the carbonization treatment (Fig. 2, spectrum *1*). The curve of the PL intensity kinetics $I(t)$ does not exhibit an extremal character typical of the freshly prepared por-Si samples [15].

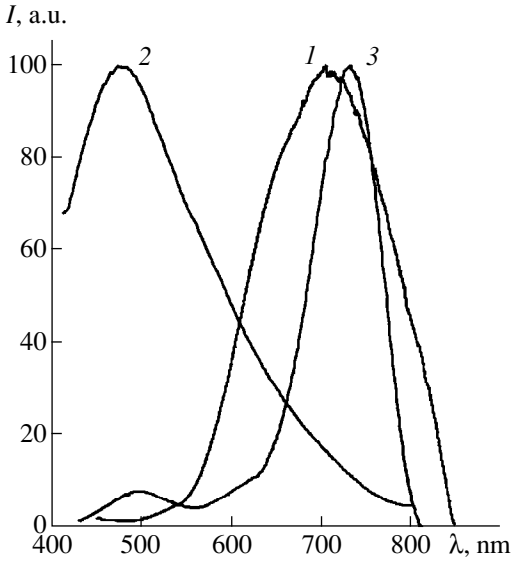

Fig. 2. PL spectra of por-Si samples: (*1*) freshly prepared por-Si treated for 60 min at 488 K in vacuum; (*2*) por-Si carbonized in acetone vapor; (*3*) por-Si after plasmachemical treatment in an oxygen-containing atmosphere.

The plasmachemical treatment significantly changes both the chemical composition (see data for samples 4–6 in the table) and the PL spectra (cf. spectra *2* and *3* in Fig. 2) of carbonized por-Si. The luminescence spectrum displays two distinct maxima, the first (small component) of which being indicative of a residual car-

Surface composition of por-Si layers (at. %) by AES data

Sample no.	State of por-Si sample	Chemical element			PL
		Si	C	O	
1	Freshly prepared	40.2	47.0	12.8	Red
2	Stored for 6 months in air	11.2	71.6	14.2	Red
3	Vacuum-annealed (1 h, 490 K)	9.3	72.5	18.2	Red
4	Plasma-treated (40 min) in oxygen-containing atmosphere	49.7	Trace	50.3	Red (very weak)
5	Carbonized (point 4 excluded)	2.4	94.5	3.1	Blue
6	Plasma-treated (40 min) after carbonization (point 4 excluded)	39	27.5	33.5	Red

Note: Sample numbers indicate the sequence of treatments.

bonized SiC layer ($\lambda_{max} \approx 492$ nm), while the second (major component) is due to the PL of por-Si ($\lambda_{max} \approx 723$ nm). However, the major PL response is no longer related to the hydrogen adsorption, but reflects an increase in the oxygen component in the previously formed O–Si–C chains ($\nu \approx 1030$–1220 cm^{-1}) and the additional silicon oxidation to SiO_2 ($\nu \approx 460$ cm^{-1}), in complete agreement with the AES surface analysis (see data for samples 5 and 6 in the table).

Thus, based on the experimental data obtained, we may suggest that an active stage in the por-Si layer morphology variation under the natural aging conditions lasts for a prolonged time (exceeding 74 days) upon the por-Si layer formation by the electrochemical oxidation method. This process is accompanied by the redistribution of the adsorbed molecules. The surface properties vary so as to favor the adsorption of oxygen, fluorine, and carbon. The high-temperature carbonization and plasmachemical treatment of por-Si lead to considerable changes in the adsorption coating on the silicon skeleton and in the character of the PL, which is explained by the formation of a very thin silicon carbide layer. It was established that the nature of a strong shift in the high-frequency wing of the IR absorption spectrum related to the carbon displacing one oxygen atom in the O–Si–O chain.

REFERENCES

1. A. G. Gullis, L. T. Canham, and P. D. G. Calcott, J. Appl. Phys. **82** (3), 909 (1997).
2. Yoshihiko Kanemitsu, J. Crystallogr. Soc. Jpn. **38** (2), 144 (1996).
3. G. G. Qin, H. Z. Song, B. R. Zhang, *et al.*, Phys. Rev. B **54** (4), 2548 (1996).
4. C. S. Chang and J. T. Lue, Thin Solid Films **259** (2), 275 (1995).
5. Zoubir N. Hadj, M. Vergnat, T. Delatour, *et al.*, Thin Solid Films **255** (1–2), 228 (1995).
6. T. Shimuzu-Iwayama, Y. Terao, A. Kamiya, *et al.*, Nanostruct. Mater. **5** (3), 307 (1995).
7. P. K. Kashkarov, E. A. Konstantinova, and V. Yu. Timoshenko, Fiz. Tekh. Poluprovodn. (St. Petersburg) **30** (8), 1479 (1996) [Semiconductors **30**, 778 (1996)].
8. Yu. A. Bykovskiĭ, V. A. Karavanskiĭ, G. E. Kotkovskiĭ, *et al.*, Poverkhnost', No. 9, 23 (1999).
9. A. A. Kopylov and A. N. Kholodilov, Fiz. Tekh. Poluprovodn. (St. Petersburg) **31** (5), 556 (1997) [Semiconductors **31**, 470 (1997)].
10. *Semiconductors*, Ed. by N. B. Hannay (Reinhold, New York, 1959; Inostrannaya Literatura, Moscow, 1962).
11. N. V. Rumak and V. V. Khat'ko, *Dielectric Films in Solid-State Microelectronics,* Ed. by V. E. Borisenko (Navuka i Tékhnika, Minsk, 1990).
12. John R. Dyer, *Applications of Absorption Spectroscopy of Organic Compounds* (Prentice-Hall, Englewood Cliffs, 1965; Khimiya, Moscow, 1970).
13. V. S. Vavilov, V. F. Kiselev, and B. N. Mukashev, *Defects in Silicon and on Its Surface* (Nauka, Moscow, 1990).
14. Yong Sun and Tatsuro Miyasato, Jpn. J. Appl. Phys., Part 1 **37**, 5485 (1998).
15. A. M. Orlov and A. V. Sindyaev, Zh. Tekh. Fiz. **69** (6), 135 (1999) [Tech. Phys. **44**, 729 (1999)].

Translated by P. Pozdeev

Technical Physics Letters, Vol. 27, No. 1, 2001, pp. 81–83. Translated from Pis'ma v Zhurnal Tekhnicheskoĭ Fiziki, Vol. 27, No. 2, 2001, pp. 84–89.

On Increasing the Hydrostatic Sensitivity of Three-Component Piezocomposites

V. Yu. Topolov and A. V. Turik

Department of Physics, Rostov State University, Rostov-on-Don, 344104 Russia

e-mail: topolov@phys.rnd.runnet.ru

In final form received September 13, 2000

Abstract—A 1–0–3 composite model of the "ferroelectricpiezoceramic–polymer 1–polymer 2" type is proposed. It is demonstrated that the square hydrostatic figure of merit (HFOM) in this system may reach a level of $(Q_h^*)^2 \sim 10^{-11}$ Pa^{-1}, which exceeds by approximately one order of magnitude the known estimates for 1–3 composites. Factors favoring an increase in the $(Q_h^*)^2$ value in three-component piezocomposites are discussed. © *2001 MAIK "Nauka/Interperiodica".*

The hydrostatic sensitivity of hydrophones, actuators, and materials used in these devices is characterized by a receipt parameter Q_h^* and the piezocoefficients d_h^* and g_h^*. For a material with the ∞mm symmetry, these quantities obey a relationship[1]

$$(Q_h^*)^2 = d_h^* g_h^* = (d_{33}^* + 2d_{31}^*)^2/\varepsilon_{33}^{*\sigma}, \qquad (1)$$

where d_{3j}^* are the piezoelectric moduli and $\varepsilon_{33}^{*\sigma}$ is the dielectric permittivity of a mechanically free sample. The value $(Q_h^*)^2$ is called the hydrophone figure of merit [1, 2] or the hydrostatic figure of merit (HFOM) [3, 4]. Previously, researchers concentrated on the two-component 1–3-composites of the "ferroelectricpiezoceramics (FPC)–polymer" type with maximum HFOM values on a level of $\max(Q_{h,1-3}^*)^2 \approx (2000–4000) \times 10^{-15}$ Pa^{-1} [1, 3, 4] and did not attempt to increase this level by modifying the composite structure or by introducing new components.[2]

Recently [5, 6] we have demonstrated the advantages of using three-component composites with 1–3 connectivity components, which can provide for a greater anisotropy of the piezomoduli d_{3j}^* or piezocoefficients e_{3j}^*. In this paper, we describe a model of the 1–0–3 composite possessing extremely high HFOM values as compared to $(Q_{h,1-3}^*)^2$ of a two-component system.

The proposed composite structure comprises elongated FPC rods oriented parallel to the polarization axis OX_3, which are surrounded by a piezopassive heterogeneous 0–3 matrix (Fig. 1). The matrix comprises alternating layers of araldite ($n = 1$) and an elastomer ($n = 2$) possessing room-temperature elastic moduli c_{ij} [7, 8] obeying the relationship

$$c_{11}^{(1)}/c_{11}^{(2)} = 6.84; \quad c_{11}^{(1)}/c_{12}^{(1)} = 1.77; \quad c_{11}^{(2)}/c_{12}^{(2)} = 1.22, \qquad (2)$$

and the dielectric permittivities $\varepsilon_{ii}^{(n)}$ such that $\varepsilon_{ii}^{(1)}/\varepsilon_{ii}^{(2)} = 0.80$ ($i, j = 1, 2, 3$). The effective elastic, piezoelectric, and dielectric constants were determined as functions of m, r, and ν by averaging the corresponding polymer characteristics within the framework of a model described in [8] for 0–3 connectivities, followed by averaging the FPC and 0–3 matrix parameters using the formulas from [7] for 1–3 connectivities. Using these effective constants, the HFOM values $(Q_h^*)^2 = (Q_h^*)^2(m, r, \nu)$ were calculated by formula (1).

An analysis of the experimental electromechanical constants for numerous $Pb(Zr_{1-x}Ti_x)O_3$ (PZT)-based FPCs [9, 10] and the results of preliminary HFOM calculations indicated that the best results can be obtained in the structures with rods made of the PKR-7M type FPC. With this FPC, $\max(Q_h^*)^2 > (Q_{h,1-3}^*)^2$ for $0 < r < 1$ and $\nu = \text{const}$, while the maximum $(Q_{h,ext}^*)^2 = 50500 \times 10^{-15}$ Pa^{-1} is observed for $r = 1$ and $\nu = 0.34$

[1] Asterisk denotes the effective electromechanical constants of a piezocomposite; the other superscripts refer to the parameters of components: FC, ferroelectricpiezoceramic; M, matrix; (n) = nth component of the matrix.

[2] According to Newnham [1], the composite structure is characterized by the connectivity. The connectivity of a two- or three-component composite is denoted by α–β or α–β–γ, respectively, where the integers α, β, γ = 0, 1, 2, 3 indicate the number of axes in the $(X_1X_2X_3)$ Cartesian system of coordinates along which the corresponding component is continuously distributed.

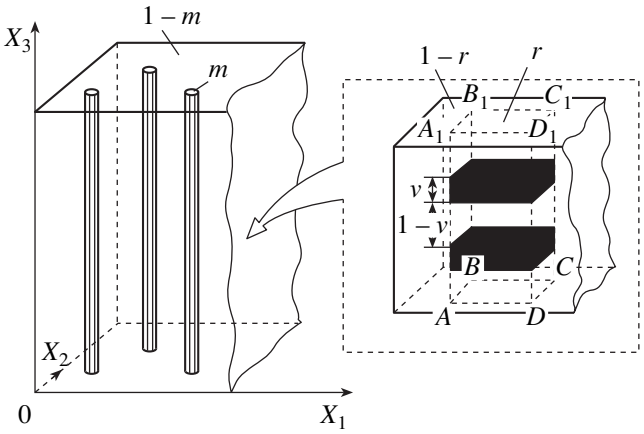

Fig. 1. A schematic diagram of the model of a piezoactive 1–0–3 composite: m is the volume fraction of cylindrical FPC rods embedded into an 0–3 matrix (volume fraction, $1 - m$). The inset shows a scheme of the matrix structure element–rectangular parallelepiped $ABCDA_1B_1C_1D_1$ with $AB = BC \ll AA_1$, comprising alternating layers of polymers 1 and 2 with relative thicknesses ν and $1 - \nu$, respectively; r is the volume fraction of such elements in the matrix.

(Fig. 2a), which implies the passage from 1–0–3 (Fig. 1) to 1–2–2 connectivity. Behavior of the $(Q_h^*)^2(m, 1, \nu)$ curves calculated for the 1–2–2 connectivity showed that the absolute HFOM maximum is attained near $m = 0.014$ and $\nu = 0.34$ (Fig. 2b). Note that the maximum HFOM reported previously for the PZT-based 2–2–0 composites was $(Q_{h,ext}^*)^2 = 50000 \times 10^{-15}$ Pa^{-1} [1]; no data on the HFOM of 1–0–3 or 1–2–2 systems were available.

In order to elucidate the factors accounting for anomalously high $(Q_h^*)^2(m, r, \nu)$ values of the proposed composites, let us consider formula (1) written in a modified form

$$(Q_h^*)^2 \approx \eta_{el}^*(e_{33}^*/c_{33}^{*E})^2/\varepsilon_{33}^{*\sigma}, \qquad (3)$$

where $\eta_{el}^* = \{[1 + (\beta_{12}^*)^{-1} - 2(\beta_{13}^*)^{-1}]/[1 + (\beta_{12}^*)^{-1} - 2(\beta_{13}^*)^{-1}(\beta_{33}^*/\beta_{13}^*)]\}^2$, and $\beta_{jk}^* = c_{11}^{*E}/c_{jk}^{*E}$, c_{jk}^{*E} are the elastic moduli of the composite. Formula (3) is derived

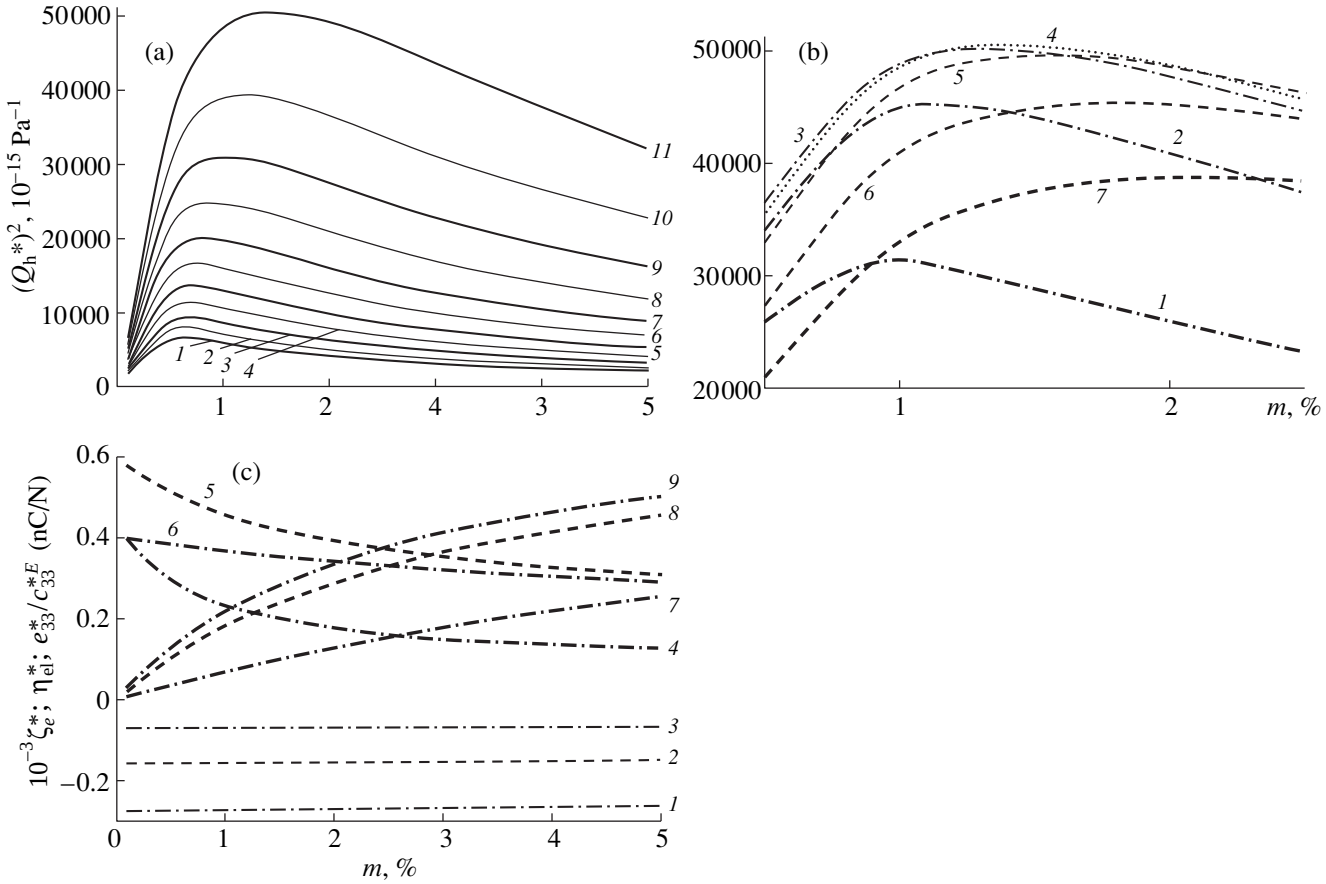

Fig. 2. Fragments of the plots of (a, b) $(Q_h^*)^2$ and (c) $10^{-3}\zeta_e^*$, η_{el}^*, and e_{33}^*/c_{33}^{*E} vs. the FPC volume fraction calculated for various 1–0–3 and 1–2–2 "FPC (PKR-7M)–araldite–elastomer" compositions: (a) $\nu = 0.34$ and $r = 0.01$ (*1*), 0.1 (*2*), 0.2 (*3*), 0.3 (*4*), 0.4 (*5*), 0.5 (*6*), 0.6 (*7*), 0.7 (*8*), 0.8 (*9*), 0.9 (*10*), 1.0 (*11*); (b) $r = 1$ and $\nu = 0.10$ (*1*), 0.20 (*2*), 0.30 (*3*), 0.34 (*4*), 0.40 (*5*), 0.50 (*6*), 0.60 (*7*); (c) (*1–3*) $10^{-3}\zeta_e^*(m, 1, \nu)$, (*4–6*) $\eta_{el}^*(m, 1, \nu)$, and (*7–9*) $e_{33}^*(m, 1, \nu)/c_{33}^{*E}(m, 1, \nu)$ in (nC/N) for $\nu = 0.10$ (*1*, *4*, *7*), 0.34 (*2*, *5*, *8*), 0.90 (*3*, *6*, *9*).

in the approximation of $|\zeta_e^*| = |e_{33}^*/e_{31}^*| \gg 1$, which is reliably valid for 1–3 [5, 6], 1–0–3, and 1–2–2 composites (Fig. 2c, curves *1–3*) with FPC rods and polymeric matrix components. According to [7], the systems with 1–3 connectivity and $m \sim 10^{-2}$ possess $e_{33}^*/c_{33}^{*E} \sim e_{33}^{FC}/c_{33}^{FC, E}$, while for $\varepsilon_{33}^{FC, \sigma} \gg \varepsilon_{33}^{(n)}$ (n = 1, 2) we have $\varepsilon_{33}^{*\sigma} \sim m\varepsilon_{33}^{FC, \sigma}$. Behavior of the factor η_{el}^*, which is determined by the elasticity anisotropy of both FPC and the heterogeneous matrix, is illustrated in Fig. 2c (curves *4–6*). For $m \sim 10^{-2}$, the terms $mc_{jk}^{FC, E}$ and $(1-m)c_{jk}^M$ accounting for the main contributions to c_{jk}^{*E} from FPC rods and the matrix, respectively, become comparable in magnitude; however, the ratios $c_{jk}^{FC, E}/c_{pq}^{FC, E}$ and c_{jk}^M/c_{pq}^M are still significantly different and may affect the η_{el}^* value. For example, the PKR-7M rods possess $c_{11}^{FC, E}/c_{33}^{FC, E} = 1.06$ and $c_{12}^{FC, E}/c_{13}^{FC, E} = 1.01$, while a 2–2 matrix with $\nu = 0.34$ has $c_{11}^M/c_{33}^M = 1.82$ and $c_{12}^M/c_{13}^M = 1.38$.

According to formula (3), the HFOM variation is determined predominantly by "competition" of the concentration dependences of η_{el}^* and e_{33}^*/c_{33}^{*E} (cf. Fig. 2c, curves *4–6* and *7–9*) on the background of a relatively weak increase in $\varepsilon_{33}^{*\sigma}(m, 1, \nu)|_{n = \text{const}}$. In particular, the substitution of PKR-73 for PKR-7M in the 1–2–2 composite leads to a decrease in HFOM: $(Q_{h, ext}^*)^2 = (Q_h^*)^2 (0.017, 1, 0.33) = 47400 \times 10^{-15}$ Pa^{-1}. In PKR-73: $c_{11}^{FC, E}/c_{33}^{FC, E} = 1.20$, $c_{12}^{FC, E}/c_{13}^{FC, E} = 1.06$, and $\varepsilon_{33}^{FC, \sigma}$ is 1.20 times the value in PKR-7M, while $e_{33}^{FC}/c_{33}^{FC, E}$ is 1.23 times smaller than the same ratio of PKR-7M [10]. In a composite containing the rods made of a modified $PbTiO_3$ FPC, $(Q_{h, ext}^*)^2 = 5080 \times 10^{-15}$ Pa^{-1}. This is explained by the effect of $c_{11}^{FC, E}/c_{33}^{FC, E} = 1.09$ and $c_{12}^{FC, E}/c_{13}^{FC, E} = 1.33$ ratios [9] on the η_{el}^* value and by the $e_{33}^{FC}/c_{33}^{FC, E}$ ratio being five times smaller than the value in PKR-7M.

Thus, we have demonstrated that the proposed piezocomposite model allows the maximum possible HFOM values to be obtained upon going from matrix 0–3 to 2–2. It is established that factors effectively determining the HFOM of this composite system are the piezoelectric anisotropy of components ($|\zeta_e^*| \gg 1$) and the ratios $e_{33}^{FC}/c_{33}^{FC, E}$, $c_{jk}^{FC, E}/c_{pq}^{FC, E}$, and c_{jk}^M/c_{pq}^M. The effect of elasticity anisotropy on the HFOM value consists in a significant redistribution of the mechanical and electric fields in the composite, which is especially pronounced when a combination of polymers possessing markedly different elastic properties, such as in condition (2), is used as a layered polymer matrix.

REFERENCES

1. R. E. Newnham, MRS Bull. **22** (5), 20 (1997).
2. O. Sigmund, S. Torquato, and I. A. Aksay, J. Mater. Res. **13** (4), 1038 (1998).
3. G. Hayward, IEEE Trans. Ultrason. Ferroelectr. Freq. Control **43** (1), 98 (1996).
4. J. Bennett and G. Hayward, IEEE Trans. Ultrason. Ferroelectr. Freq. Control **44** (3), 565 (1997).
5. V. Yu. Topolov and A. V. Turik, Pis'ma Zh. Tekh. Fiz. **24** (11), 65 (1998) [Tech. Phys. Lett. **24**, 441 (1998)].
6. V. Yu. Topolov and A. V. Turik, J. Electroceram. **3** (4), 347 (1999).
7. A. A. Grekov, S. O. Kramarov, and A. A. Kuprienko, Mekh. Kompoz. Mater., No. 1, 62 (1989).
8. F. Levassort, M. Lethiecq, D. Certon, and F. Patat, IEEE Trans. Ultrason. Ferroelectr. Freq. Control **44** (2), 445 (1997).
9. *Landolt-Börnstein. Zahlenwerte und Funktionen aus Naturwissenschaften und Technik. Neue Serie* (Springer-Verlag, Berlin, 1984; 1990), Gr. III, Bd. 18; Bd. 28.
10. V. Yu. Topolov and A. V. Turik, J. Phys. D **33** (6), 725 (2000).

Translated by P. Pozdeev

Technical Physics Letters, Vol. 27, No. 1, 2001, pp. 84–85. Translated from Pis'ma v Zhurnal Tekhnicheskoĭ Fiziki, Vol. 27, No. 2, 2001, pp. 90–94.

Nuclear Spin Echo in Magnetic Fluids

I. A. Aleksashkin, V. N. Berzhanskiĭ, E. D. Pershina, S. N. Polulyakh, and M. V. Turishchev

Tauric National University, Simferopol, Crimea, Ukraine

e-mail: roton@tnu.crimea.ua

Received August 21, 2000

Abstract—The two-pulse proton spin echo signal decay was studied in benzene-based magnetic fluids containing magnetite (filler) and oleic acid (surfactant). The spin echo signal decay rate increases with the magnetic filler concentration. A decrease in the transverse proton relaxation time is due to the increasing inhomogeneity of the local nuclear magnetic fields. © *2001 MAIK "Nauka/Interperiodica".*

The colloidal suspensions of magnetic nanoparticles offer, along with their practical applications, an interesting object for fundamental research. The structures formed by such magnetic particles exposed to an external magnetic field were recently studied [1, 2] by indirect methods based on the magnetic resonance of the fluid base. This approach consists in studying the shape of the resonance spectral line, the inhomogeneous broadening of which is related to dissipation fields created by the magnetic particles [1].

The main method of investigation of the spin system with inhomogeneously broadened spectral lines is the spin echo technique [3]. The spin echo signal shape is essentially the Fourier image of the line shape function, the spin echo decay rate is determined by the magnetic relaxation processes related to the local magnetic field fluctuations. In the ^{1}H NMR study of the magnetic fluid base reported in [1], the main attention was devoted to the analysis of the resonance line shape in the samples with magnetic fillers of various types.

The purpose of our work was to study the influence of the magnetic filler concentration on the conditions of observation and the rate of decay of the proton spin echo signal from the magnetic fluid base.

The experiments were performed with magnetic fluids based on benzene, containing a magnetic filler (magnetite nanoparticles) and a surfactant component (oleic acid). The magnetite nanoparticles were synthesized by a chemical reaction of the aqueous solutions of $FeSO_4$ and $FeCl_3$ with aqueous ammonia (an alkalizing agent). The reaction product–magnetite–was separated from the reaction mixture by centrifugation. The magnetic suspensions were prepared by mixing the magnetite nanoparticles with a benzene solution of oleic acid.

The magnetite concentration in the suspension was determined by weighing the dry residue after the evaporation of a sample with a known volume. The samples with preset concentrations of the magnetic filler were prepared by diluting a stock solution with a magnetite concentration of 0.3 mol/l. The spin echo measurements were performed at T = 35°C in a Bruker Minispec P20 pulse relaxometer operated at a magnetic field induction of B = 0.5 T.

The ^{1}H NMR measurements at certain fixed values of the constant and alternating magnetic field, corresponding to the proton magnetic resonance in a nonmagnetic fluid, and the free induction signal measurements with a lock-in detector revealed oscillations in decay of the proton free induction signal from the magnetic fluids studied. The oscillation frequency increased with the magnetic filler concentration, which was indicative of a shift in the center-of-gravity of an inhomogeneously broadened ^{1}H NMR line [3, 4]. The results of additional investigations showed that the signal shifts toward lower field strengths. Moreover, measurements of the free induction signal and the Hahn two-pulse spin echo signal with an amplitude detector also revealed a decrease in the duration of each response with increasing concentration of magnetic particles (Fig. 1), which is indicative of an increase in the spectral line width [3, 4].

The experimentally observed features in the behavior of the pulse NMR response in the magnetic fluids studied agree well with the results reported in [1] and are explained by the fact that there are two contributions to the proton resonance field: the constant external magnetic field and the dissipation fields of magnetic particles. The magnetic moments of particles are oriented along the external magnetic field, while the dissipation fields are opposite to this field. As a result, the resonance line shifts toward lower frequencies. The dissipation field exhibits a maximum gradient at the particle surface and decreases with distance from the particle. The fraction of protons occurring in the region of the strong field gradient increases with the magnetic filler concentration, which leads to the observed increase in inhomogeneous broadening of the spectral line.

1063-7850/01/2701-0084$21.00

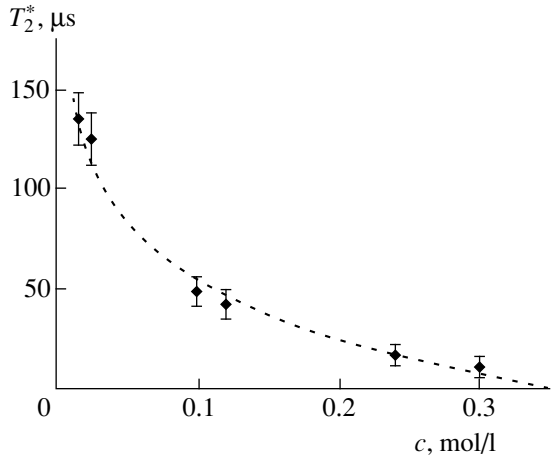

Fig. 1. A plot of the spin echo signal halfwidth at half height T_2^* vs. magnetic filler concentration c.

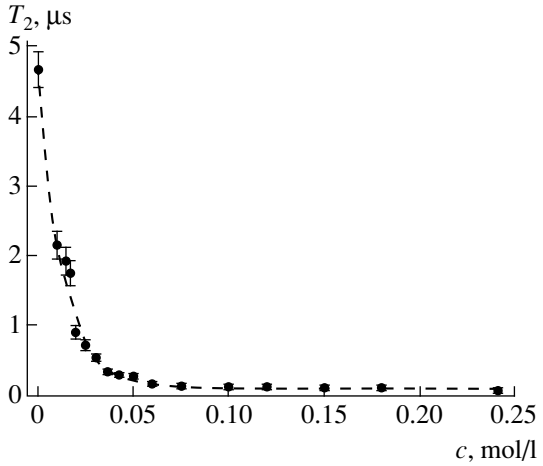

Fig. 2. A plot of the transverse proton relaxation time T_2 vs. magnetic filler concentration c.

Study of the Hahn two-pulse spin echo signal amplitude V as a function of the time interval between the excitation pulses showed that this dependence is well approximated by the exponent

$$V(\tau) = V(\tau)\exp(-2\tau/T_2), \quad (1)$$

where T_2 is the transverse proton relaxation time. The experimental results reveal a decrease in T_2 with increasing magnetic filler concentration (Fig. 2).

As is known [3, 4], the transverse proton relaxation time in a magnetic fluid is determined by the local nuclear magnetic field fluctuations. An exponential decay of the spin echo is observed when the local field fluctuations are described by a rapid random process with $\Delta\omega\tau_c \ll 1$, where $\Delta\omega$ is the fluctuation amplitude and τ_c is the correlation time. An increase in the fluctuation amplitude decreases the relaxation rate.

In the case of a magnetic fluid exposed to the constant magnetic field, we may assume that the magnetic particles form a structure of filaments oriented along the field. The structure is effectively "frozen" in the external magnetic field, so that we may ignore the motion of particles and consider the local magnetic field fluctuations at the protons as determined by the molecular mobility. An increase in the magnetic filler concentration leads to a growth in the inhomogeneity of the dissipation fields. As a result, the motion of a benzene molecule by the same distance leads to a greater variation in the local magnetic field. Thus, the nuclear magnetic spin echo measurements in magnetic fluids may provide data on the nature of their viscosity, which are difficult to obtain by different methods.

REFERENCES

1. González, D. Pusiol, A. M. F. Neto, *et al.*, J. Chem. Phys. **109**, 4670 (1998).
2. G. J. Da Silva, P. C. Morais, and F. A. Tourinho, J. Chem. Phys. **107**, 2793 (1997).
3. A. Abraham, *The Principles of Nuclear Magnetism* (Clarendon Press, Oxford, 1961; Inostrannaya Literatura, Moscow, 1963).
4. A. A. Vashman and I. S. Pronin, *Nuclear Magnetic Relaxation Spectroscopy* (Nauka, Moscow, 1986).

Translated by P. Pozdeev

Technical Physics Letters, Vol. 27, No. 1, 2001, pp. 9–10. Translated from Pis'ma v Zhurnal Tekhnicheskoĭ Fiziki, Vol. 27, No. 1, 2001, pp. 19–23.

Diagnostics of High-Resistivity GaAs Wafers by Microwave Photoconductivity

L. S. Vlasenko, A. T. Gorelenok, V. V. Emtsev, A. V. Kamanin, S. I. Kokhanovskiĭ, D. S. Poloskin, and N. M. Shmidt

Ioffe Physicotechnical Institute, Russian Academy of Sciences, St. Petersburg, 194021 Russia

Received September 4, 2000

Abstract—It is demonstrated that the method of microwave photoconductivity developed previously for the study of ultrapure Si can be successfully employed in the qualitative diagnostics of pure high-resistivity GaAs. Data on the microwave photoconductivity of GaAs are in good agreement with the results of measurements of the Hall effect, *C–V* characteristics, and low-temperature photoluminescence. © *2001 MAIK "Nauka/Interperiodica".*

The diagnostics of high-resistivity materials, exhibiting charge carriers concentration below 10^{12} cm^{-3}, always meets substantial difficulties. The reason is that the methods employed necessitate obtaining Ohmic contacts to such materials. The difficulty of this problem accounts for the interest in contactless methods for the investigation and diagnostics of semiconductors. The method of microwave photoconductivity (MPC) is a contactless technique based on the measurements of the microwave absorption by a sample placed inside a cavity. This method is successfully used in the studies of pure silicon crystals. In particular, the detection of changes in the microwave photoconductivity upon excitation of the magnetic resonance of the charge recombination centers in silicon allowed the electron paramagnetic resonance (EPR) spectra to be measured at the center concentration of 10^{10}–10^{12} cm^{-3} [1–3]. The sensitivity of the MPC method in combination with EPR appeared to be four orders of magnitudes higher than that of the conventional EPR and one–two orders of magnitude higher than that attained in the measurements of the dc photoconductivity.

Preliminary experiments showed that the MPC method developed for the studies of the spin-dependent recombination (SDR) in silicon [4–6] can be informative and sensitive in the studies of GaAs as well. However, the method exhibits two contradictory tendencies preventing one from an unambiguous conclusion regarding its applicability, which necessitates additional experimental studies. SDR and EPR measurements show that the main differences between Si and GaAs crystals are the greater motility of free carriers in the latter semiconducor and nonzero magnetic moments of Ga and As nuclei. Thus, one can expect a greater photoconductivity and an increase in the SDR sensitivity in GaAs as compared to silicon. However, GaAs contains magnetic nuclei and exhibits hyperfine interaction, which leads to substantial broadening and a decrease in intensity of the EPR lines.

In this work, we report on the first results regarding diagnostics of high-resistivity GaAs wafers by the MPC method.

The experiments were performed with GaAs wafers doped with iron and the GaAs plates after various stages of gettering, with the carrier concentration ranging from 10^{15} to 10^{8} cm^{-3}. The concentrations of charge carriers determined from measurements of the Hall effect and the *C–V* characteristics at 300 K.

The microwave photoconductivity measurements were performed in the 3–150 K temperature range using an EPR spectrometer operating at 9 GHz. The samples were placed into the spectrometer cavity and illuminated by a 100-W incandescent halogen lamp. The cavity Q-factor depends on the sample conductivity.

We measured the light-induced changes in the output voltage of the microwave detector (that is proportional to the Q-factor) at the frequency of the 100% light intensity modulation (80 Hz). The MPC signals were measured at various temperatures and magnetic field strengths.

Figure 1 shows the plots of MPC versus temperature for pure GaAs crystals measured prior to and after heat treatment (HT). The initial resistance of the samples accounts for the substantial decrease in the Q-factor. The untreated samples exhibit photoresponse only at low temperatures of 3–25 K with the maximum at 5–7 K (curve *1* in Fig. 1). The 0.5-h HT leads to an increase in the resistance of the crystal, after which the photoresponse is observed at higher temperatures (up to 70 K) (curve *2* in Fig. 1). After a 3-h HT, the samples possess a high resistance even at room temperature and exhibit a photoresponse in the entire temperature range studied (curve *3* in Fig. 1).

1063-7850/01/2701-0009$21.00

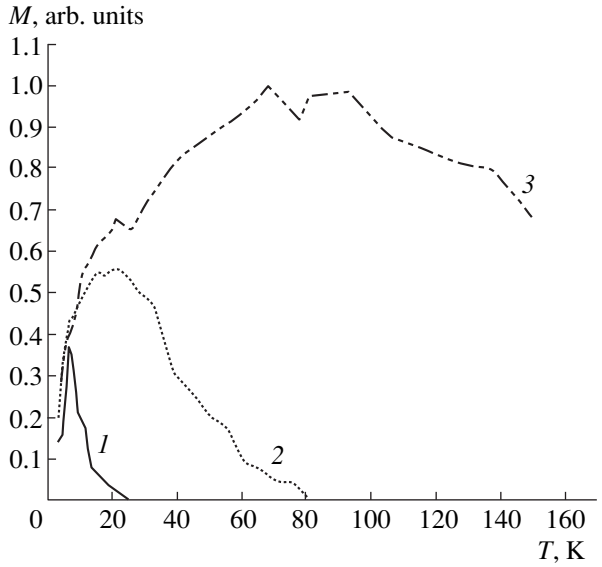

Fig. 1. Plots of the microwave photoconductivity versus temperature GaAs crystals: (*1*) prior to HT, (*2*) after HT for 0.5 h at 800°C (ShGA-6), and (*3*) after HT for 3 h at 800°C (ShGA-4).

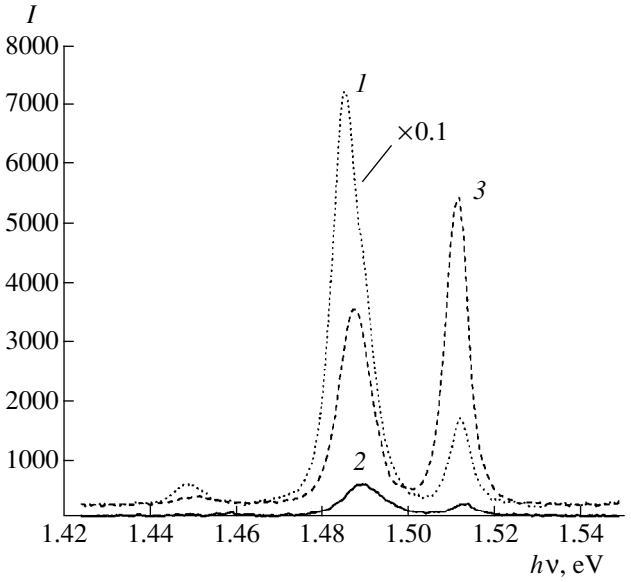

Fig. 2. PL spectra of GaAs measured at 2 K (*1*) prior to HT, (*2*) after HT for 0.5 h at 800°C (ShGA-6), and (*3*) after HT for 3 h at 800°C (ShGA-4).

Despite a high photoresponse of the pure GaAs crystals we did not manage to observe the EPR spectra related to changes in the microwave photoconductivity of these samples. The lines of the magnetic resonance of the paramagnetic recombination centers were observed only in the GaAs crystals doped with Fe, the photoconductivity of which is several times smaller than that of the pure GaAs crystals.

The HT-induced increase in the dark conductivity of GaAs cannot be explained by a trivial compensation of the shallow donors by the deep centers. If this were the case, we would rather observe an increase in the recombination rate of the photoexcited carriers and, hence, a decrease in the photoconductivity. This effect is observed, for example, in GaAs doped with Fe. The HT-induced increase in the GaAs photoconductivity and the absence of SDR–EPR spectra can be explained by passivation of the shallow donors and by the formation of electrically and paramagnetically inactive centers.

The experimental data are in good agreement with the results of the Hall effect and *C*–*V* measurements and the low-temperature photoluminescence (PL) data. Figure 2 shows the low-temperature PL spectra for the same samples as in Fig. 1. It is seen that an increase in the gettering HT time leads to quenching of the impurity band with $h\nu \sim 1.49$ eV and increasing intensity of the band with $h\nu \sim 1.512$ eV (bandgap energy of GaAs). These changes can be interpreted as being due to purification of the material, which is additionally confirmed by an increase in the spectral range of the MPC photoresponse (Fig. 1).

Thus, the contactless method based on the microwave photoconductivity measurements may be helpful in the studies of the photoelectric properties, estimating the quality, and diagnostics of the high-resistivity semiconductor materials.

Acknowledgments. The work was supported by the Russian Foundation for Basic Research, project no. 00-02-17026.

REFERENCES

1. H. J. Von Bardeleben and J. C. Bougoin, *Defect Control in Semiconductors*, Ed. by K. Sumino (Elsevier, Amsterdam, 1990).
2. A. V. Markov *et al.*, Vysokochist. Mater. **1**, 86 (1996).
3. C. M. Buttar, Nucl. Instrum. Methods Phys. Res. A **395**, 1 (1997).
4. L. S. Vlasenko, M. P. Vlasenko, V. N. Lomasov, and V. A. Khramtsov, Zh. Éksp. Teor. Fiz. **91**, 1037 (1986) [Sov. Phys. JETP **64**, 612 (1986)].
5. L. S. Vlasenko, in *Semiconductors and Insulators: Optical and Spectroscopic Research*, Ed. by Yu. Koptev (Nova Science, 1992), p. 217.
6. L. S. Vlasenko, Yu. V. Martynov, T. Gregorkiewicz, and C. A. J. Ammerlaan, Phys. Rev. B **52**, 1144 (1995).

Translated by A. Chikishev